

MICROSTRUCTURES AND OXIDATION PROPERTIES IN
HAFNIUM-TANTALUM-NITRIDE CERAMICS

by

BRADFORD CHRISTOPHER SCHULZ

GREGORY THOMPSON, COMMITTEE CHAIR
DANIEL BUTTS
ROBIN FOLEY
J. BRIAN JORDON
MARK WEAVER

A DISSERTATION

Submitted in partial fulfillment of the requirements
for the degree of Doctorate of Philosophy in the
Department of Metallurgical Engineering in
the Graduate School of the
University of Alabama

TUSCALOOSA, ALABAMA

2013

Copyright Bradford Christopher Schulz 2013
ALL RIGHTS RESERVED

ABSTRACT

Ultra high temperature ceramics (UHTC) comprise a class of materials characterized by high melting points, chemical inertness, high hardness, and moderate oxidation. These ceramics typically comprise either group IV or V metals bonded with boron, carbon or nitrogen. When in equal atomic ratio, a MX compound will nominally form, where M is the metal species and X the interstitial light element (boron, carbon, or nitrogen). For the group V metals, small changes in the M:X ratio can result in the precipitation of M_6X_5 , M_4X_3 , M_3X_2 , and/or M_2X compounds. The precipitation of these phases can have a dramatic influence on the microstructure's grains' morphology and properties, including mechanical, electrical, and oxidation.

To understand the microstructure-property relationship in the hafnium nitride system, two sets of hafnium nitride diffusion couples were processed by hot-isostatic pressing and their resulting microstructure and phase orientation were identified. Distinct regions were found in the diffusion couples. It was shown that the rhombohedral ζ -Hf₄N₃ phase, like other M_4X_3 UHTCs, formed through elemental migration along close-packed planes from FCC structures. Lattice parameter calculations from the high temperature diffusion couple verified homogeneity ranges of ϵ -Hf₃N₂ and ζ -Hf₄N₃.

To study the relationship of microstructure-oxidation behavior a series of (HfN)_{1-x}(TaN)_x ultra-high temperature nitrides were fabricated with the vacuum plasma spray process. The resulting nitrides had significant nitrogen content loss. This loss of nitrogen was used to explain the formation of metal-rich nitrides. The nitride compositions underwent two oxidation

experiments between 400-1600°C. The resulting oxide scales were characterized by X-ray diffraction and electron diffraction. The 18.8 at.% specimen deviated from norm and had the lowest mass change and grew a black scale. This black scale contained rhombohedral ϵ -Hf₃N₂ and ζ -Hf₄N₃ phases with elongated *c*-lattice parameters and STEM analysis showed increased oxygen content in these structures. This black oxy-nitride scale acted as a passivation layer minimizing oxygen diffusion through close-packed crystal lattices.

This oxy-nitride layer was further investigated to analyze the processing-oxidation behavior relationship. It was found that the increase in density for the nitrides processed by the combined vacuum plasma spray and additional sinter/HIP steps improved oxidation resistance. The reaction of hafnium nitride conversion into hafnia was found to be affected by both boundary and diffusion mechanisms. The growth of an oxy-nitride intermediate layer was observed to coarsen and begin forming as low as 650°C. Not only did the high density minimize boundary oxidation but the oxy-nitride also lowered the rate of oxygen diffusion through the reaction layer.

ACKNOWLEDGMENTS

I am pleased to take this opportunity to thank my colleagues, friends, and faculty members who have helped me with this research project. I am indebted to my advisor Dr. Gregory Thompson, the chairman of this dissertation, for providing me with this opportunity and for his trust. I would also like to thank all of my committee members; doctors Daniel Butts, Robin Foley, Brian Jordon, and Mark Weaver for their invaluable input, questions, and support in my dissertation progress. I would like to thank Dr. Daniel Butts with Plasma Processing, LLC. and Dr. Steve DiPietro with Exothermics, Inc. for providing a gracious amount of samples used in this research.

Finally, this research would not have been possible without the support of my friends and fellow graduate students and of course the endless encouragement from my family. Currently, the chapters are in the process of being submitted for publication. The first paper, titled “Phase and Microstructure Relationships in Hf-N”, will be submitted to the International Journal of Applied Ceramic Technology. The second paper, titled “Oxidation Behavior of Vacuum Plasma Sprayed Hafnium-Tantalum Nitrides“, will be submitted to the Journal of American Ceramic Society. The last paper, titled “Influence of an Oxy-nitride Scale on the Oxidation Characteristic in Hf(Ta)N“, will be submitted to the Journal of European Ceramic Society.

LIST OF ABBREVIATIONS AND SYMBOLS

3D	Three-dimensional
at.%	atomic percent
BCC	Body-centered cubic
EBSD	Electron backscattered diffraction
EDS	Energy dispersive spectroscopy
eV	electron volts
FCC	face-centered cubic
FIB	Focused ion beam
HAADF	High angle annular dark field
HCP	Hexagonal close-packed
HIP	Hot-isostic pressure
°C	Celsius
Pa	Pascal
R _{PB}	Pilling-Bedworth ratio

SAED	Selected area electron diffraction
SEM	Scanning electron microscope
STEM	Scanning transmission electron microscope
TEM	Transmission electron microscope
UHTC	Ultra high temperature ceramic
VPS	Vacuum plasma spraying
wt. %	weight percent
XRD	X-ray diffraction

CONTENTS

ABSTRACT	ii
ACKNOWLEDGMENTS	iv
LIST OF ABBREVIATIONS AND SYMBOLS	v
LIST OF TABLES	viii
LIST OF FIGURES	x
CHAPTER 1: INTRODUCTION	1
CHAPTER 2: PHASE AND MICROSTRUCTURE RELATIONSHIPS IN HF-N	12
CHAPTER 3: OXIDATION BEHAVIOR OF VACUUM PLASMA SPRAYED HAFNIUM-TANTALUM NITRIDES	26
CHAPTER 4: INFLUENCE ON AN OXY-NITRIDE SCALE ON THE OXIDATION CHARACTERISTIC IN HF(TA)N	48
CHAPTER 5: CONCLUSION AND FUTURE DIRECTIONS	64
REFERENCES	67
APPENDIX A: XRD LINE SCAN PROCEDURE	74
APPENDIX B: DENSITY FUNCTIONAL THEORY EXAMPLE REACTIONS FOR THE HAFNIUM AND TANTALUM NITRIDE SYSTEMS	80
APPENDIX C: INITIAL WORK ON HAFNIUM-TANTALUM-NITRIDE CHARACTERIZATION OF MECHANICAL BEHAVIOR	91

LIST OF TABLES

Table 2-1: Calculated lattice parameters from the XRD line scan for α -Hf, ϵ -Hf ₃ N ₂ , ζ -Hf ₄ N ₃ , and δ -HfN compared with prior findings (McMurdie ^[65] , Rudy ^[27] , and Fiala ^[66]). The calculated lattice parameters were derived from the minimum and maximum 2 θ values based on intensity-distance relationships from Figure 2-3(a).	19
Table 3-1: Analysis of the four (HfN) _{1-x} (TaN) _x nitrides (0.0, 18.8, 28.1, 46.7 at.%) post-VPS processed. Analysis includes the porosity % calculated with the Delesse Principle and LECO results.	32
Table 3-2: Analysis of the four (HfN) _{1-x} (TaN) _x nitrides (0.0, 18.8, 28.1, 46.7 at.%) post-oxidation. Mass change % was measured for all four specimens for first oxidation series (700°C, 1200°C, and 1700°C).	34
Table 3-3: Lattice parameters (left) based on peak shift from the 18.8 at.% 1700°C oxidized specimen XRD line scan compared with prior literature (right: (McMurdie ^[65] , Rudy ^[27] , and Fiala ^[66])).	37
Table 3-4: Mass change % for the (HfN) _{1-x} (TaN) _x X=18.8 at.% specimen post-oxidation II treatment.	39
Table 3-5: Phase vol.% identified from the EBSD for (HfN) _{1-x} (TaN) _x X=18.8 at.% specimen post-oxidation I treatment at 1700°C.	43
Table 4-1: Pre-heat treatment (left) homogenization density and porosity % values as well as the (right) nitrogen content. The initial nitrogen value (at.%) is based on starting powders, the post (at.%) is nitrogen content post-processing.	53
Table 4-2: EBSD phase content (volume %) of sintered/HIP'ed specimen pre-oxidation treatments.	54
Table 4-3: Oxidation treatment I mass % change for the (left) as-sprayed condition and (right) the additional sintered/HIP'ed. The oxidation heat treatment was for three times and four temperatures.	56

Table 4-4: Oxidation treatment II mass % change for (left) as-sprayed conditions and (right) the additional sintered/HIP'ed. The first group *C*- had no low 650°C treatment but just 10 min oxidation at 1200°C follow by an air quench. The second group *T*- was oxidized for 10 min at 650°C followed by an air quench and then oxidized for 10 min at 1200°C with an air quench after. 58

Table C-1: EBSD of high-temperature flexural tested 80HfN-20TaN at 1650°C..... 92

Table C-2: Lattice parameters based on XRD line scan. Starting at top: (1) Hf, (2) Hf₃N₂ main peak, (3) Hf₃N₂ new split peak, (4) Hf₄N₃ main peak, (5) Hf₄N₃ new split peak, (6) HfN. 92

LIST OF FIGURES

Figure 1-1: Rudy’s revised Hf-N system phase equilibrium [3].	4
Figure 1-2: (Left to right) α -Hf ($P6_3/mmc$), ϵ -Hf ₃ N ₂ ($R\bar{3}m$), ζ -Hf ₄ N ₃ ($R\bar{3}m$), δ -HfN ($Fm\bar{3}m$).	4
Figure 1-3: Crystallographic (110) view of ζ -Hf ₄ N ₃ and ϵ -Hf ₃ N ₂ demonstrating alternating hexagonal (h) and cubic (c) layers [27].	5
Figure 1-4: Processes occurring in three types of oxide surface scale during oxidation (a) interstitial cation, (b) anion vacancy, and (c) cation vacancy. Based on Figure 12.13 from Jones [42].	7
Figure 2-1: (a) Phase diagram of Hf-N system [3] with red lines indicating 1900°C (solid) and 1200°C (dashed). Crystallographic (11 $\bar{2}$ 0) view (b) of ζ -Hf ₄ N ₃ and ϵ -Hf ₃ N ₂ demonstrating alternating hexagonal (h) and cubic (c) layers bonded along the interstitial [27].	15
Figure 2-2: EBSD of the 1900°C diffusion couple with locations of regions [A]-[E] approximated on the (a) image quality reconstructed map. (b) Phase identification for the reaction zone based on the diffraction data. (c) Orientation mapping for the reaction zone. Magnified region [C] and [D] image (d) quality map, (e) phase identification, and (f) crystallographic orientation.	18
Figure 2-3: XRD line scan of the 1900°C diffusion couple with a step size of 0.01 mm. The unique peak maximums for each phase are indicated on (a), the [10 $\bar{1}$ 1] peak for α -Hf (McMurdie ^[65]), the [0009] peak for ϵ -Hf ₃ N ₂ (Rudy ^[27]), the [00015] peak for ζ -Hf ₄ N ₃ (Rudy ^[27]), and the [200] peak for δ -HfN (Fiala ^[66]). Note the peaks begin at δ -HfN and progress towards α -Hf. (a) Entire image with x-2 θ (25°-60°), y-distance (0.00-1.25 mm), and z-intensity. Same line scan (b) from 56°-59° arranged to depict the additional [hk0] peak, the [11 $\bar{2}$ 0], for c-lattice parameter calculations.	19
Figure 2-4: EBSD of the 1200°C diffusion couple with locations of regions [A], [B], [C*], and [E] approximated on the (a) image quality reconstructed map. (b-c) Approximate magnified region of [B], [C*], and [E] from (a). The (b) image quality map demonstrating lath microstructures indicated by the arrows and (c) is the phase identification map.	21

Figure 3-1: SEM imaging of pre-mixed nitride powders (left: HfN, right: TaN).	32
Figure 3-2: Pre-oxidation normalized XRD phase identification of the four specimens $(\text{HfN})_{1-x}(\text{TaN})_x$ where X is 0.0, 18.8, 28.1 and 46.7 wt.%. The phase peak information for the phases considered are presented below the four specimens.	33
Figure 3-3: Pre- and post-oxidation images of the four specimens $(\text{HfN})_{1-x}(\text{TaN})_x$ where X is 0.0, 18.8, 28.1 and 46.7 at.%.	34
Figure 3-4: Post-oxidation normalized XRD phase identification of the oxide scale for specimen $(\text{HfN})_{1-x}(\text{TaN})_x$ where X=0.0 (a), 18.8 (b), 28.1 (c), and 46.7 (d) at.% for the three oxidation experiment temperatures (top). The normalized phase peak information for the main oxide phases considered are presented below the XRD data.	35
Figure 3-5: XRD line scan of the $(\text{HfN})_{1-x}(\text{TaN})_x$ 18.8 at.% 1700°C oxidized specimen with a step size of 0.01 mm. (Left) Entire image with $x-2\theta$ (25°-50°), y-distance (0.00-1.00 mm), and z-intensity. (Right) Line scan data view from x-y plane with peaks utilized for phase identification marked.	37
Figure 3-6: (a) Example of SEM EDS line scan of oxidation II treatment scale thickness. This specific scan is one of three from the 1200°C 60 min specimen. The bulk of the specimen on left, intermediate layer in middle, and oxide scale on right. (b) Plot of oxide scale and intermediate layer based on SEM EDS line scans. The solid line represents the oxide scale measurements, dashed line for the intermediate scale, and the error bars are marked as red in the y-axis. An additional plot of normalized mass change vs. temperature is also plotted in red which shows the similar findings from Desmaison-Brut and Montintin ^[9]	39
Figure 3-7: The $(\text{HfN})_{1-x}(\text{TaN})_x$ X=18.8 at.% specimen post-oxidation I treatment at 1700°C oxidation. a) HAADF STEM image of lath-like microstructure with marked path of STEM EDS line profile. The brighter contrast in these laths (dash arrows) is due to hafnium enrichment found in the (b) STEM EDS line profile. (b) EDS line profile shows oxygen intensity peak data.	42
Figure 3-8: The EBSD for $(\text{HfN})_{1-x}(\text{TaN})_x$ X=18.8 at.% specimen post-oxidation I treatment at 1700°C oxidation. a) Image of four hafnium phases. d) Image of the phases with oxygen.	43
Figure 3-9: Ternary Hf-Ta-N phase diagram at 1000°C based on initial Rudy ^[38] findings. The ϵ -Hf ₂ N phase in the original report [38] has been replaced by ϵ -Hf ₃ N ₂ & ζ -Hf ₄ N ₃ ^[27] . In this diagram, dashed lines (1-4) estimate the nitrogen loss path for (1) 0.0, (2) 18.8, (3) 28.1, and (4)	

46.7 at.% (TaN) with arrows indicating nitrogen loss direction. The red dashed lines are approximated for 25 and 50 at.% nitrogen..... 45

Figure 4-1: XRD of as-sprayed and sintered/HIP'ed pre-oxidation treatments. 53

Figure 4-2: SEM image of as-sprayed microstructure (a). EBSD of sintered/HIP'ed specimen with quality reconstructed image (b) and phase content mapping (c). The phase content is matched based on colors found in the key. 54

Figure 4-3: Scale thickness measurements of the post-oxidation treatment I measured with EDS line scans from SEM imaging (a). As-sprayed (b) with solid lines indicating oxide scale, dash is the intermediate scale, and color is based on the three times studied. Sintered/HIP'ed (c) with solid lines indicating oxide scale, dash is the intermediate scale, and color is based on the three times studied. 56

Figure 4-4: Measured EDS length of scales from the as-sprayed conditions (black and blue) and the additional sintered/HIP'ed (orange and green) post-oxidation treatment II. The *C*- without low 650°C oxidation is on the left while the *T*- with a low 10 min 650°C oxidation is on the right. Both groups were oxidized at 1200°C for 10 min with an air quench. 58

Figure 4-5: STEM-HAADF images and SAED of a FIB lift-out foil from the *T*-sintered/HIP'ed. STEM image (a) of FIB lift-out foil with the bulk region on left, intermediate on right, marked SAED diffraction pattern location, and STEM EDS line profile. The SAED diffraction pattern (b) identifies the lath-like microstructure as ϵ -Hf₃N₂. The EDS line profile (c) across this lath indicates hafnium (intensity on left axis) and oxygen (intensity on right axis) content. 60

Figure 4-6: Example SEM imaging of (a) as-sprayed condition and (b) the additional sintered/HIP'ed post-oxidation treatment II for *T*-set. Approximate locations of oxide scale (note the observable charging), intermediate and bulk are marked. 62

Figure A-1: Interior image of Bruker XRD system at the University of Alabama. XRD probe on left, optical camera in the middle, and XRD detector on right. The x- and y-axis' are labeled. .. 74

Figure A-2: GADDS line scan software parameters. 75

Figure A-3: Imported XRD files from Excel into Origins..... 76

Figure A-4: Orientate display to determine peak maxima and their frame-distance positioning.77

Figure A-5: Shows Origins on-screen commands. How to change the display speed, rotation and image adjustment, as well as axis parameter changes are described above..... 77

Figure A-6: Demonstration of peak analysis to determine the 2-theta values of frame-distance position..... 78

Figure A-7: Screen shot demonstrating the creation of a 2D line scan plot. 78

Figure A-8: Example Excel sheet with appropriate equations in determining *a*- and *c/a* lattice values in a hexagonal crystal system. 79

Figure C-9: EBSD of high-temperature flexural tested 80HfN-20TaN at 1650°C. The bulk is on left and scale on right. All phases are shown in (a) including the prior-literature Hf₂ON₂ and Hf₇O₈N₄ oxy-nitrides as well as the predicted Hf₃ON₂ and Hf₄ON₃. Only the nitrides and elemental Hf are shown in (b) for comparison. 92

Figure C-10: HAADF STEM image (a) of the 1650°C post-tested specimen with bulk on left and oxide scale on left. The line profile (b) from (a) and the diffraction pattern (c) is the spot found in (a)..... 92

Figure C-11: Atom probe tip (a) from bulk of 1650°C tested nitride and tip (b) near oxide/intermediate interface..... 92

Figure C-12: XRD line scan of 1650°C specimen from bulk (bottom, distance = 0) to oxide scale (distance = 1.00). At distance = 0.5 an example 2D plot shows the peak shifting. 92

CHAPTER 1 INTRODUCTION

Motivation

Ultra high temperature ceramics (UHTC) comprise a class of materials characterized by high melting points, chemical inertness, high hardness, and moderate oxidation resistance [1-3]. These ceramics typically comprise either group IV or V metals bonded with boron, carbon or nitrogen [2-29]. When in equal atomic ratio, a MX compound will nominally form, where M is the metal species and X the interstitial light element (boron, carbon, or nitrogen). For the group V metals, small changes in the M:X ratio can result in the precipitation of M_6X_5 , M_4X_3 , M_3X_2 , and/or M_2X compounds. The precipitation of these phases can have a dramatic influence on the microstructure's grains' morphology [1-2,5,8,13-14,23-24,29-35] and properties, including mechanical [18,22,36], electrical [23-24] and oxidation [4,10-15,35,37].

The high melting temperatures of UHTCs lead to applications at extreme environments, load bearing components at high atmospheric temperatures. Understanding how these phases form with the resultant microstructure and their effect on material properties is essential to engineer these ceramics. In the current research, the phase equilibrium and phase transformation pathways for hafnium nitrides were explored. Special consideration was placed on the interrelationship of these microstructures and their oxidation behavior, including the mechanisms of oxidation. In particular, it was hypothesized that the closed-packed symmetry of the hafnium-rich nitrides with interstitial vacancies yield a stable crystallographic framework for an adherent intermediate oxide scale that improved oxidation resistance.

The first objective of this research was to explore the multi-phase microstructures in the Hf-N system, with particular attention to compositions that span between the hafnium metal to the mono-nitride composition. The ϵ -Hf₃N₂ and ζ -Hf₄N₃ phases, which were the primary phases of study, are believed to be a result of subtle variations in the close pack stacking sequence caused by changes in nitrogen interstitial site occupancies. The second objective of the research was to determine the oxidation behavior and the oxidation mechanisms associated with these compositions. This research focused on the nitrogen doped α -Hf, ϵ -Hf₃N₂, and ζ -Hf₄N₃ phases and their multi-phase regions. The inherent crystallography of the Hf-rich nitrides and how it contributed to the formation of an adherent intermediate oxy-nitride scale was explored. The

third, and final objective, was to investigate how processing related to the stabilization of this adherent intermediate oxy-nitride scale.

Technical Background

Crystallography and Phase Stability of Hf_xN_{1-x} Phases

Nitrogen is soluble in the hexagonal α -Hf phase ($P6_3/mmc$) up to 30 at.% N [3], as seen in Figure 1-1. The increase solubility content of nitrogen increases the melting temperature of α -Hf from 1743°C to 2910°C as well as increases the α -Hf to BCC β -Hf ($Im\bar{3}m$) allotropic transformation at a rate of $\sim 83 \pm 10^\circ\text{C}/\text{at.}\%$ [26]. The incorporation of nitrogen strengthens the intrinsic bonding in hafnium evident by these increases in melting or allotropic temperatures. From 43 at.% N to slightly above 50 at.% N, the mononitride δ -HfN forms with the B1 or cubic $Fm\bar{3}m$ rock-salt crystal structure. Between 33 to 47 at.% N (which is between the α -Hf and δ -HfN phases) the rhombohedral ϵ -Hf₃N₂ and ζ -Hf₄N₃ phases form, with each phase having the $R\bar{3}m$ point group symmetry. The crystallography of these phases can be seen in Figure 1-2. Previously, these hafnium-rich nitride phases were thought to be a hexagonal Hf₂N structure [18]. The particular stoichiometries of M₄X₃ and M₃X₂ phases can be understood from their structural similarities to the HCP M₂X and FCC-like MX structures [26-27,38].

In the HCP M₂X structure, different stacking sequences of the metallic atoms result in different spatial arrangements of the octahedral interstices. The octahedral interstices form straight chains running parallel to the c -axis with vacancies and interstitial atoms alternating along the chains [27]. This pattern of alternating carbon-hole occupancy of the interstitial sites along the c -axis is common to ordered sub-lattice structures of the M₂X structure and is believed to be maintained in the disordered modifications at high temperatures [39]. In contrast, larger spacing's between interstitial sites are allowed in the FCC MX phases [27] and all sites may be occupied.

Both types of interstitial atom packing are possible in the ϵ -Hf₃N₂ and ζ -Hf₄N₃ structures. Within the ϵ -Hf₃N₂ and ζ -Hf₄N₃ phases, linkages consisting of three interstitial sites are arranged as hexagonal M₂X symmetries joined by one (ϵ -Hf₃N₂) or two (ζ -Hf₄N₃) linked nitrogen atoms which are stacked similar to cubic mononitride [27]. The links are believed to account for the observed occupancy, $\frac{2}{3}$ for ϵ -Hf₃N₂ and $\frac{3}{4}$ for ζ -Hf₄N₃, of the three adjacent linkages and thus maintaining the interstitial atom-vacancy sequence derived from the M₂X structure [27].

The similarity between the ϵ -Hf₃N₂ and ζ -Hf₄N₃ phases becomes evident from the crystallographic (110) sectional cut of both unit cells, Figure 1-3. The ζ -Hf₄N₃ structure may be formed by adding a cubic metal layer (c) after every third layer in the ϵ -Hf₃N₂ structure, leading to the sequence (hhcc)₃ in ζ -Hf₄N₃ from ϵ -Hf₃N₂'s (hhc)₃ [27]. Both phases are rhombohedral and similarly structured to HCP M₂X which leads to the uncertainty and confusion from literature about the existence of an Hf₂N phase [27,33,38,40].

Crystallography of Ternary Hf-Ta-N Phases

Rudy *et al.* investigated the solid solution of HfN-TaN and found that δ -HfN can accommodate up to approximately 75 mol.% ϵ -TaN (hexagonal $P6/mmm$) into solution in the cubic B1 crystal structure [41]. At approximately, 2000°C, it undergoes a polymorphic transformation to a δ -TaN (cubic $Fm\bar{3}m$) phase which can span approximately 41 to 50 at.% N up to a melting temperature over 2800°C [25] and may explain how it is accommodated into the cubic δ -HfN phase. The γ -Ta₂N phase is hexagonal in symmetry ($P6_3/mmc$), which could provide substitutional sites in the rhombohedral hafnium rich nitride phases or even the α -Hf metal. The α -Hf metal can accommodate up to 30% nitrogen in solution. The only complete solid solution formation in the system is BCC β -(Ta,Hf) (cubic $Im\bar{3}m$) above 1770°C. The α -Hf phase has a maximum solubility of tantalum at 22 at.% Ta (2260°C). The δ -(Hf,Ta)N_{1-x} has a maximum solubility of tantalum at 47 at.% (2100°C). Above 2100°C, the maximum solubility of tantalum in the δ -(Hf,Ta)N_{1-x} is at the mononitride phase boundary of the two-phase field, γ -Ta₂N + δ -(Hf,Ta)N_{1-x}. The maximum solubility of hafnium in γ -Ta₂N is 9.5 at.% at 2800°C and 30 at.% N for the solid solution at the three-phase boundary: β -(Ta,Hf) + γ -(Ta,Hf)₂N + δ -(Hf,Ta)N_{1-x} [20]. This resulted in a range of tantalum composition additions that could be added to the variety of nitride phases suggested previously and determine if tantalum, which can form in solution, alters the oxidation behavior through scale formation or other means.

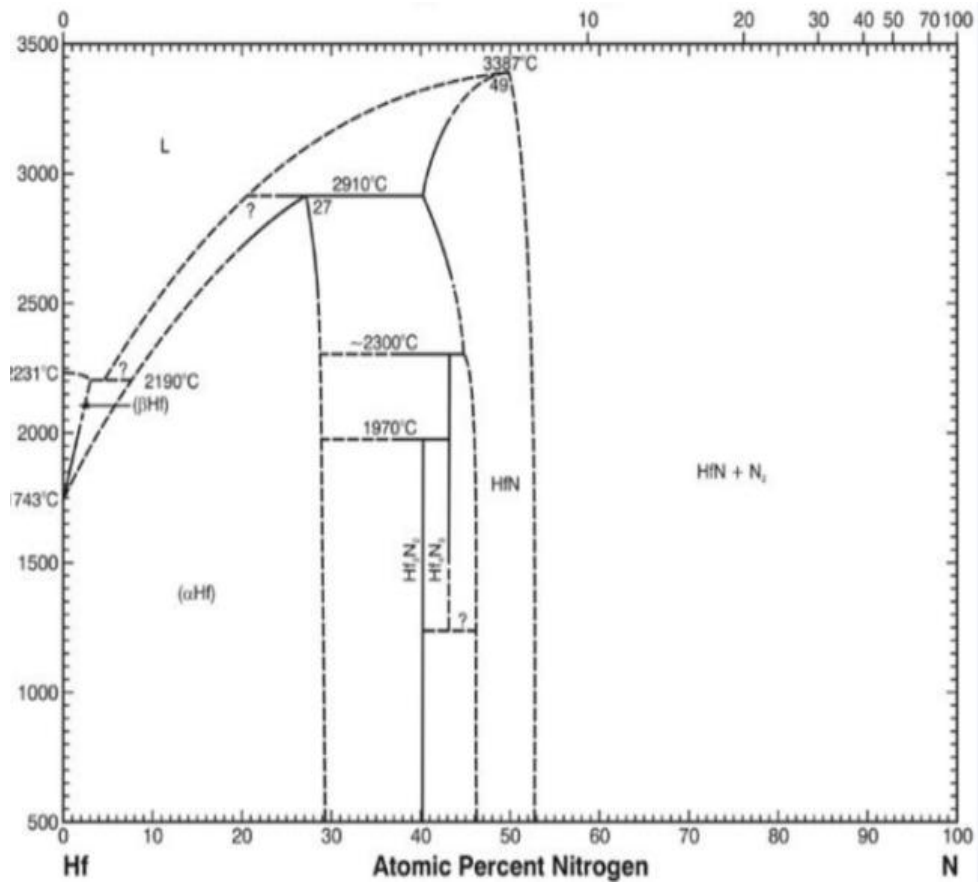


Figure 1-1: Rudy's revised Hf-N system phase equilibrium [3].

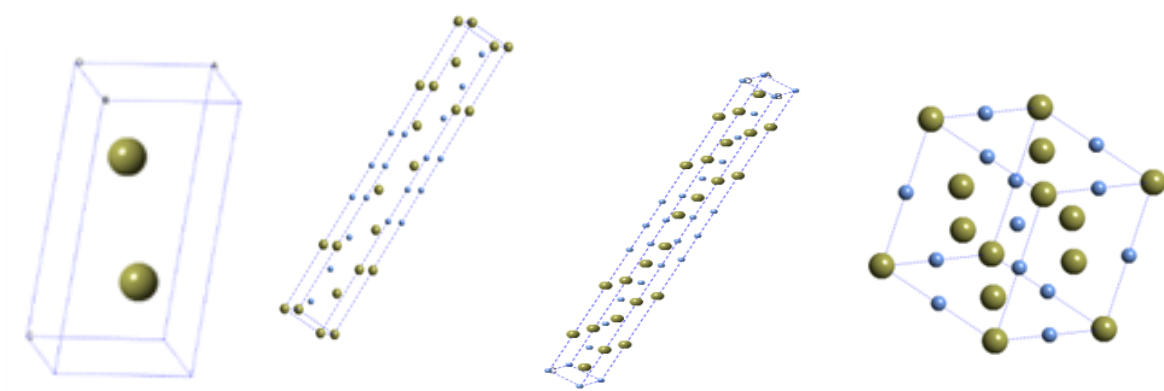
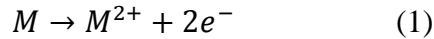


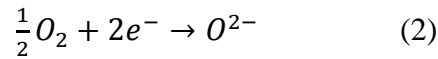
Figure 1-2: (Left to right) $\alpha\text{-Hf}$ ($P6_3/mmc$), $\epsilon\text{-Hf}_3\text{N}_2$ ($R\bar{3}m$), $\zeta\text{-Hf}_4\text{N}_3$ ($R\bar{3}m$), $\delta\text{-HfN}$ ($Fm\bar{3}m$).

Oxidation Mechanisms

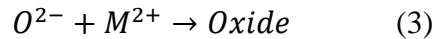
Oxidation at elevated temperatures is a chemical reaction that typically occurs on metallic surfaces exposed to oxygen. In UHTCs the metallic cations will react with oxygen, nucleate an oxide, and laterally grow a continuous film into the underlying material. There are three generic types of oxide film growth processes; (a) metal excess with interstitial cations, (b) metal excess with anion vacancies, and (c) metal deficit with cation vacancies [42], Figure 1-4. In all three cases, M (an arbitrary metal) atoms are oxidized to M^{2+} by equation (1)



freeing electrons across an oxide scale to partake in the reduction of molecular oxygen,



at the oxide-gas interface. Electron transport occurs by movement of free electrons in *n*-type oxides, but in *p*-type oxides, electron hole migrate by electrons transferred between M^{2+} cations [42]. Growth of *n*-type cation interstitial oxides (a) involves the freeing of interstitial cations (1) at the oxide-metal interface and migration to the oxide-gas interface to form an oxide scale. The reduction of oxygen (2) is the most thermodynamically favorable source of O^{2-} , but it is possible for M to be oxidized by water vapor or carbon dioxide. For the *n*-type anion vacancy oxides (b), O^{2-} anions migrate through the oxide lattice by anion vacancies to the oxide/metal interface where they form an oxide scale. Note that the formation of an oxide, the reaction interface from equation (3)



occurs at the oxide/metal interface in (b) but at the oxide/gas interface for (a). Lastly, the *p*-type metal-deficit oxides (c) grow by providing M^{2+} cations at the oxide/metal interface which migrate to the oxide/gas interface by cation vacancies. Like (a), the cations form the oxide scale at the oxide/gas interface.

The oxidation of a multiple element component system is more complex and relies on the: (1) solubility of parent materials, (2) affinity and thermodynamic stability of possible oxides, and (3) the mobility of component species [43]. Depending on these conditions the oxide scale can either be: (i) a mixture of oxides, (ii) a single dominant oxide, or (iii) an external and internal oxide [43]. The oxide scale would begin with the nucleation of reaction sites of various oxides that would eventually be dominated by a thermodynamically favorable oxide. Too selective of a mixture may result in excessive scale formation, cracking, and/or spalling [43].

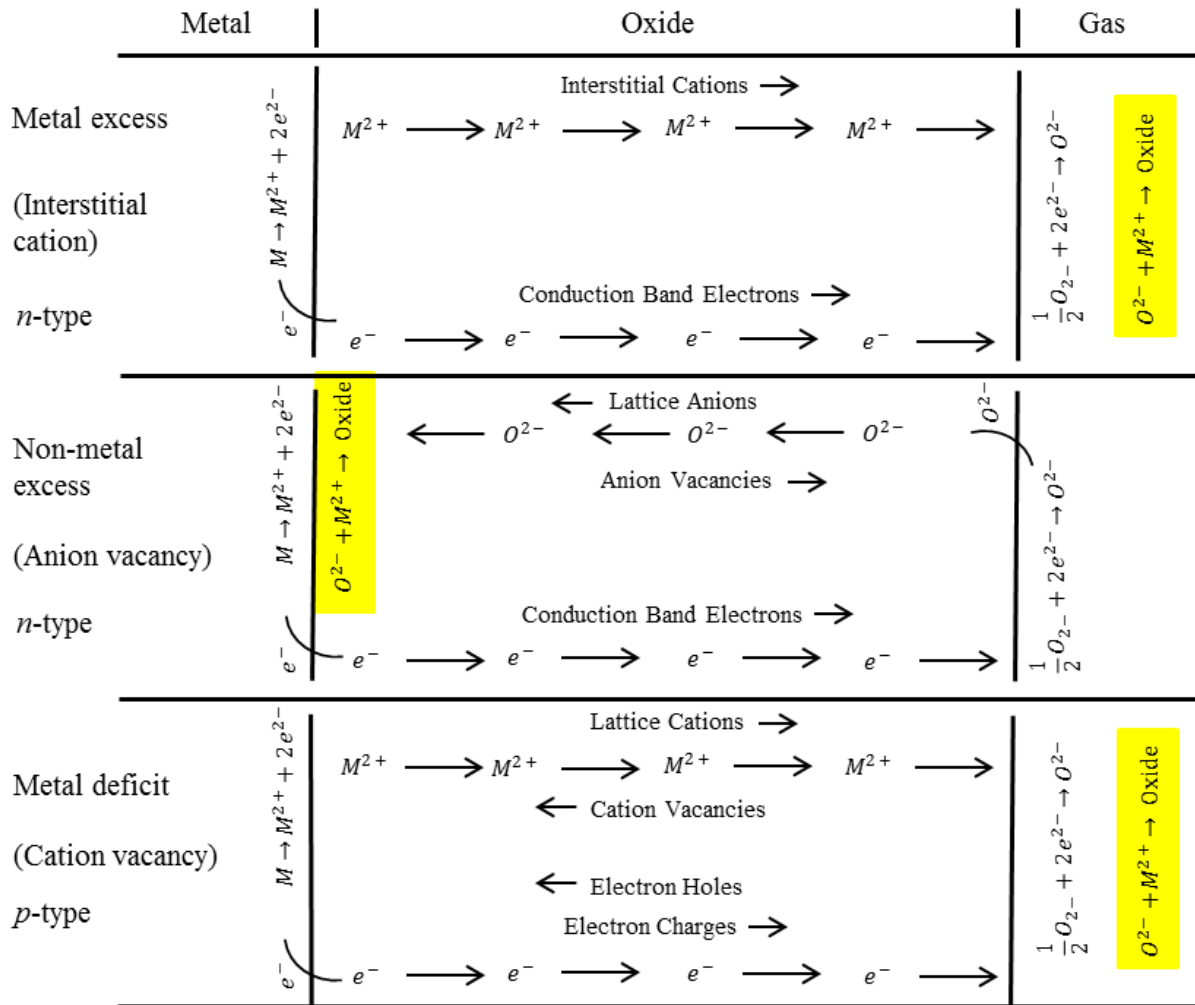


Figure 1-4: Processes occurring in three types of oxide surface scale during oxidation (a) interstitial cation, (b) anion vacancy, and (c) cation vacancy. Based on Figure 12.13 from Jones [42].

Oxidation is often classified based on the rate dominant steps, either diffusion-controlled [6,10-12,35,37] and/or boundary-controlled mechanism [6,9,35]. In a boundary-controlled process, oxidation is progressed by initiating the reaction at new interfaces and beginning nucleation of an oxide. In diffusion-controlled conditions, the oxidation rate is limited by the movement of oxygen or metal species through the reaction layer.

Oxide scales are stronger in compression than in tension [42]. It is possible for volumetric differences to develop between the matrix and oxide scale during thermal changes. In boundary-controlled oxidation, these thermal changes can cause tensile stress that lead to severe cracking within the microstructure which provide fast-track pathways for the oxygen to penetrate deeper into the material and accelerate oxidation. This cracking caused by high thermal expansion ratio differences is often characterized by the Pilling-Bedworth ratio (R_{PB}), which is the ratio of oxide volume to matrix volume. Typically R_{PB} ratios between 1 and 2 are considered favorable for forming protective oxide scales [44]; ratios above 2 lead to an un-protective oxide scale and spalling [7] while ratios below 1 are considered to produce oxide scales that are too thin [45]. Hafnium has a R_{PB} of 1.62 whereas tantalum is 2.47 [45]. In oxidation and corrosion, protective scales are often characterized by the ability to act as a passive film. Hence the formation of an adherent protective oxide scale is essential as it provides a barrier to rapid oxidation and spalling.

Oxidation of the Hf_xN_{1-x} System

The hafnium nitrides have been reported to exhibit both oxidation mechanisms. For example, a diffusion-controlled monoclinic hafnia oxide scale has been shown to form on Hf-N specimens below 800°C [9,46-47]. During oxidation, nitrogen liberation occurs, as seen in equation 4. The oxide scale formation reaction is limited by diffusion based mechanisms. The low plasticity of the oxide scale formed on the ceramic matrix exterior prevents the relaxation of stresses caused by the thermal expansion ratio differences between δ -HfN and HfO₂ [9]. This leads to cracking within the ceramic matrix, where boundary-controlled mechanisms initiate, and de-cohesion of the scale spalling [7].



In addition, hafnium oxide has three polymorphs, which are α -HfO₂ (monoclinic $P2_1/c$), β -HfO₂ (tetragonal $P4_2/nmc$) at 1670°C, and δ -HfO₂ (cubic $Fm\bar{3}m$) at 2200°C [48]. These

additional transformations of the oxide scale complicate the stress state behavior and adhesion. In contrast, other reports have shown that HfN's oxidation is slowed between 800 and 1000°C because of a possible intermediate oxy-nitride phase with similar kinetic behavior as the monoclinic hafnia [9,46-47] making it adherent, as suggested by similar transition metal carbide systems (Zr, Ta, Nb, V) [17,22,49]. It has been previously reported that oxidation in transition metal carbides, for example, can be reduced when particular phases within a scale can form [6,10-12,35,37].

It was hypothesized that this oxy-nitride scale is more favorable for the hafnium-rich nitrides than that of the δ -HfN. For example, in the M_2X materials (Ta_2C) [6] vacant layers of X atoms in the hexagonal M_2X structure are suspected sites where oxygen atoms can reside and form an oxy-X scale [6]. This has been proposed for oxygen dissolved in carbides that form an oxy-carbide, $MC_{1-x}O_x$, scale [6,9,11]. As x increased in the oxy-carbide, i.e. more oxygen, the oxy-carbide saturated and eventually produced MO_2 and MO crystallites [11]. As this oxy-carbide thickened at a parabolic rate, it acted as a diffusion barrier for oxygen.

Like the hexagonal M_2X structure, the rhombohedral ϵ - Hf_3N_2 and ζ - Hf_4N_3 symmetries offer similar vacant layers and are believed to contribute to easier stabilization of an oxy-nitride scale as compared to δ -HfN. In addition, the close-packed nature of the structure could also hinder matrix based diffusion by providing anion vacancy wells.

Oxidation with tantalum additions

A major concern of group V UHTCs with tantalum is its ready oxidation into Ta_2O_5 [50]. Tantalum oxide also has three main polymorphs, which are orthorhombic L- Ta_2O_5 ($Pmm2$) [51], triclinic β - Ta_2O_5 ($P\bar{1}$) that is stable between 700°C and 1320°C, and monoclinic α - Ta_2O_5 ($C2/m$) which melts at 1872°C [52]. The tantalum-ceramics suffer from diffusion-controlled and boundary-controlled oxidation; it forms a porous oxide scale that has a low melting temperature, below 1900°C [50], and fails due to non-dense oxide scale spalling [10]. Yet, it has been previously reported that oxidation in transition group V carbides can be reduced when particular phases within the scale can form, such as the close-packed hexagonal γ - Ta_2C [6,10-12,53]. It was believed that this phase limited oxidation by controlling and minimizing diffusion through the reaction layer.

Processing and Characterization

The range of Hf-N and Hf-Ta-N specimens were fabricated by two primary routes - hot isotactic pressing (HIP) and vacuum plasma processing (VPS) through collaborations with Exothermics, Inc. and Plasma Process, LLC. The HIP process is a reaction based 'bottom up' process where constituent powders are mixed and sintered under pressure and temperature. In VPS, constituent powders are melted under a plasma plume and re-solidified onto a graphite mandrel and is considered a 'top down' process. In the VPS process, the as-sprayed material is then consolidated through a sintering and can-less HIP process. In previous work, Morris *et al.* [31-32] reported that these subsequent steps of consolidation of the VPS material resulted in similar microstructures as the bottom up HIP process. The significant difference was that the VPS material tended to have smaller grain sizes since the solidification of the molten splat yielded smaller starting grain sizes as compared to powder mixtures of the HIP.

A Sentro Tech Corp 1700 2.5-6 High Temperature Tube Furnace was used to oxidize the samples. This furnace allows atmospheric heating up to 1700°C heating temperatures. Samples' mass was weighed prior to and post oxidation treatment to determine mass loss or gain.

The research work relied heavily on the use of analytical characterization techniques such as electron microscopy. Electron diffraction is advantageous because of the large ratio in electron scattering in ceramics, simplicity of pattern detection from zone axis symmetry, selected area diffraction from individual grains or phases, and bright field and dark field imaging for unambiguous structure analysis and deformation mechanism determination. Bright and dark field imaging was conducted on a FEI F20 Tecnai transmission electron microscope (TEM), operated at 200 keV. The High Angle Annular Dark Field (HAADF) detector was used for Z-contrast imaging in the scanning transmission electron microscope (STEM) mode. The Z-contrast imaging observed is chemically dependent with higher atomic number elements being brighter since the HAADF collects scattered electrons that are insensitive to crystallographic dependent scattering [54]. This was advantageous in identifying particular phases and oxides in the material. TEM specimens were prepared using a focus ion beam (FIB) microscope milling technique which will allow for site specific extraction and thinning [55-56].

Microstructure characterization and imaging was also performed using a FEI Quanta 3D dual scanning electron (SEM) FIB microscope. The images were collected in either an ion contrast imaging condition or secondary electron (SE) conditions. The specimen phase

composition, grain size, and microstructure orientation was quantified using an Electron Backscattered Diffraction (EBSD) patterns taken on an EDAX-TSL Hikari camera platform attached to the Quanta 3D. Porosity fraction was quantified using the Delesse Principle which compares the surface area fraction of the total pore count divided by the total surface area of the image [57].

The phase identification was also done by X-ray diffraction (XRD) using a Bruker D8 Discovery General Area Diffraction Detector System (GADDS) using Cu-K α radiation at 45 keV and 40 mA as the source. The collected peaks were compared with the lattice structure data in the ICDD cards [58-61] as well as reported crystallographic data from literature [24]. Prior to XRD analysis, the specimens were crushed and ground using a mortar and pedestal which ensured a random texture and sufficiently large sampling volume from the powder particulates.

Dissertation Organization

The remainder of this work describes key findings of the hafnium nitride microstructure and phase evolution along with the oxidation of hafnium-tantalum nitrides. The dissertation is organized in a journal paper format, per the guidelines of The University of Alabama's Graduate School. Chapter 2 is a discussion on the resulting microstructures and phase orientations of the metal-rich hafnium nitrides from a hot-isostatic pressed diffusion couple. The next section, Chapter 3, progresses the conversation to VPS as-sprayed ternary hafnium-tantalum nitrides and their oxidation behavior during various heat treatments between 400°C to 1600°C. Chapter 4 further analyzes possible oxy-nitride intermediate layers for an 80(HfN)-20(TaN) (wt.%) nitride with VPS and sinter/HIP processing. Chapter 5 is a summary of the results from the research and suggestions for future work.

CHAPTER 2

Phase and Microstructure Relationships in Hf-N

Bradford C. Schulz¹, Steve DiPietro², and Gregory B. Thompson^{1,#}

¹ Department of Metallurgical & Materials Engineering,
The University of Alabama
301 7th Avenue, 116 Houser Hall
Tuscaloosa, AL 35487-0202 (United States of America)
(205) 348-1589

² Exothermics, Inc.
14 Columbia Drive
Amherst, NH 03031 (United States of America)
(603) 732-0077

Contact author: gthompson@eng.ua.edu

Abstract

Two sets of hafnium nitride diffusion couples were processed by hot-isostatic pressing and their resulting microstructure and phase orientation were identified. Distinct regions were found in the diffusion couples. The first diffusion couple heat treated at 1900°C at 200 MPa and 2 hrs revealed a combined phase region of ϵ -Hf₃N₂ grains with α -Hf laths, a dominant ζ -Hf₄N₃ grain region, and a mixed δ -HfN grains with ζ -Hf₄N₃ laths region between the initial α -Hf and δ -HfN diffused materials. The second diffusion couple heat treated at 1200°C at 200 MPa and for 12 hrs revealed similar regions except the mixed δ -HfN grains with ζ -Hf₄N₃ laths region was not present. Instead, the reaction zone transitioned directly from the initial δ -HfN to a mixed ϵ -Hf₃N₂ and ζ -Hf₄N₃ region. It was shown that the rhombohedral ζ -Hf₄N₃ phase, like other M₄X₃ UHTCs, formed through elemental migration along close-packed planes from FCC structures. Lattice parameter calculations from the high temperature diffusion couple verified homogeneity ranges of ϵ -Hf₃N₂ and ζ -Hf₄N₃.

Keywords

Ultra-high temperature ceramics, hafnium nitride system, hot-isostatic pressing, diffusion couple

Introduction

Ultra high temperature ceramics (UHTC) constitute a class of materials characterized by high melting points, chemical inertness, high hardness, and moderate oxidation resistance [1-2,62]. These ceramics typically comprise either group IV or V metals bonded with boron, carbon or nitrogen [2]. When in equal atomic ratio, a MX compound will nominally form, where M is the metal species and X the interstitial light element (boron, carbon, or nitrogen). Dependent on the light species type, the group IV and V metals can precipitate of metal-rich M_6X_5 , M_4X_3 , M_3X_2 , and/or M_2X compounds. The precipitation of these phases have a dramatic influence on the microstructure's grains' morphology [1-2,5,31-32] and properties, including mechanical [22,63], electrical [23] and oxidation [10,15]. Intrinsic to microstructure manipulation, i.e. properties, is regulating the precipitation and growth of secondary phases. For example, in tantalum carbides, the precipitation of the Ta_4C_3 phase from TaC results in a crisscross pattern of laths within equiaxed grains whereas Ta_4C_3 's precipitation from Ta_2C results in the laths parallel to each other and along the major axis of acicular grains [32]. To engineer microstructures, elucidating the nucleation and growth sequence of phase precipitation is essential for manipulating structure-property interrelationships. In the current work, the microstructure formations between various hafnium nitride phases are explored to determine what microstructure morphologies are present in multiphase fields and how such microstructures evolved.

For the Hf-N system, the incorporation of nitrogen strengthens the intrinsic bonding in hafnium evident by the increase in melting temperature of the hexagonal close packed (HCP) α -Hf phase ($P6_3/mmc$) from 1743°C to 2910°C [26,38,41], Figure 2-1(a). From approximately 43 at.% N to slightly above 50 at.% N, the mononitride δ -HfN is stable with the B1 or face-centered cubic (FCC) based rock-salt crystal structure ($Fm\bar{3}m$). It is interesting to note that this phase is stabilized for slightly nitrogen-rich compositions. Upon reduction of nitrogen, the mononitride phase can become thermodynamically unstable and result in the precipitation of hafnium-rich nitrogen phases. There has been debate about which phases are stable in these metal-rich compositions. It was previously believed that only a hexagonal-based Hf_2N structure was present between α -Hf and δ -HfN [38]. However, Rudy *et al.* revised these earlier findings [13] and established that two rhombohedral phases ($R\bar{3}m$), ζ - Hf_4N_3 and ϵ - Hf_3N_2 , existed and Hf_2N was not present [27]. This confusion lies in that these phases have very similar stacking sequences to

each other [64]. When the M_2X structure is generically represented in a HCP setting, the different stacking sequences of the metallic atoms result in different spatial arrangements of the octahedral interstices, where the light element X resides. The octahedral interstices form straight chains running parallel to the c -axis with vacancies and interstitial atoms alternating along these chains [27], Figure 2-1(b) [39]. In contrast, larger spacing's can exist between interstitial sites in the FCC based MX phases [27] where all the light element sites may be occupied. Since both types of interstitial atom packing are possible, *i.e.* HCP verses FCC, in the ϵ -Hf₃N₂ and ζ -Hf₄N₃ structures, this lead to the apparent confusion. In ζ -Hf₄N₃, the nitrogen resides in three hexagonal based interstitial sites and two cubic based interstitial sites along the c -axis [27,64], Figure 2-1(b). For the ϵ -Hf₃N₂, the nitrogen resides in three hexagonal and one cubic interstitial site, Figure 2-1(b). These subtle nitrogen stacking sequence changes results in the precipitation of nano-laminate phases [16]. Figure 2-1(a) suggests that the ζ -Hf₄N₃ phase is stable only at elevated temperatures in excess of approximately 1225°C and decomposes into either the ϵ -Hf₃N₂ or δ -HfN at lower temperatures. These metal-rich nitrogen phases exist between 33 to 47 at.% N, which is between the α -Hf and δ -HfN phase fields in Figure 2-1(a).

To date, there has not been a rigorous study of how phase content controls the microstructure in the Hf-N system. This is surprising considering that the metal-rich nitride phases appear to intrinsically regulate the self-organization of nitrogen to specific interstitial sites and can precipitate out nano-laminate phases [16] which could be strengthening mechanism in the microstructure. How these phase changes occur and precipitate within the matrix needs to be addressed. Diffusion couples have been fabricated between α -Hf and δ -HfN under hot-isostatic pressing (HIP) conditions to determine the phase transformation pathways that lead to the types of microstructures that form in Hf-N. HIP is commonly used as a fabrication method for UHTCs and would provide a direct comparative study in processing-structure relationships on how various multiphase microstructures form.

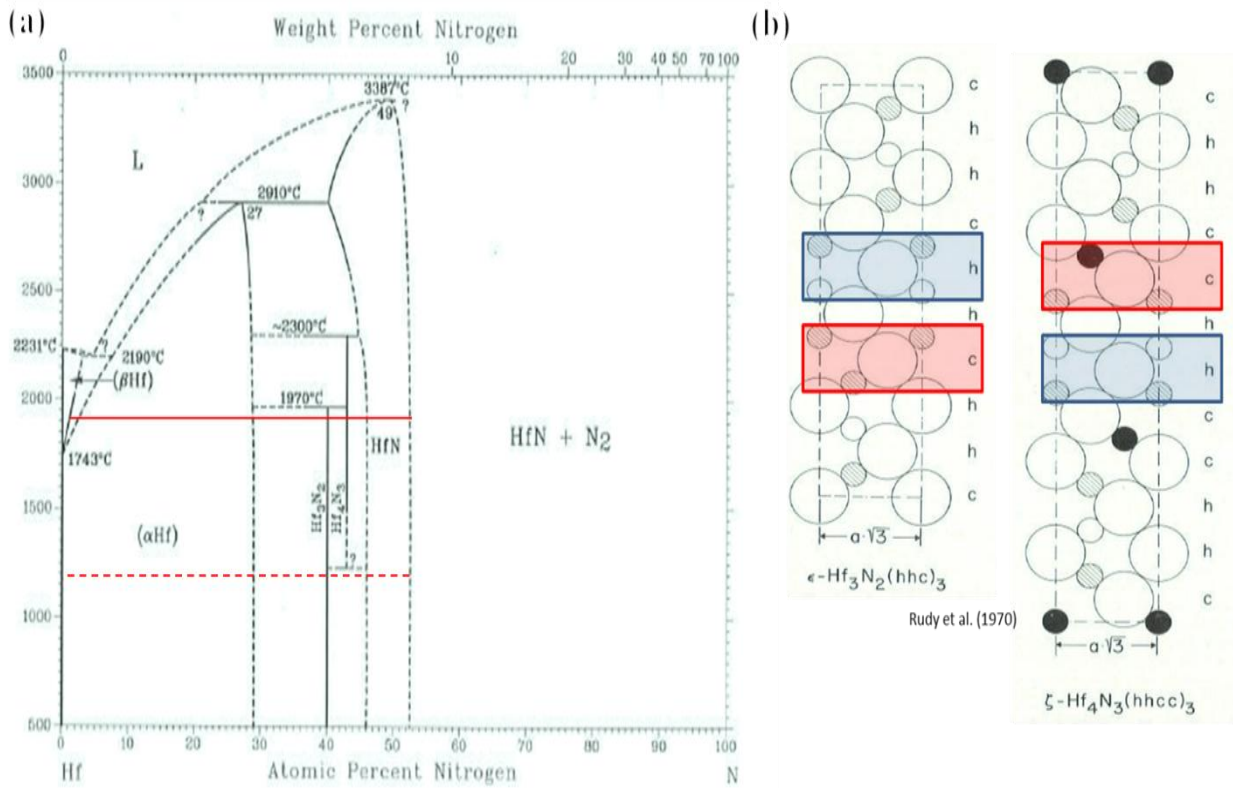


Figure 2-1: (a) Phase diagram of Hf-N system [3] with red lines indicating 1900°C (solid) and 1200°C (dashed). Crystallographic (11 $\bar{2}$ 0) view (b) of ζ -Hf₄N₃ and ϵ -Hf₃N₂ demonstrating alternating hexagonal (h) and cubic (c) layers bonded along the interstitial [27].

Experimental Procedure

HIP is a reaction based 'bottom-up' process where constituent powders are mixed and sintered under pressure and temperature. The diffusion couple specimens were fabricated by reacting α -Hf powder that encased a previously prepared δ -HfN monolith. The mixture of starting materials were all placed in a vacuumed sealed tantalum container prior to HIP processing to eliminate extraneous contamination. Two diffusion couples were processed at either 1900°C for 2 hrs at 200 MPa or 1200°C for 12 hrs at 200 MPa. This process difference was to explore the stability of the ζ -Hf₄N₃ formation denoted as the dashed lines in Figure 2-1(a).

Post-HIP, the nitride specimens were mechanically cut and ground from the tantalum canisters. The interior portions of these cross-section surfaces were then polished with 3 micron diamond abrasive paste with a final Vibromet® polish for 24 hrs in aqueous 0.05 micron silica slurry to reveal the microstructure.

Each specimen was characterized using electron microscopy and X-ray diffraction. The specimen microstructure and phase identification within the microstructure was quantified by Electron Backscattered Diffraction (EBSD) using an Oxford Instruments NordlysNano camera platform attached to a JEOL 7000 field emission scanning electron microscope (SEM). Besides EBSD, secondary electron imaging of the surface on the SEM was employed. The phase content was also identified by X-ray diffraction (XRD) using a Bruker D8 Discovery General Area Diffraction Detector System (GADDS) operating with Cu-K α radiation at 45 keV and 40 mA as the source. The collected peaks were compared with the lattice structure data from the ICDD database and reported crystallographic data [27,65-66]. The XRD scans consisted of line scans over the reaction zone between the α -Hf and δ -HfN interface using a 0.8 mm source spot size and a 0.01 mm step between each scan, Appendix A. The reported accuracy of significant figures is based on the 2- θ step.

Results

Figure 2-2 contains EBSD image quality, phase identification, and orientation maps formed from the reaction of α -Hf with δ -HfN at a HIP temperature of 1900°C. Five distinct regions have been identified and correspond to the following:

- [A] α -Hf grains
- [B] ϵ -Hf₃N₂ grains with α -Hf laths
- [C] ζ -Hf₄N₃ grains

[D] δ -HfN grains with ζ -Hf₄N₃ laths

[E] δ -HfN grains

This diffusion couple reveals very distinct boundaries between each of the phase fields between each region. There does not appear to be a gradual change from one regional microstructure to another. The α -Hf grains, [A], transitions almost directly to a two phase columnar grain region consisting of α -Hf laths encased in a primarily ϵ -Hf₃N₂ matrix, denoted as [B]. Within [B], all of the identified α -Hf laths, Figure 2-2(b), have a 60° misorientation within the ϵ -Hf₃N₂ matrix, Figure 2-2(c). With further increase in nitrogen content, region [B] abruptly transitions to a narrower, but distinct granular ζ -Hf₄N₃ region, [C]. With further nitrogen enrichment, [D], the δ -HfN is present as equiaxed grains containing laths of ζ -Hf₄N₃. It was observed that the ζ -Hf₄N₃ laths were misorientated by 54.75° with respect to the δ -HfN matrix and by 70.5° to each other within this region. Lastly, the reaction zone concludes with equiaxed single phase δ -HfN grains in [E].

XRD line scans across the reaction zone confirmed the evolution of phase content. By plotting the XRD intensity as a function of diffraction angle, 2θ , and line scan distance, an accurate measurement of each phases' lattice parameters was achieved. From the EBSD images, the reaction zone is approximately 0.15 mm whereas the XRD spot is approximately 0.8 mm; this ensures that the X-ray sampling volume contain multiple phases' diffraction peaks [27,65-67]. As seen in Figure 2-3(a), as the X-ray probe scanned across the interface, specific unique phase peaks increased and decreased in intensity as well as shifted in 2θ space. The peak intensity variations are contributed to the change in phase content's volume fraction whereas the peak shift is associated with the lattice parameter response with nitrogen content. Since many of these phases are not cubic (or have a single lattice parameter), the convoluted “*” $[hk0]$ peak was also used to determine the c -lattice parameter for those phases [19]. A careful review of this “*” peak's diffraction angle range, Figure 2-3(b), showed that it too shifts as a function of distance. When the peak intensity, unique peaks for a - and “*” for c -, was a maximum in 2θ , this was taken to be the ideal stoichiometric lattice parameter and is tabulated in Table 2-1. Since these peaks also shifted, the lattice parameter associated with the minimum intensity on either side of the maximum intensity position is also given and tabulated as a range in Table 2-1. This shift in lattice parameter provides insights into the possible range of nitrogen stoichiometry for these compounds.

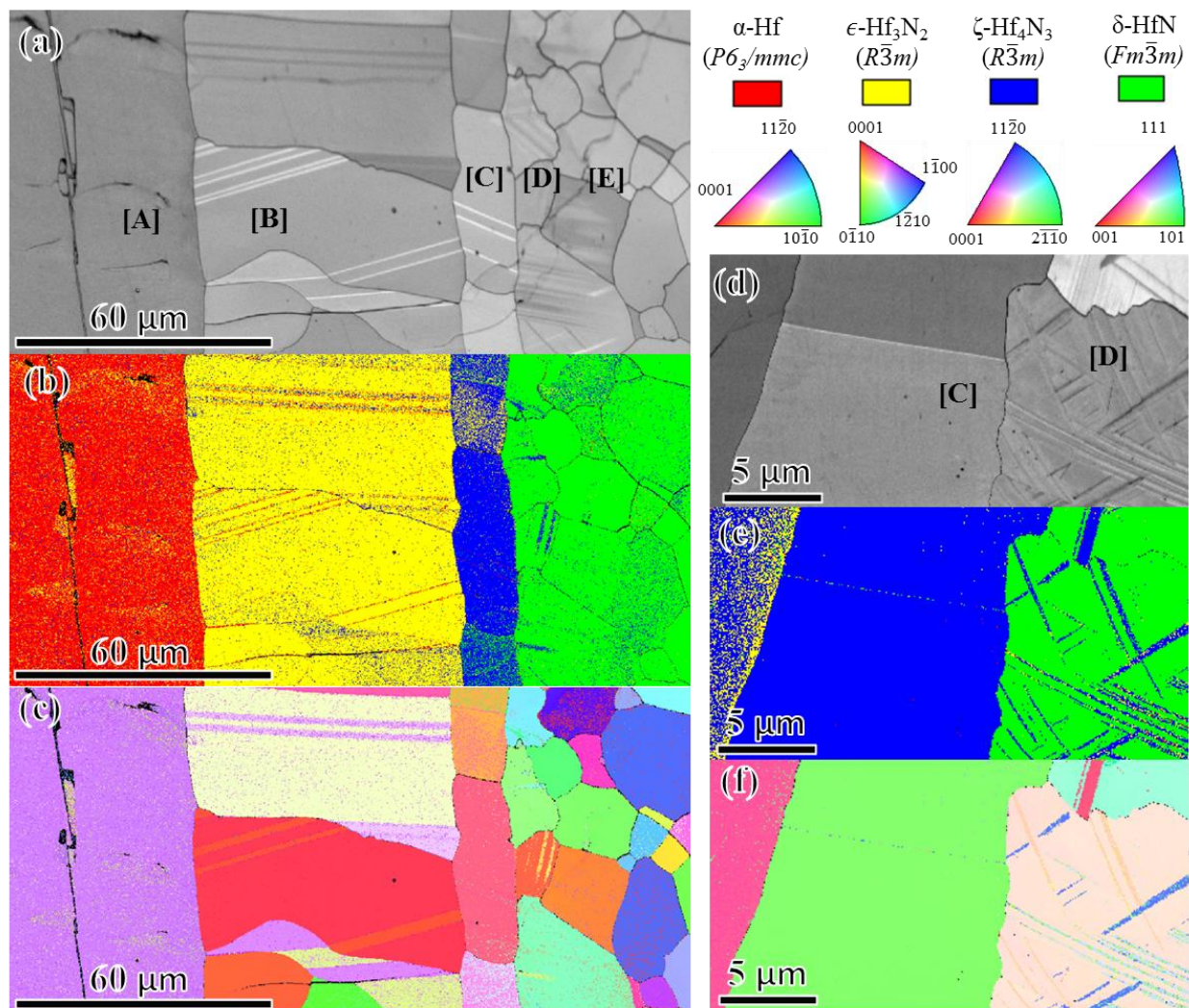


Figure 2-2: EBSD of the 1900°C diffusion couple with locations of regions [A]-[E] approximated on the (a) image quality reconstructed map. (b) Phase identification for the reaction zone based on the diffraction data. (c) Orientation mapping for the reaction zone. Magnified region [C] and [D] image (d) quality map, (e) phase identification, and (f) crystallographic orientation.

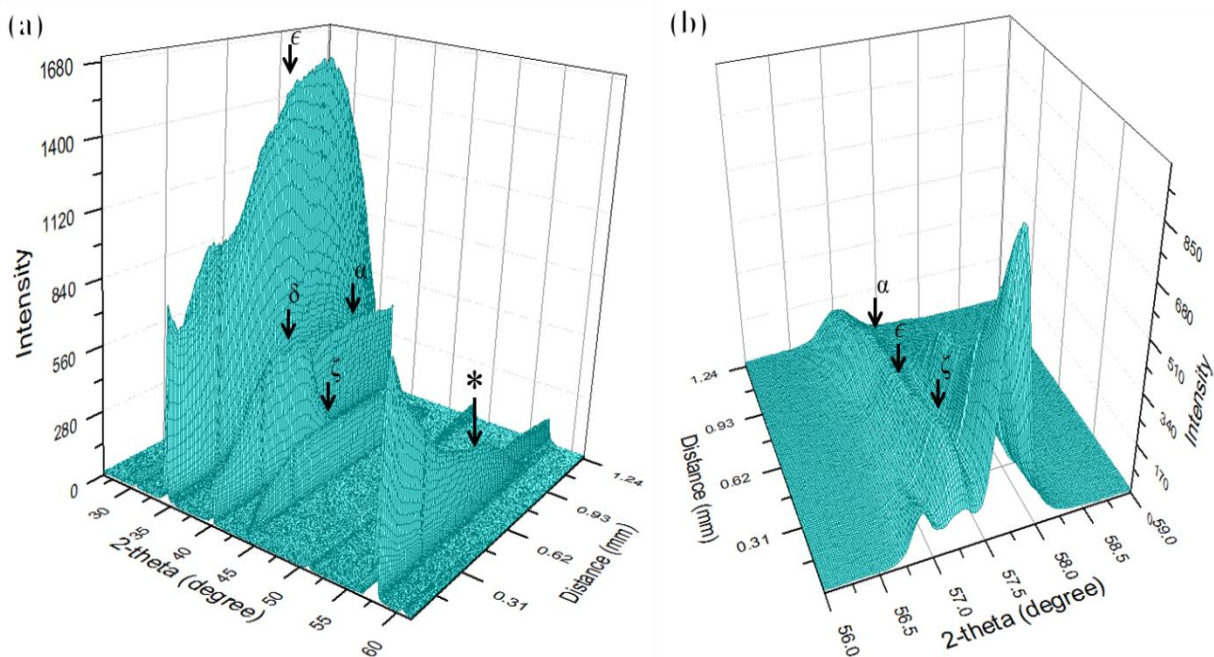


Figure 2-3: XRD line scan of the 1900°C diffusion couple with a step size of 0.01 mm. The unique peak maximums for each phase are indicated on (a), the $[10\bar{1}1]$ peak for α -Hf (McMurdie^[65]), the $[0009]$ peak for ϵ -Hf₃N₂ (Rudy^[27]), the $[00015]$ peak for ζ -Hf₄N₃ (Rudy^[27]), and the $[200]$ peak for δ -HfN (Fiala^[66]). Note the peaks begin at δ -HfN and progress towards α -Hf. (a) Entire image with x- 2θ (25°-60°), y-distance (0.00-1.25 mm), and z-intensity. Same line scan (b) from 56°-59° arranged to depict the additional $[hk0]$ peak, the $[11\bar{2}0]$, for c -lattice parameter calculations.

Chemical Formula Crystal System Space Group	Hf Hexagonal <i>P63/mmc</i> (194)			HfN _{0.67} Rhombohedral <i>R3m</i> (166)			HfN _{0.75} Rhombohedral <i>R3m</i> (166)			HfN Cubic <i>Fm3m</i> (225)		
	Calculated		McMurdie	Calculated		Rudy	Calculated		Rudy	Calculated		Fiala
	Minimum	Maximum		Minimum	Maximum		Minimum	Maximum		Minimum	Maximum	
a (nm)	0.3190	0.3193	0.3196	0.3214	0.3218	0.3206	0.3214	0.3215	0.3214	0.4504	0.4511	0.452
c (nm)	0.5259	0.5254	0.5058	2.343	2.343	2.326	3.109	3.107	3.1120	0.4504	0.4511	0.452

Table 2-1: Calculated lattice parameters from the XRD line scan for α -Hf, ϵ -Hf₃N₂, ζ -Hf₄N₃, and δ -HfN compared with prior findings (McMurdie^[65], Rudy^[27], and Fiala^[66]). The calculated lattice parameters were derived from the minimum and maximum 2θ values based on intensity-distance relationships from Figure 2-3(a).

Figure 2-4 is the EBSD-based micrographs for the 1200°C processed HIP specimen. Similarly, the following five regions have been identified as the following:

- [A] α -Hf grains
- [B] ϵ -Hf₃N₂ grains with α -Hf laths
- [C*] ζ -Hf₄N₃ and ϵ -Hf₃N₂ grains
- [E] δ -HfN grains

Region [C*] is denoted with an asterisk because it similar to region [C], which contains ζ -Hf₄N₃, from the 1900°C specimen but also ϵ -Hf₃N₂. Since this 1200°C specimen does not contain a ζ -Hf₄N₃/ δ -HfN region, as seen in the 1900°C's [D], it is omitted and the labeling continues with [E], the δ -HfN grains, which was common to both specimens. This labeling scheme maintains consistency between the two micrographs, Figure 2-2 and Figure 2-4, for comparative purposes. Similar to the previous result in Figure 2-2, distinct boundary existed between each of the phase field regions. The α -Hf appears to uptake nitrogen where upon the precipitation of ϵ -Hf₃N₂ forms within these grains, and was noted to have lath morphologies indicted by the arrows in Figure 2-4(b). It is interesting to note that these higher nitrogen containing Hf-based grains, [B], appear to be columnar as compared to the equiaxed grains of α -Hf. This change in grain morphology was noted in both region [B]'s for each specimen. With continual nitrogen diffusion from δ -HfN towards α -Hf, a refined ϵ -Hf₃N₂ grain structure formed, [C*]. But unlike the 1900°C [C] region, where the grains where predominately ζ -Hf₄N₃, these grains were primarily ϵ -Hf₃N₂. Upon closer inspection of 1200°C's [C*], a gradient in the ζ -Hf₄N₃ and ϵ -Hf₃N₂ phases is present and lath morphologies between the two phases is evident, indicated by the arrows in Figure 2-4(b) within [C*]. Surprisingly, a region of δ -HfN with laths of ζ -Hf₄N₃ was not observed like as in [D] of Figure 2-2. Rather only single phase δ -Hf grains were evident, [E], in Figure 2-4.

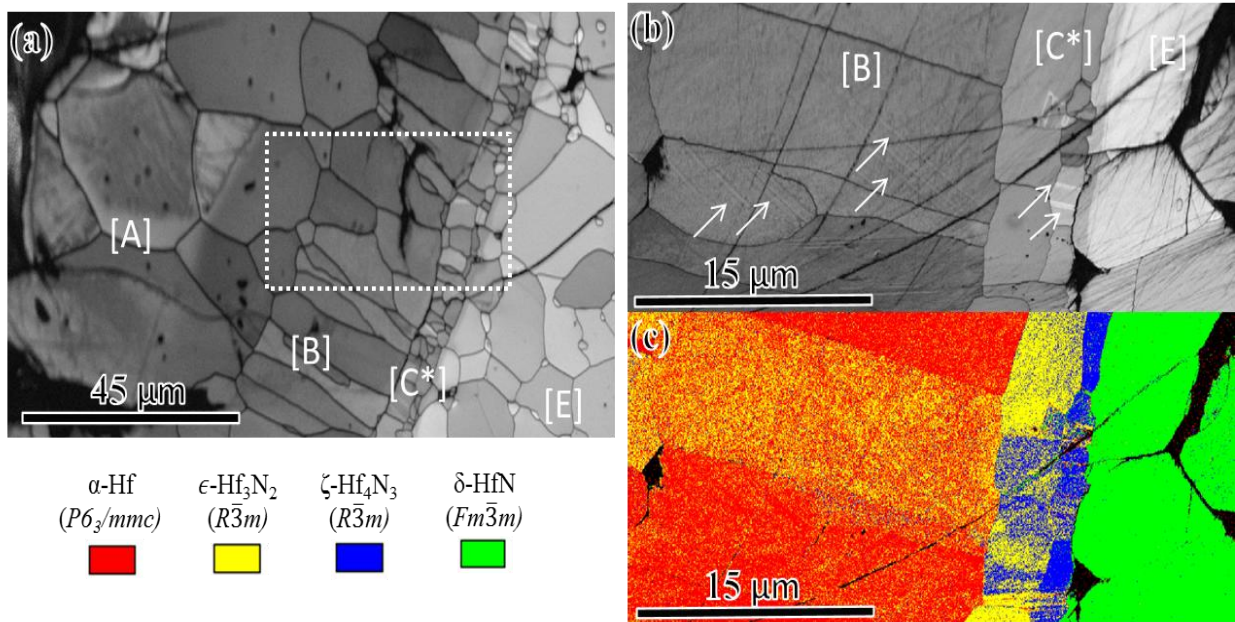


Figure 2-4: EBSD of the 1200°C diffusion couple with locations of regions [A], [B], [C*], and [E] approximated on the (a) image quality reconstructed map. (b-c) Approximate magnified region of [B], [C*], and [E] from (a). The (b) image quality map demonstrating lath microstructures indicated by the arrows and (c) is the phase identification map.

Discussion

In both diffusion couples, distinct phase regions were present. Nitrogen, being the smaller atom that resides in the interstitial sites of the metal lattice, will diffuse faster than the hafnium. In region [D] for the 1900°C specimen, precipitation of the ζ -Hf₄N₃ occurs within the δ -HfN matrix. Based on the orientation relationship, the close packed planes of each phase are parallel with each other. In the δ -HfN rock salt structure, alternating close pack {111} planes of hafnium and nitrogen exist along the $\langle 111 \rangle$ direction. It was observed that the ζ -Hf₄N₃ laths were misorientated from each other by approximately 70° and by 55° with respect to the δ -HfN matrix. As seen in other UHTC's, it is common for M₄X₃ to precipitate out of FCC structures (like δ -HfN) along the close-packed {111} planes [31-32]. These FCC close-packed planes have a 70.5° misorientation with each other and a 54.74° misorientation with the base {002} plane. This would suggest that the ζ -Hf₄N₃ phase forms laths similarly where nitrogen is depleted along δ -HfN's close-packed planes. With the diffusion of nitrogen from δ -HfN in the diffusion couple, these nitrogen planes will become depleted and eventually absent in the crystal structure. If there is a subsequent loss of every fourth nitrogen {111} plane, the two hafnium metal {111} planes now placed into contact with each other will shear. This sequence will yield the correct composition and symmetry of the ζ -Hf₄N₃ phase [32,68]. Consequently, the ζ -Hf₄N₃ formed laths with the observed orientation relationship. Since δ -HfN also has four equivalent {111} planes, the crisscross ζ -Hf₄N₃ morphology, with a 70° misorientation from each other, develops within δ -HfN grains. At the lower temperature diffusion couple, the morphology of crisscross laths was not observed in the same region.

The precipitation of ϵ -Hf₃N₂ laths in the 1200°C in an equivalent region as [D] at 1900°C could be expected. The ϵ -Hf₃N₂ phase has the same rhombohedral symmetry as ζ -Hf₄N₃ and would likely follow the same phase transformation pathway described above except with every third close packed {111} nitrogen plane being depleted with the subsequent hafnium-hafnium close packed plane shear. Surprisingly, these metal-rich precipitates were not observed within the δ -HfN matrix; this may be a result of the lower process temperature which was insufficient to coarsen the phase sufficiently to be resolved by the spatial resolution of the EBSD technique. The ζ -Hf₄N₃ and ϵ -Hf₃N₂ phases were clearly observed as a distinct mixed phase region next to the δ -HfN, [C*], Figure 2-4. In this region, a gradation of ζ -Hf₄N₃ and ϵ -Hf₃N₂ phases was present. According to Figure 2-1(a), ζ -Hf₄N₃ is not thermodynamically stable at the 1200°C

processing temperature. The presence of ζ -Hf₄N₃ for this specimen is contributed to its formation either under the high pressure of HIP'ing (note the phase diagram of Figure 2-1(a) assume 1 atm) or its structural similarity to ϵ -Hf₃N₂, the thermodynamically stable phase. The interstitial arrangement of the nitrogen atoms between ζ -Hf₄N₃ and ϵ -Hf₃N₂ is subtle, Figure 2-1(b) [27,64]; it could be expected that this ζ -Hf₄N₃ phase is an intermediate metastable phase formed during the phase transformation to leaner nitrogen phase. Note that the ζ -Hf₄N₃ phase was spatially closer to the δ -HfN grains, where the nitrogen content would be higher. In this mixed ζ -Hf₄N₃ and ϵ -Hf₃N₂ region, the phases' exhibit lath like morphologies with each other indicated by the arrow in Figure 2-4(b). Since both phases share the same symmetry, they maintain a close packed plane orientation relationship with each other, as previously described above. Since the rhombohedral structure has one basal plane, these laths are parallel to each other in only one direction within each grain. Finally, within this mixed region the grains are refined compared to the surrounding grains. This is suggestive that these phases are not consuming existing larger grains. Rather the diffusing hafnium and nitrogen, likely along a fast-track grain boundary pathway, react and undergo a discontinuous precipitation process [69] and form these phases which develop into these refined grains that contain the metal-rich phases. Since these refined grains are much smaller than the surrounding grains, it is not clear whether these phases are forming within a larger grain and subsequently consuming it. Based on the orientation relationship of these phases with either α -Hf or δ -HfN, the metal-rich phases precipitate as laths that span the larger grain rather than precipitating as small, self-contained volumes within the larger grain. This type of reaction pathway is suggestive of a processing means of fabricating smaller grains with these lath phases and is the subject of future investigations. Based on the 1900°C couple, where the [C] ζ -Hf₄N₃ zone was narrow, the refinement of the grains may strongly be dependent on the precipitation of this phase rather than ϵ -Hf₃N₂.

In contrast, the region next to this refined grain structure, the [B] ϵ -Hf₃N₂ grains, were larger in spatial extent. This was observed for both couples. The ϵ -Hf₃N₂ phase within this grain is suspected to have formed from the rapid diffusion of nitrogen from δ -HfN into the larger α -Hf metal grains. Since α -Hf can accommodate a significant amount of nitrogen in solid solution, Figure 2-1(a), no precipitation occurred and the grains remained large. Once a critical amount of nitrogen was absorbed, the ϵ -Hf₃N₂ phase precipitated and consumed the prior grain. Since nitrogen is abundantly present in the α -Hf grain, precipitation could occur throughout the grain.

This is clearly evident viewing the center grain in region [B] of Figure 2-4(c)'s micrograph which shows a mixture of α -Hf and ϵ -Hf₃N₂ phases. At 1900°C, this mixture was not as evident because the higher temperature being sufficient to nearly transform the prior α -Hf grain to ϵ -Hf₃N₂; though some remnants of α -Hf are still present in these grains indicated by the thin α -Hf laths in [B] of Figure 2-2(b). These remnant α -Hf laths run parallel to each other and align in a single orientation within each grain because ϵ -Hf₃N₂ and α -Hf each have a single close packed plane variant to each other.

A peculiar feature of these [B] region grains is their columnar or acicular shape. In the image quality maps of Figure 2-2 and Figure 2-4, it is clear that the laths run parallel or relatively parallel to the columnar grain length. The close packed orientation relationship of the two phases during the phase transformation may also influence the observed grain morphology change. Note that the diffusivity coefficients of light element interstitial species in HCP-based structures are anisotropic in and out of the basal plane [70]. These diffusivity differences will affect the nucleation and growth rate direction of the new phase forming within the grain. Considering the alignment or near alignment of the laths along the long axis of the columnar grains is suggestive that the phase transformation pathway maybe influencing the grain morphology. This has been observed in the precipitation of Ta₄C₃ in Ta₂C, which also has a similar orientation and lath morphology to this system. In the carbide system, these multiphase grains were acicular with the laths running parallel to the major axis of the grain [31-32]. In contrast, the surrounding carbide grains remained equiaxed.

According to the phase diagram of Figure 2-1(a), the ζ -Hf₄N₃ and ϵ -Hf₃N₂ phases are line compounds. For sub-stoichiometric phases, like δ -HfN, the lattice parameter shifts with nitrogen content. The XRD lattice parameters for the ζ -Hf₄N₃ and ϵ -Hf₃N₂ phase show some variation along the reaction zone. These shifts could suggest that these phases are not line compounds but rather accommodate some sub-stoichiometric of nitrogen content. Lengauer *et. al.* [71] also suggested that these phases are not line compounds and revised a phase diagram of Okamoto [26]. Upon review of their electron probe microanalysis, they found consistent homogeneity ranges between 1300-1800°C and not line compounds as suggested by Okamoto [26], Figure 2-1(a). However, their work is not conclusive on the low temperature metastable ζ -Hf₄N₃ region. Gusve *et. al.* [72] has shown that similar M₄C₃ compounds can exhibit a modest sub-stoichiometry range. Coupling this prior work and this experimental lattice parameter value

observed in this work, it is likely that these metal-rich nitrides are not necessarily line compounds at elevated temperatures.

Conclusion

Two sets of hafnium nitride diffusion couples were processed by hot-isostatic pressing and their resulting microstructure and phase orientation were identified. Distinct regions were found in the diffusion couples. The first diffusion couple heat treated at 1900°C at 2 hrs revealed a combined phase region of ϵ -Hf₃N₂ grains with α -Hf laths, a dominant ζ -Hf₄N₃ grain region, and a mixed δ -HfN grains with ζ -Hf₄N₃ laths region between the initial α -Hf and δ -HfN diffused materials. The second diffusion couple heat treated at 1200°C for 12 hrs revealed similar regions except the mixed δ -HfN grains with ζ -Hf₄N₃ laths region was not present. Instead, the reaction zone transitioned directly from the initial δ -HfN to a mixed ϵ -Hf₃N₂ and ζ -Hf₄N₃ region. It was shown that the rhombohedral ζ -Hf₄N₃ phase, like other M₄X₃ UHTCs, formed through elemental migration along close-packed planes from FCC structures. Lattice parameter calculations from the high temperature diffusion couple verified homogeneity ranges of ϵ -Hf₃N₂ and ζ -Hf₄N₃.

CHAPTER 3

Oxidation Behavior of Vacuum Plasma Sprayed Hafnium-Tantalum Nitrides

Bradford C. Schulz¹, Daniel Butts², and Gregory B. Thompson^{1,#}

¹ Department of Metallurgical & Materials Engineering,
The University of Alabama
301 7th Avenue, 116 Houser Hall
Tuscaloosa, AL 35487-0202 (United States of America)
(205) 348-1589

² Plasma Processes, Inc.
4914 Moores Mill Road
Huntsville, Alabama 35811 (United States of America)
(256) 851-7653

Contact author: gthompson@eng.ua.edu

Abstract

A series of $(\text{HfN})_{1-x}(\text{TaN})_x$, where X is the starting 0.0, 18.8, 28.1, and 46.7 at.%, ultra-high temperature nitrides have been fabricated with the vacuum plasma spray process. The resulting nitrides had significant nitrogen content loss. This loss of nitrogen was used to explain the formation of metal-rich nitrides. The nitrides with above compositions underwent two oxidation experiments between 400-1600°C. The low porosity led to minimized boundary-controlled oxidation leaving diffusion as the primary oxidation mechanism. The resulting oxide scales were characterized by X-ray diffraction and electron diffraction. It was found that the addition of tantalum nitrides to the hafnium mixture in general resulted in an increase in mass change. However, the 18.8 at.% specimen deviated from norm and had the lowest mass change and grew a black scale. This black scale contained rhombohedral $\epsilon\text{-Hf}_3\text{N}_2$ and $\zeta\text{-Hf}_4\text{N}_3$ phases with elongated *c*-lattice parameters and STEM analysis showed oxygen diffusion into these structures. This black oxy-nitride scale acted as a passivation layer minimizing oxygen diffusion through close-packed crystal lattices.

Keywords

Vacuum plasma spray, oxidation, ultra high temperature ceramics

Introduction

Ultra high temperature ceramics (UHTC) comprise a class of materials characterized [1-2,62] by high melting points, chemical inertness, high hardness [18,22,36,63], and moderate oxidation resistance [4,10-15,19,35,53]. These ceramics typically comprise either group IV or V metals bonded with boron, carbon, or nitrogen. Depending upon the M:X ratio, where M is the metal species and X is the interstitial light element (boron, carbon, or nitrogen), various metal-rich M_6X_5 , M_4X_3 , M_3X_2 , and/or M_2X compounds can be stabilized. Depending on the phase and volume fraction of phases, the properties of UHTCs can be engineered to achieve a specific performance metric. In this work, the oxidation behavior in hafnium nitrides with various micro-alloying amounts of tantalum has been investigated. The addition of tantalum to the mono-hafnium nitride species has been reported to increase the melting temperature from 3300 to 3380°C [20,25-26,38,73]. An increase in melting temperature is beneficial to design of many applications [1,39,74-75] but at higher temperatures, oxidation becomes problematic. To date, there have been limited studies addressing how tantalum addition may alter the oxidation behavior of the hafnium nitrides. This lack of interest is likely associated that tantalum's readily oxidizes as compared to many of the metal species in UHTCs [50].

Oxidation in ceramics commonly occurs by matrix diffusion-controlled [6,10-12,53] and/or boundary-controlled processes [6,9,34-35]. In diffusion-controlled conditions, the movement of oxygen or metal species through the specimen is limited by the rate of oxidation through the diffusion layer. In a boundary-controlled process, cracking within the microstructure provides fast-track pathways for the oxygen to penetrate deeper into the material and accelerate oxidation. The hafnium nitrides have been reported to exhibit both matrix-diffusion and boundary-controlled oxidation mechanisms. During this oxidation process, an oxide scale can form. The low plasticity of the oxide scale prevents the relaxation of stresses during thermal expansion [9] which can lead to cracking within the ceramic matrix and de-cohesion of the scale spalling [6]. Hence tailoring of phases and compositions that can lead to the formation of an adherent protective oxide scale is ideal [9].

Hafnium oxide has three polymorphs which are the following: (a) monoclinic α -HfO₂ ($P2_1/c$), which forms below 1743°C (b) tetragonal β -HfO₂ ($P4_2/nmc$) that forms above 1743°C, and cubic δ -HfO₂ ($Fm\bar{3}m$) which is stabilize above 2200°C until the melting point [48,76]. If the oxide scale forms on the nitride matrix and/or goes through a series of temperatures where one of

these phase transitions occurs, the volumetric change will generate stress states that can result in the loss of adhesion. Desmison-Brut and Montintin [9] have reported that oxidation in hafnium nitride was retarded between 800 and 1000°C because of a possible intermediate oxy-nitride phase that had similar kinetic behavior as the monoclinic α -HfO₂. They suggested that the oxy-nitride phase appeared to improve the adhesion of the scale on the nitride.

This research investigated hafnium nitride and tantalum nitride combined powders processed by the top-down vacuum plasma spray method and analyzed the phase content relationship with oxidation behavior.

Experimental

Materials and methods

Four specimens of (HfN)_{1-x}(TaN)_x, where X is based on the starting blended powder compositions of 0.0, 18.8, 28.1, and 46.7 at.%, were fabricated by vacuum plasma spraying (VPS). The specimens are referenced based on the ratio of the starting blend powders. Post-spraying, the material was chemically analyzed by LECO to determine any compositional changes that could occur during the VPS process. VPS flows powders under a plasma torch where they are melted and deposited as a rapidly solidified microstructure on a substrate surface, which for these materials was graphite mandrel. Under the plasma flame, and in a vacuum condition, the liquidized powders can change composition because of vapor pressure differences between the powders' constituent species. The starting blend powders, δ -HfN and δ -TaN, were sieved with a 325 mesh to achieve powder sizes less than 45 microns. A custom-constructed VPS stainless steel chamber was evacuated to 10 Pa using mechanical pumps whereupon it was backfilled with argon to a pressure of 26.6 kPa [77]. A volume mixture of 70:1 Ar:H₂ served as the plasma gas for the feedstock powder through the VPS tungsten cathode plasma gun operated at a processing power of 33 kW. The mixture of these plasma gases has been shown to increase the processing temperature and lower porosity in the deposited material [77-78]. The as-sprayed material was deposited to an approximate thickness of 20 mm. Post-VPS fabrication, the nitride material was mechanically sectioned into 250 x 200 x 20 mm test specimens for the characterization and oxidation studies.

Specimen Characterization

The characterization of the nitrides consisted of optical and electron beam imaging as well as electron and X-ray diffraction analysis for the pre-oxidation and post-oxidation specimens. A FEI F20 Tecnai (scanning) transmission electron microscope (S-TEM), operated at 200 keV provided High Angle Annular Dark Field (HAADF) micrographs. HAADF provides atomic number or Z-contrast imaging, where higher Z-elements are brighter or scatter more strongly in this detection mode [79]. The TEM specimen was prepared using a FEI Quanta 3D Dual Beam focus ion beam (FIB) microscope milling procedure which allowed for site specific extraction and thinning [31-32]. Scanning electron microscopy (SEM) imaging of the initial powders, pre-oxidation and post-oxidation was performed using a JOEL 7000 SEM at 20 keV. This instrument also was equipped with the Oxford Instruments Electron Backscattered Diffraction (EBSD) platform which provided phase identification within the microstructure images. Chemical analysis was performed using Electron Dispersive Spectroscopy in the SEM. The SEM specimens were mounted and mechanically polished using a 3 μm diamond paste with a further polish for 24 hours in aqueous 0.05 μm silica slurry using a Vibromet [31-32].

The phases' content was identified by X-ray diffraction (XRD) using a Bruker D8 Discovery General Area Diffraction Detector System (GADDS) operated with Cu- K_{α} radiation as the source at a setting of 45 keV and 40 mA. The collected peaks were compared with the phase data found in the International Centre for Diffraction Data (ICDD) given in references [80-99]. Prior to XRD analysis, the pre-oxidation specimens were crushed and ground using a mortar and pestle which ensured a random texture and sufficiently large sampling volume from the powder particulates. Post-oxidation XRD analysis was conducted directly on the scale formed on surface (the scale was not removed and crushed as a powder due to the lack of materials). An XRD line scan was also conducted with a 0.8 mm spot size with 0.01 mm steps for dwell times of 180 seconds, Appendix A. The reported accuracy of significant figures is based on the 2- θ step.

Specimen Oxidation

Two sets of oxidation experiments were conducted on the nitride specimens, denoted at oxidation treatment I and II. In both experiments, the pre- and post-oxidation specimens' masses were measured. The nitride specimens were placed in silica boats and heated under atmospheric conditions in a 99.5% alumina tube inserted in a Sentro Tech Corp 1700 2.5-6 high temperature

tube furnace with MoSi₂ heating elements. In oxidation treatment I, the specimens were heated from room temperature to either 700, 1200, or 1700°C. The 700 and 1200°C maximum temperature experiments consisted of heating to 200°C at a 20°C/min where it was held for 10 min, then ramped up to the targeted maximum set point at a rate of 10°C/min where it was held for an hour and then allowed to cool to room temperature which took approximately 2 hours. The 1700°C maximum temperature followed the specimen process except that at 1200°C it was held for 10 minutes and then continued to ramp to 1700°C at the same rate where it was held for one hour and allowed to cool afterwards, which took approximately 3 hours. This heating procedure was the furnaces manufacturer's recommended heating procedure to achieve the higher temperature set points.

Based on the results of the first oxidation treatment, the oxidation treatment II was only conducted for the (HfN)_{1-x}(TaN)_x 18.8 at.% nitride specimen; this specimen showed promising oxidation behavior as will be discussed below. The 18.8 at.% nitride was mechanically cut into 3 x 3 x 3 mm cubes and polished with 120 grit SiC paper on all six surfaces. After polishing, the cubes were cleaned in ethanol for 8 hours followed by 8 hours of ultra-sonic water cleaning where it was then air dried for 8 hours. The furnace brought to the set point temperature of 400, 650, 750, 800, 850, 950, 1200, and 1600°C and immediately inserted and then removed after 60 minute and allowed to air quench (rather than the slow furnace cool done in the first set of oxidation experiments).

Results

Pre-Oxidation

The average initial powder sizes were between 6-7 μm for both δ-HfN and δ-TaN powders, Figure 3-1. The specimens' intrinsic, as-sprayed microstructure porosity and nitrogen content post-VPS spraying is tabulated in Table 3-1. The porosity was measured using the Delesse Principle which compares the surface area fraction of the total pore count divided by the total surface area of the image [57]. The nitrogen measurements were provided by LECO.

The XRD scans for the four pre-oxidized nitride specimens confirmed the phases of α-Hf, β-Ta, δ-HfN, δ-TaN, ε-Hf₃N₂, ζ-Hf₄N₃, and γ-Ta₂N, Figure 3-2. The identification of the metal and metal-rich nitrides confirms the loss of nitrogen, as noted in the LECO measurements. The

metal-rich nitride phases (ϵ -Hf₃N₂, ζ -Hf₄N₃, and γ -Ta₂N) were prevalent in the 18.8 at.% specimen.

Oxidation Treatment I

For the first oxidation series, an increase in maximum temperature led to an increase in mass change, Table 3-2. Pre- and post-oxidation optical images of the specimens are shown in Figure 3-3. Comparing Table 3-2 and Figure 3-3, as the mass change increased, there was a corresponding presence of an oxide scale, evident by the change in color of the specimens and prevalent powder (which is the delaminated scale) around the bulk of the specimen. The only exception with respect to the to the spalling of the scale powder was the 18.8 at.% specimen, which had a dark-color scale as compared to the white or brown color of the other scales, Figure 3-3. Interestingly the 18.8 at.% specimen also had the highest porosity content, Table 3-1. The oxide scales for all the post-oxidized specimens is plotted in Figure 3-4(a-d). Those specimens with dominant white-colored scale/powder had strong α -HfO₂ peaks located at 2θ 28.31° and 31.70°. The specimens that developed a brown color scale, notably the 28.1 and 46.7 at.% specimens heated to 1700°C, have a high intensity α -Ta₂O₅ peak at 2θ 35.52°. Similar to hafnia, tantalum oxides have different polymorphs with temperature which are the orthorhombic L-Ta₂O₅ (*Pmm2*) (below 700°C) [51], triclinic β -Ta₂O₅ (*P $\bar{1}$*) (stable between 700°C and 1320°C), and monoclinic α -Ta₂O₅ (*C2/m*) (1320°C till its melting temperature at 1872°C) [52]. The 18.8 at.% specimen, which had the dark-colored scale, Figure 3-3, retained strong diffraction from the α -Hf, ϵ -Hf₃N₂, ζ -Hf₄N₃, δ -HfN, and ϵ -Ta₂N phases (pre-oxidation phases) at the 700 and 1200°C temperatures. Only at 1700°C, did the presence of α -HfO₂, L-Ta₂O₅, and Hf₇O₈N₄ (along with the prior phases) become noticeable, Figure 3-4(b). Note that the 18.8 at.% specimen is the only specimen that was indexed to have an oxy-nitride phase. These differences are easily identified by considering the clustering of nitride peaks around 35° 2θ compared to the clustering of oxide peaks around 27° 2θ between all the scans in Figure 3-4.

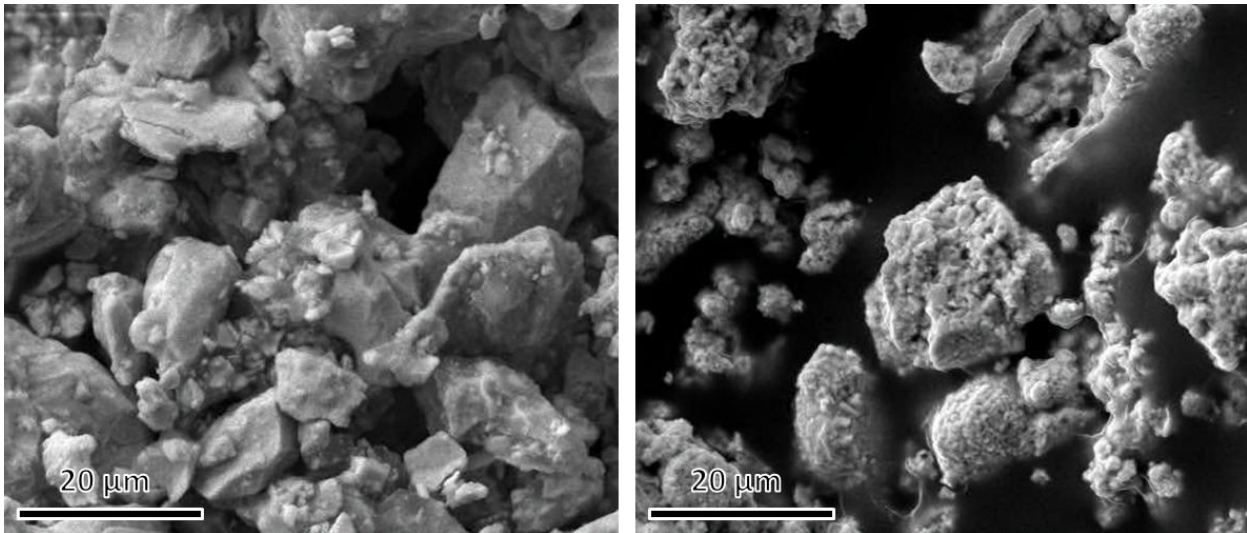


Figure 3-1: SEM imaging of pre-mixed nitride powders (left: HfN, right: TaN).

Specimen Chemistry (HfN) _{1-x} (TaN) _x	Post-Processed	
	Porosity %	Nitrogen (at.%)
0.0 at.%	2.78	21.16
18.8 at.%	5.58	24.04
28.1 at.%	2.52	17.80
46.7 at.%	3.67	25.70

Table 3-1: Analysis of the four (HfN)_{1-x}(TaN)_x nitrides (0.0, 18.8, 28.1, 46.7 at.%) post-VPS processed. Analysis includes the porosity % calculated with the Delesse Principle and LECO results.

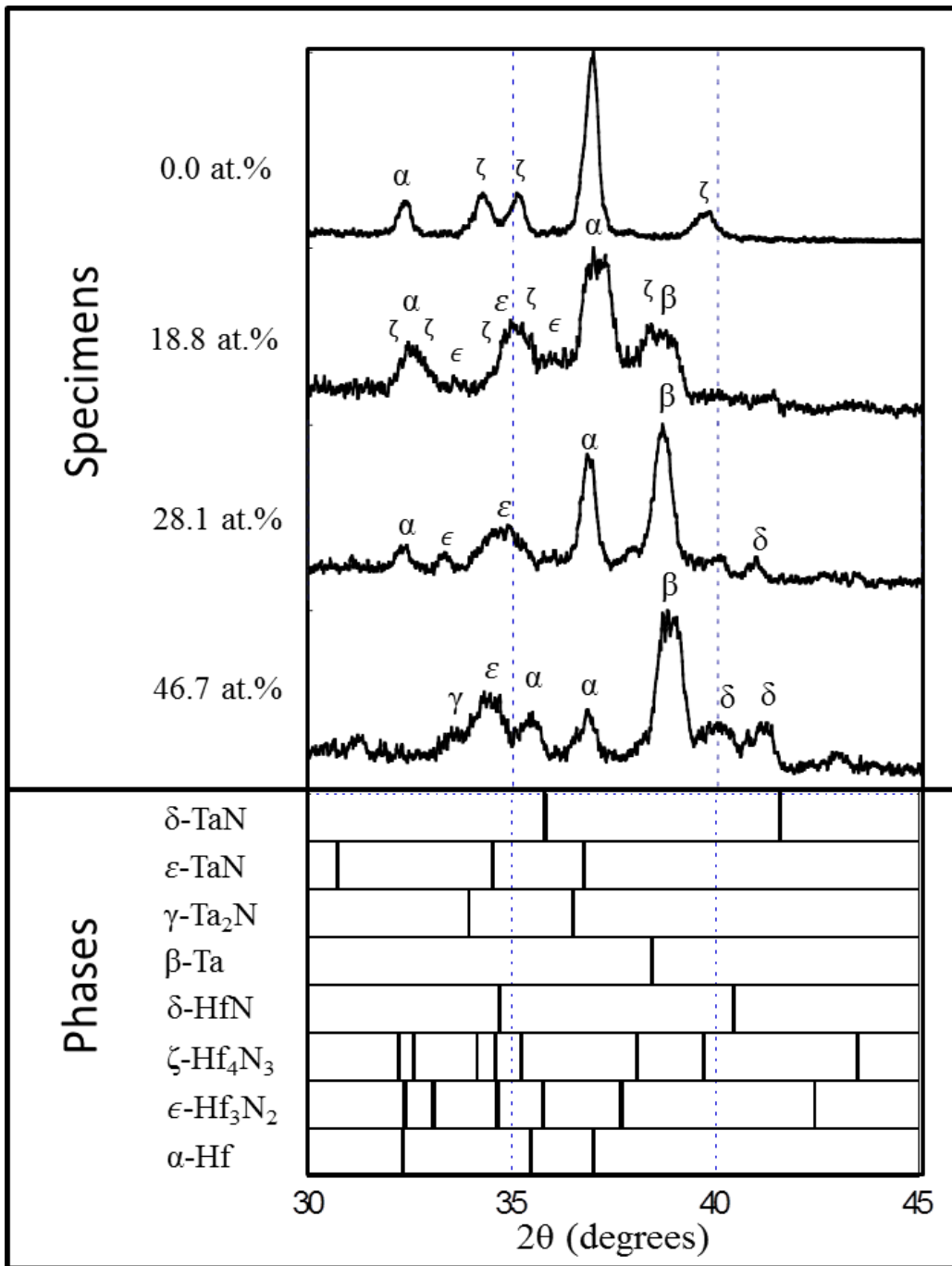


Figure 3-2: Pre-oxidation normalized XRD phase identification of the four specimens $(\text{HfN})_{1-x}(\text{TaN})_x$ where X is 0.0, 18.8, 28.1 and 46.7 wt.%. The phase peak information for the phases considered are presented below the four specimens.

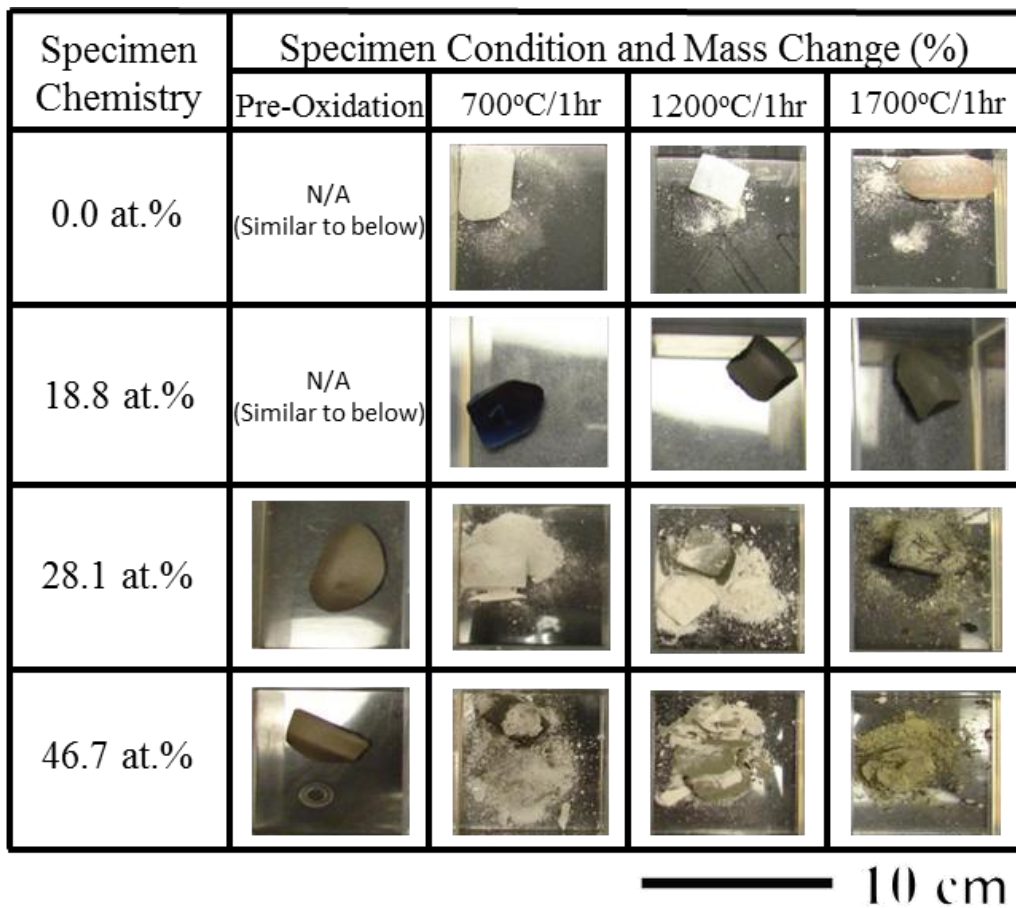


Figure 3-3: Pre- and post-oxidation images of the four specimens $(\text{HfN})_{1-x}(\text{TaN})_x$ where X is 0.0, 18.8, 28.1 and 46.7 at.%.

Specimen Chemistry $(\text{HfN})_{1-x}(\text{TaN})_x$	Post-Oxidation Mass Change %		
	700°C	1200°C	1700°C
0.0 at.%	0.37	0.75	1.61
18.8 at.%	0.04	0.02	0.10
28.1 at.%	1.67	3.34	N/A
46.7 at.%	1.35	3.25	3.61

Table 3-2: Analysis of the four $(\text{HfN})_{1-x}(\text{TaN})_x$ nitrides (0.0, 18.8, 28.1, 46.7 at.%) post-oxidation. Mass change % was measured for all four specimens for first oxidation series (700°C, 1200°C, and 1700°C).

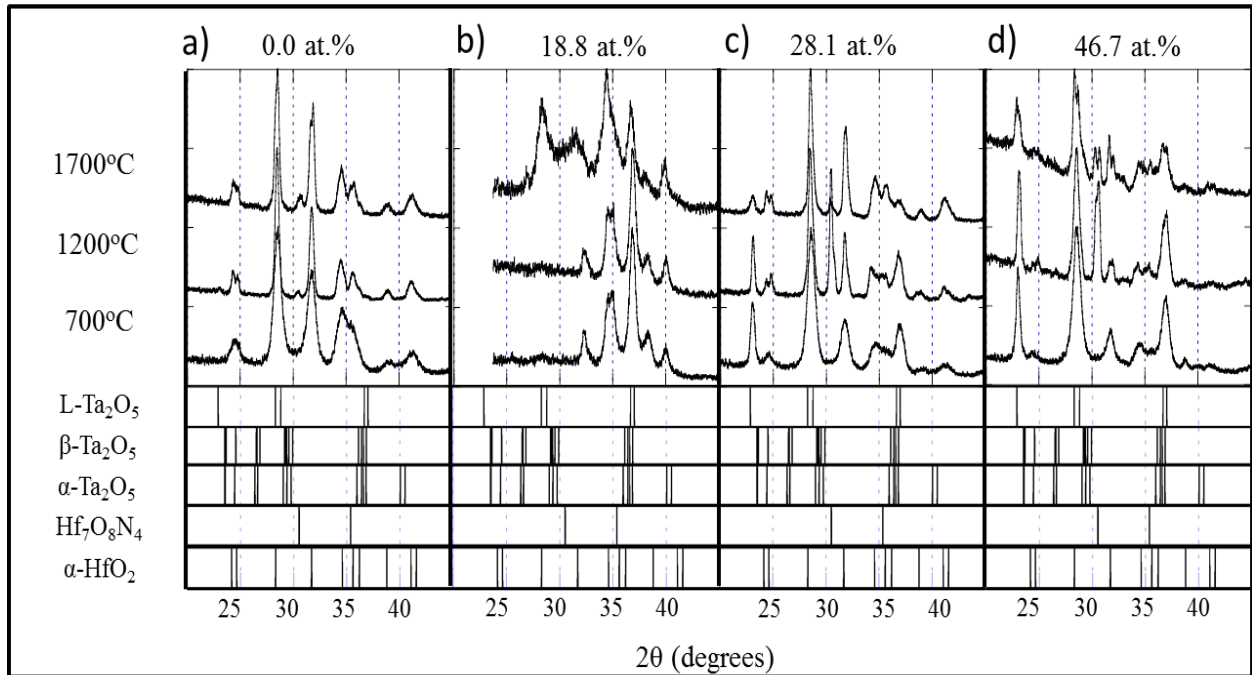


Figure 3-4: Post-oxidation normalized XRD phase identification of the oxide scale for specimen $(\text{HfN})_{1-x}(\text{TaN})_x$ where $X=0.0$ (a), 18.8 (b), 28.1 (c), and 46.7 (d) at.% for the three oxidation experiment temperatures (top). The normalized phase peak information for the main oxide phases considered are presented below the XRD data.

A line XRD scan was performed on the 18.8 at.%-1700°C specimen. Figure 3-5 is a plot of those scans as a function of distance, two-theta, and intensity. Since the X-ray probe is larger than the scale thickness, relative changes (rather than absolute position values) can be inferred from the intensity and peak position shifts of the scan across the surface of the specimen. The following crystallographic data was used to identify the phases and calculate lattice parameters over the scanned region: the $[10\bar{1}1]$ peak for α -Hf [65], the $[10\bar{1}4]$ peak for ϵ -Hf₃N₂ [27], the $[10\bar{1}7]$ peak for ζ -Hf₄N₃ [27], and the $[200]$ peak for δ -HfN [66]. An additional $[hk0]$ peak, $[11\bar{2}0]$, was required to determine the second lattice parameter associated with either the hexagonal and rhombohedral phases [67]. The calculated lattice parameters and their shifts from bulk to oxide scale are tabulated in Table 3-3.

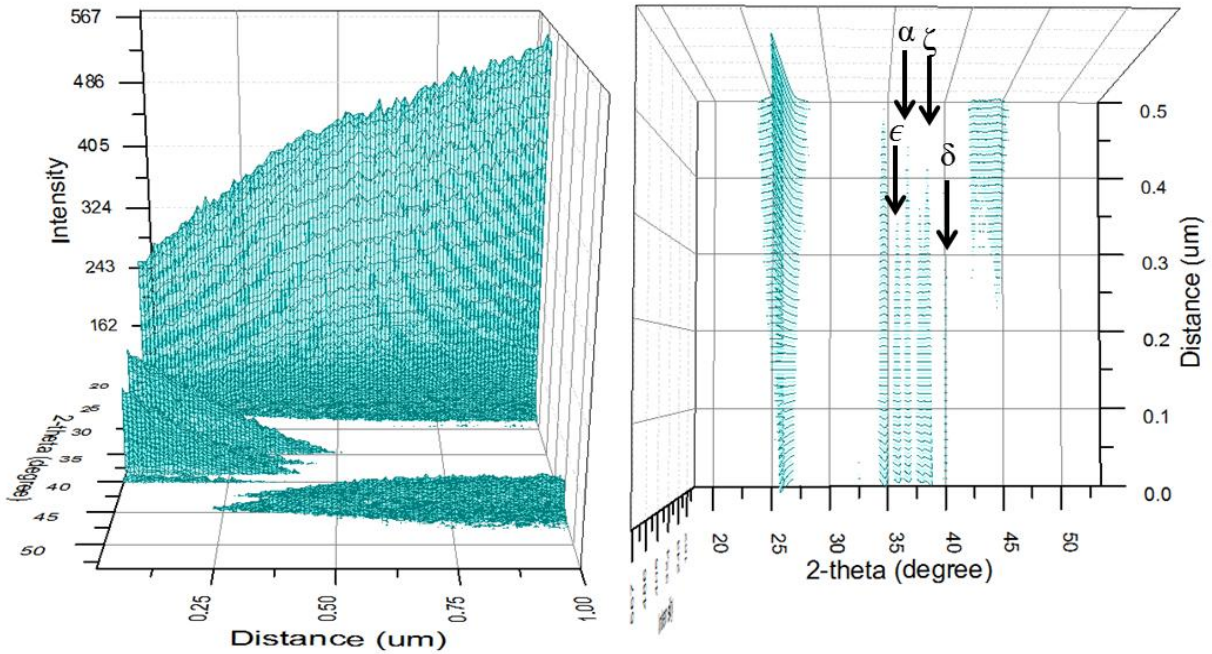


Figure 3-5: XRD line scan of the $(\text{HfN})_{1-x}(\text{TaN})_x$ 18.8 at.% 1700°C oxidized specimen with a step size of 0.01 mm. (Left) Entire image with x- 2θ (25° - 50°), y-distance (0.00-1.00 mm), and z-intensity. (Right) Line scan data view from x-y plane with peaks utilized for phase identification marked.

	0.00 mm	0.25 mm	0.38 mm	0.50 mm	Prior
Chemical Formula			Hf		
Crystal System			Hexagonal		
Space Group			$P63/mmc$ (194)		
a (nm)	0.3196	0.3196	0.3196	0.3196	0.320
c (nm)	0.5194	0.5194	0.5218	0.5228	0.506
Chemical Formula			$\text{HfN}_{0.67}$		
Crystal System			Rhombohedral		
Space Group			$R\bar{3}m$ (166)		
a (nm)	0.3206	0.3206	0.3206	0.3200	0.321
c (nm)	2.322	2.322	2.446	2.467	2.326
Chemical Formula			$\text{HfN}_{0.75}$		
Crystal System			Rhombohedral		
Space Group			$R\bar{3}m$ (166)		
a (nm)	0.3214	0.3214	0.3214	0.3214	0.321
c (nm)	3.022	3.022	3.044	3.075	3.112
Chemical Formula			HfN		
Crystal System			Cubic		
Space Group			$Fm\bar{3}m$ (225)		
a (nm)	0.4506	0.4506	0.4509	0.4512	0.452

Table 3-3: Table 3-3: Lattice parameters (left) based on peak shift from the 18.8 at.% 1700°C oxidized specimen XRD line scan compared with prior literature (right: (McMurdie^[65], Rudy^[27], and Fiala^[66]).

Oxidation Treatment II

The $(\text{HfN})_{1-x}(\text{TaN})_x$ $X=18.8$ at.% composition was selected for further oxidation experiments based on the promising findings in the initial oxidation experiments. In general, an increase in temperature, which spanned 400 to 1600°C, lead to an increase in mass change, tabulated in Table 3-4, with significant changes at 1200 and 1600°C. Since the scale adhered relatively well to this specimen compared to the others (which had significant spalling evident by the powder presence), the scale thicknesses with temperature could be measured. The scale thickness was determined by comparing both the SEM cross sectional image overlaid with an EDS line profile, Figure 3-6(a). Figure 3-6(b) is the plot of scale growth as a function of temperature. As the temperature increased, an observable intermediate layer existed between the bulk nitride specimen and the oxide scale. This is evident by the dark contrast beside the oxide scale but prior to the bulk matrix in the SEM micrograph of Figure 3-6(a). This region is labeled as the “intermediate” layer. In addition a drop in oxygen content is correlated with this intermediate layer. In the plot of Figure 3-6(b), the oxide scale length increases with temperature while the intermediate layer remains relatively constant. The error bars are one standard deviation from the average for three separate scans from three different regions of the specimen for that particular temperature.

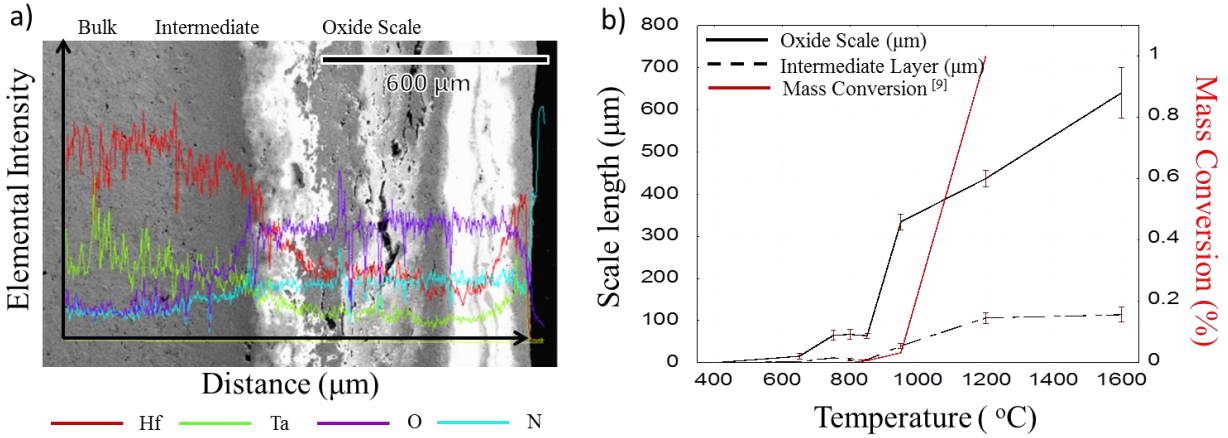


Figure 3-6: (a) Example of SEM EDS line scan of oxidation II treatment scale thickness. This specific scan is one of three from the 1200°C 60 min specimen. The bulk of the specimen on left, intermediate layer in middle, and oxide scale on right. (b) Plot of oxide scale and intermediate layer based on SEM EDS line scans. The solid line represents the oxide scale measurements, dashed line for the intermediate scale, and the error bars are marked as red in the y-axis. An additional plot of normalized mass change vs. temperature is also plotted in red which shows the similar findings from Desmaison-Brut and Montintin ^[9].

Temperature (C)	Mass Change (%)
400	0.36
650	1.42
750	1.60
800	2.87
850	1.32
950	1.39
1200	4.04
1600	9.40

Table 3-4: Mass change % for the (HfN)_{1-x}(TaN)_x X=18.8 at.% specimen post-oxidation II treatment.

Discussion

The post-VPS process $(\text{HfN})_{1-x}(\text{TaN})_x$ specimens' LECO combustion analysis, Table 3-1, indicated that the nitrogen content was depleted from the initial blend mixture. In the case of Hf-N, nitrogen loss stabilizes the rhombohedral $\zeta\text{-Hf}_4\text{N}_3$ and $\epsilon\text{-Hf}_3\text{N}_2$ whereas in Ta-N, a hexagonal $\gamma\text{-Ta}_2\text{N}$ phase precipitates with nitrogen depletion. In addition, all the species showed some fraction of elemental hafnium and tantalum, when it was added. As consequence of this multiphase microstructure is a complex oxidation behavior.

The control 0.0 at.% specimen had moderate mass changes compared to the 28.1 and 46.7 at.% specimens. The XRD scale of this specimen was indexed as $\alpha\text{-HfO}_2$, indicating that the white scale/powder was hafnia. In contrast, the 28.1 and 46.7 at.% had a strong primary $\beta\text{-Ta}$ peak in the post-sprayed condition. Since tantalum readily oxidizes faster than hafnium, and was prevalent in the material, this explains the observed poorer oxidation resistance. The XRD scans of these scales were hafnia and $\alpha\text{-Ta}_2\text{O}_5$, with the latter being the most intense indicative that the tantalum was the primary oxide. The change in oxide scale resulted in a change in color of the scale from white to brown, Figure 3-3.

The specimen with the lowest mass change, 18.8 at.%, contained a lower $\beta\text{-Ta}$ peak compared to $\alpha\text{-Hf}$ and a balance of the close-packed like structures of $\epsilon\text{-Hf}_3\text{N}_2$, $\zeta\text{-Hf}_4\text{N}_3$ and $\gamma\text{-Ta}_2\text{N}$ phases, Figure 3-2. Upon oxidation treatments at 700 and 1200°C, a discernible oxide was not detected, Figure 3-4. In contrast, a strong oxy-nitride peak, $\text{Hf}_7\text{O}_8\text{N}_4$ was indexed near 35° 2 θ . The chemical presence of such a phase is supported by the EDS line scan in Figure 3-6 too. Though this particular peak can be identified in the other specimens, its relative peak intensity is not as large as compared to the 18.8 at% specimen. Though an $\alpha\text{-HfO}_2$ peak can also exist near 35°, the $\alpha\text{-HfO}_2$ peak near 27° 2 θ provides a clearer indication of the scale's presence with no peak overlap. In the 0.0, 28.1, and 46.7 at.% specimens, this 27° 2 θ $\alpha\text{-HfO}_2$ peak is clearly evident at each temperature. In contrast, this 27° 2 θ peak is not observed for the 700 and 1200°C scans for 18.8 at.%, This indicates that this particular composition did not readily oxidize. This statement is supported by the low mass change, Table 3-2. At 1700°C, the $\alpha\text{-HfO}_2$ 27° 2 θ peak is evident and the onset of a white scale powder is present on this specimen, Figure 3-3, and subtle changes in mass measured. This suggests that temperatures in excess of 1200°C, for this particular composition, results in the clear onset of oxidation.

The $\text{Hf}_7\text{O}_8\text{N}_4$ phase has a rhombohedral symmetry [94], similar to the rhombohedral $\zeta\text{-Hf}_4\text{N}_3$ and $\epsilon\text{-Hf}_3\text{N}_2$ based structures [27], which may account for the ability to form this intermediate phase. An EDS line profile across the hafnium-rich nitride phases in the scale of the 18.8 at.%-1700°C specimen showed increases in oxygen levels, Figure 3-7(a-b), suggestive that these phases do act as oxygen getters and provide a heterogeneous nucleation sites for forming the oxy-nitride.

Since a gradation of oxygen into these rhombohedral structures would occur as oxygen diffuses into the material, that lattice parameter of the rhombohedral hafnium-rich nitride phases would shift. The $\zeta\text{-Hf}_4\text{N}_3$ rhombohedral structure has $\frac{1}{4}$ and the $\epsilon\text{-Hf}_3\text{N}_2$ rhombohedral structure has $\frac{1}{3}$ of its light element interstitial sites vacant. Assuming that the oxygen interacts with these vacant and nitrogen interstitial sites, the composition of these ‘transitional’ phases would be $\zeta\text{-Hf}_4\text{O}_x\text{N}_3$ and $\epsilon\text{-Hf}_3\text{O}_x\text{N}_2$ where oxygen substitutes in for interstitial vacancies or nitrogen. These ‘transitional’ phases are also assuming that the crystallography remains the same. When they are coupled with the lattice parameters determined from the peaks shifts from the XRD line scan of Figure 3-5 tabulated in Table 3-3, these ‘transitional’ phases were successfully identified in the EBSD phase map of Figure 3-8(a-b) as distinct phases. This phase map has now identified the metal-nitride phases, Figure 3-8(a), and the different oxy-nitride phases, Figure 3-8(b). Also note the high vol.% of the $\zeta\text{-Hf}_4\text{O}_x\text{N}_3$ and $\epsilon\text{-Hf}_3\text{O}_x\text{N}_2$ phases tabulated in Table 3-5. To the authors’ knowledge, these proposed intermediate oxy-nitride phases of $\text{Hf}_4\text{O}_x\text{N}_3$ and $\text{Hf}_3\text{O}_x\text{N}_2$ have not been previously reported but exist in the oxide scale and likely act as a phase transformation pathway to forming the rhombohedral $\text{Hf}_7\text{O}_8\text{N}_4$ or $\alpha\text{-HfO}_2$ phases. By filling these interstitial vacancies, the oxy-nitride layer provides a barrier for oxygen diffusion. If further oxygen is required to pass through this phase, it will either require substitutional site exchange and/or a phase transformation to another symmetry. Future work is underway to determine the stability of these intermediate phases through density functional theory.

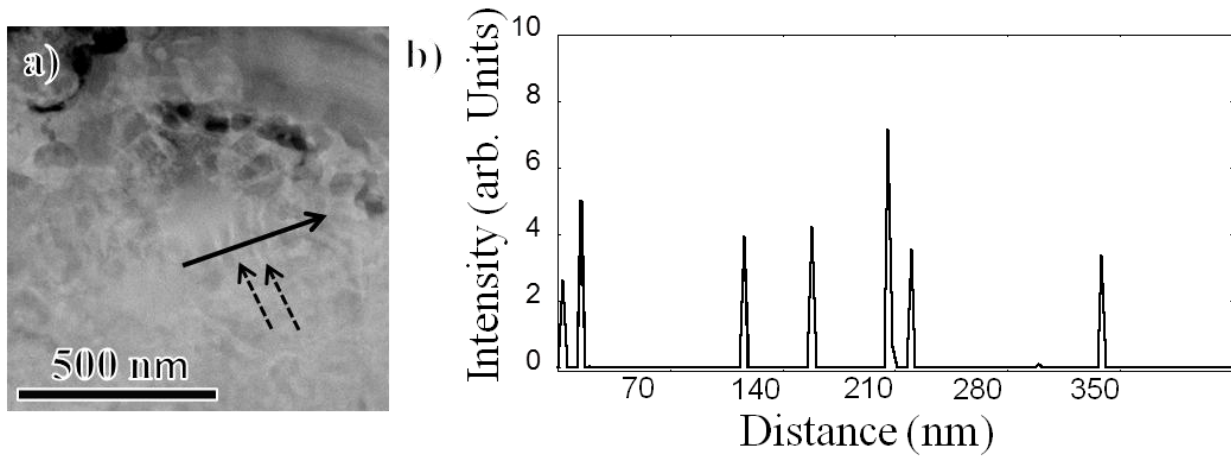


Figure 3-7: The $(\text{HfN})_{1-x}(\text{TaN})_x$ $X=18.8$ at.% specimen post-oxidation I treatment at 1700°C oxidation. a) HAADF STEM image of lath-like microstructure with marked path of STEM EDS line profile. The brighter contrast in these laths (dash arrows) is due to hafnium enrichment found in the (b) STEM EDS line profile. (b) EDS line profile shows oxygen intensity peak data.

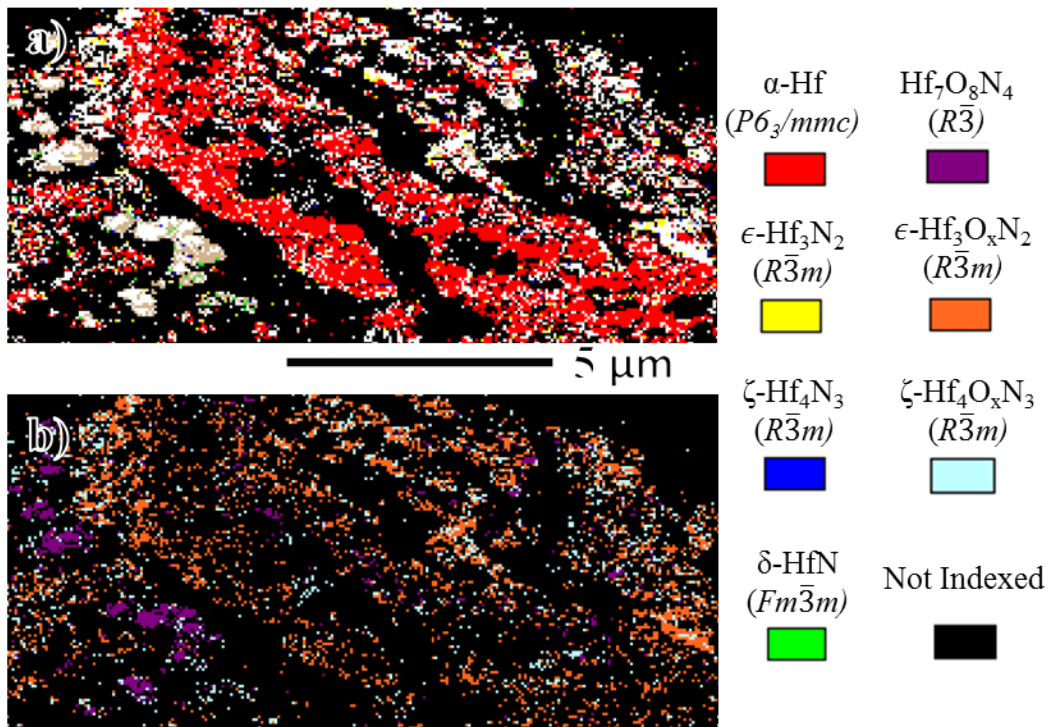


Figure 3-8: The EBSD for (HfN)_{1-x}(Ta₂N)_x X=18.8 at.% specimen post-oxidation I treatment at 1700°C oxidation. a) Image of four hafnium phases. d) Image of the phases with oxygen.

Phase	Vol. %
α -Hf	19.4
ϵ -Hf ₃ N ₂	1.2
ζ -Hf ₄ N ₃	0.2
δ -HfN	0.2
β -Ta	1.1
γ -Ta ₂ N	0.2
δ -TaN	2.6
ϵ -TaN	0.2
Hf ₇ O ₈ N ₄	2.4
ϵ -Hf ₃ ON ₂	9.6
ζ -Hf ₄ ON ₃	4.6

Table 3-5: Phase vol.% identified from the EBSD for (HfN)_{1-x}(Ta₂N)_x X=18.8 at.% specimen post-oxidation I treatment at 1700°C.

Though these metal-rich nitrogen phases existed in all the systems, the addition of 18.8 at.% tantalum appears to assist in stabilizing a larger fraction of these phases which are believed to improve the oxidation resistance by providing a pathway to nucleate an oxy-nitride diffusion barrier. Though the VPS process can be considered highly dynamic and lead to non-equilibrium phases; phase diagrams can still provide useful insights into phase stability [77]. The approximate location for each post-VPS sprayed specimen, using the LECO nitrogen results, is plotted in Figure 3-9 [100]. Clearly, the experimental presence of a variety of phases, Figure 3-2, than those allowed in the phase diagram, Figure 3-9, indicates that the system was not in equilibrium. Regardless, one can glean how phase fractions may be driven to achieve equilibrium. As the tantalum amount increased, (1) to (4) in Figure 3-9, the occurrence of these rhombohedral based hafnium-rich nitride phases increases too. The volume fraction of these phases can be inferred by the XRD intensity increases relative to α -Hf seen between the 0.0 and 18.8 at.% specimens. Though these hafnium rich nitrides existed at higher tantalum additions, the higher fraction for β -Ta, with its poor oxidation properties, dominated the oxidation. In addition, the 18.8 at.% specimen also had the highest porosity which one could assume would provide the worst oxidation resistance because of the cracks and open volume pathways to allow boundary oxidation. In contrast, the formation of the intermediate oxy-nitride scale appears to be more dominating in regulating the oxidation behavior as compared to the other specimens.

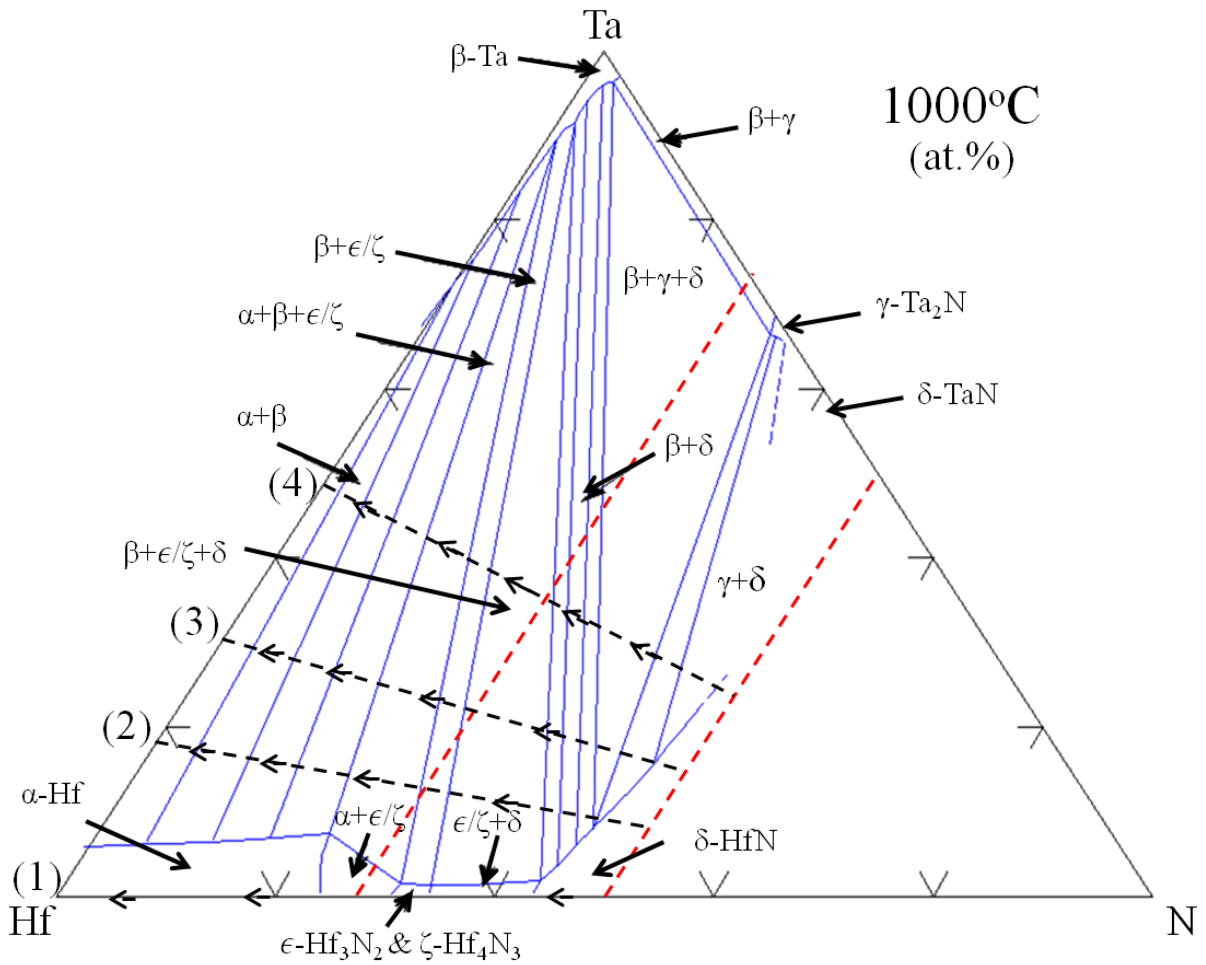


Figure 3-9: Ternary Hf-Ta-N phase diagram at 1000°C based on initial Rudy^[38] findings. The ϵ -Hf₂N phase in the original report [38] has been replaced by ϵ -Hf₃N₂ & ζ -Hf₄N₃^[27]. In this diagram, dashed lines (1-4) estimate the nitrogen loss path for (1) 0.0, (2) 18.8, (3) 28.1, and (4) 46.7 at.% (Ta₂N) with arrows indicating nitrogen loss direction. The red dashed lines are approximated for 25 and 50 at.% nitrogen.

An additional set of oxidation experiments, treatment II, were designed to determine the stability of the oxy-nitride scale. Based on the mass change, Table 3-4, the 18.8 at.% specimen followed similar trends as prior studies of HfN with no tantalum additions [9]. In their report and this current study, there was little to no oxidation below 650°C, a minimal increase between 650 and 950°C, and a significant change above 950°C. Desmaison-Brut and Montintin [9] suggested that an intermediate layer formed in HfN between 600-1000°C and suggested a possible oxy-nitride layer as a barrier to oxidation but provided no microstructural characterization to verify its presence. Based on the characterization of this work, an oxy-nitride layer does form and supports this prior suggestion. Unlike the prior work [9], where oxidation exponentially increased above 1000°C, this work shows a slower linear rate of increase. This may be contributed to the increased fraction of metal-rich nitride layers which are stabilized by the tantalum additions and provide a pathway to more easily form an oxy-nitride intermediate boundary compared to one in a mono-nitride starting matrix. Collectively, these metal-rich nitride phases appear to be advantageous by acting as a passivation layer in minimizing oxygen diffusion through the close-packed like crystal lattices.

Conclusion

A series of $(\text{HfN})_{1-x}(\text{Ta}_x\text{N})_x$ compositionally mixed powders where $X= 0.0, 18.8, 28.1,$ and 46.7 at.% were processed with a vacuum plasma spray. The resulting nitrides had significant nitrogen content loss. This nitrogen loss is known to occur for the non-equilibrium parameters during VPS processing. This loss of nitrogen and the use of a ternary phase diagram were used to explain the presence of metal-rich phases. With sufficient nitrogen loss the formation of elemental α -Hf and β -Ta formed. When nitride compositions underwent two oxidation experiments between 400-1600°C it was found that this presence of β -Ta readily formed α -Ta₂O₅. The dominant oxide scale was found to be a white powder α -HfO₂. The specimen with the lowest mass change, 18.8 at.%, contained a lower β -Ta peak compared to α -Hf and a balance of the close-packed like structures of ϵ -Hf₃N₂, ζ -Hf₄N₃ and γ -Ta₂N phases. This composition developed a dark intermediate oxy-nitride phase between the oxide scale and bulk. XRD data identified three oxy-nitrides; the Hf₇O₈N₄ and the rhombohedral Hf-N based ζ -Hf₄O_xN₃ and ϵ -Hf₃O_xN₂ phases. STEM EDS line profiles suggested that the rhombohedral Hf-N phases acted as

oxygen getters and provide heterogeneous nucleation sites for forming the oxy-nitride. These phases were derived from the inherent interstitial vacancy of the ζ -Hf₄N₃ and ϵ -Hf₃N₂ phases that became filled with oxygen. It is believed that these metal-rich nitride phases are advantageous to oxidation resistance by acting as a passivation layer in minimizing oxygen diffusion through the close-packed like crystal lattices.

CHAPTER 4

Influence of an Oxy-nitride Scale on the Oxidation Characteristic in Hf(Ta)N

Bradford C. Schulz¹, Daniel Butts², and Gregory B. Thompson^{1,#}

¹ Department of Metallurgical & Materials Engineering,
The University of Alabama
301 7th Avenue, 116 Houser Hall
Tuscaloosa, AL 35487-0202 (United States of America)
(205) 348-1589

² Plasma Processes, Inc.
4914 Moores Mill Road
Huntsville, Alabama 35811 (United States of America)
(256) 851-7653

Contact author: gthompson@eng.ua.edu

Abstract

It was found that the increase in density for the nitrides processed with vacuum plasma spray and an additional sinter/HIP step improved oxidation resistance. The reaction of hafnium nitride conversion into hafnia was found to be affected by both boundary and diffusion mechanisms. Boundary oxidation mechanisms were significant in specimens with increased porosity and that were subjected to cracking, possibly from thermal expansion stresses. Specimens with low porosity minimized boundary oxidation. It was found that the inherent nitrogen loss from the high temperature processing led to the formation of close-packed phases. These close-packed phases aided in limiting the diffusion of oxygen through an adherent oxy-nitride intermediate layer. Growth of this oxy-nitride intermediate layer was observed to begin as low as 650°C. A decrease in oxidation diffusion through the reaction layer was explained by close-packed like rhombohedral ϵ -Hf₃N₂ laths. Not only did the high density minimize boundary oxidation but the oxy-nitride also lowered the rate of oxygen diffusion through the reaction layer.

Keywords

Vacuum plasma spray, sinter, hot-isostatic pressure, oxidation, ultra high temperature ceramics

Introduction

The group IV and V metal ceramics consist of a metal atom which is bonded to an interstitial light element, such as boron, carbon or nitrogen [2,27]. These bonds can lead to a variety of phases and properties that are dependent upon the metal-interstitial ratio. For example, the depletion of nitrogen from the group IV mono-hafnium nitride phase results in the precipitation of rhombohedral ϵ -Hf₃N₂ and ζ -Hf₄N₃ compounds. Similarly, a depletion in nitrogen from the group V mono-tantalum nitride phase facilitates the precipitation of a close-packed hexagonal γ -Ta₂N phase. By controlling the mixture of phases [20,25-26] in a microstructure, the properties, such as mechanical [18,36], electrical [23-24] and oxidation [4,10-13,35,53], can be tuned to achieve a higher performance .

A common trait to ceramics is a high melting temperature. At high temperatures, oxidation can be a significant concern in maintaining the structural and phase stability. Oxidation in ceramics commonly occurs by matrix diffusion-controlled [6,10-13,53] and/or boundary-controlled [6,9,34-35] processes. For the hafnium nitride system in the presence of oxygen, the following reaction can occur:



In diffusion-controlled conditions, the oxidation rate is limited by the movement of oxygen or metal species through this reaction layer. In a boundary-controlled process, cracking within the microstructure through the reaction layer provides fast-track pathways for the oxygen to penetrate deeper into the material and initiate the oxidation reaction. The formation of an adherent, protective oxide scale that acts as a boundary barrier which can minimize oxygen diffusion is advantageous in preserving the original ceramic microstructure.

The group IV hafnium nitrides have been reported to exhibit both diffusion-controlled and boundary-controlled oxidation mechanisms [9]. Once hafnia forms, the low plasticity of the scale prevents the relaxation of stresses during thermal expansion [9] which leads to cracking and de-cohesion of the scale, which is referred to as spalling [6]. A guideline to determine if spalling will occur is the Pilling-Bedworth ratio (R_{PB}), which is the ratio of oxide volume to matrix volume [42]. If an oxide scale will spall, the development of an intermediate or transitional oxide scales which adheres and reduces the oxidation kinetics is desirable. The development of such layers involves manipulating the phase content and compositions within the ceramic microstructure. Micro-alloying is one means of microstructure manipulation. Previous

reports have suggested that the group V ceramic close packed structures have reduced oxidation characteristics [6,10-12,53]. The authors have recently reported that micro-alloying of tantalum nitrides to hafnium nitrides can result in improved oxidation resistance [101]. This improvement was associated with the formation and stabilization of an oxy-nitride layer, originally proposed by Desmanson-Brut and Montintin [9]. In this current work, a micro-alloy composition is further studied to determine how optimizing the processing of the microstructure as well as the oxy-nitride layer can further improve the oxidation behavior.

Experimental

Materials and methods

Two sets of specimens with an initial blend of 80HfN-20TaN (wt%) were fabricated by vacuum plasma spraying (VPS). These starting blended powders were mixed from δ -HfN and δ -TaN powders sieved with a 325 mesh to select powders less than 45 μm . Since the VPS process can result in a splat-like microstructure and higher intrinsic porosity [31-32,77-78,80], two specimens were compared; one that was in the as-sprayed condition (denoted as-sprayed) and one that was sintered and hot-isostatic pressed (HIP) after spraying (denoted sintered/HIP'ed) to equilibrate and consolidate the microstructure. In prior study [101], the specimens were not sintered nor HIP'ed after spraying.

The VPS occurred in a custom-made stainless steel processing chamber that was evacuated to 10 Pa using mechanical pumps whereupon it was backfilled with argon to a pressure of 26.6 kPa [77]. A volume mixture of 70:1 Ar:H₂ served as the plasma gas for the feedstock powder through the tungsten cathode plasma gun operated at a power of 33 kW. From the plasma gun, the molten feedstock powder was sprayed onto a rotating graphite mandrel to an approximate thickness of 20 mm. Post-VPS fabrication, the graphite mandrel was mechanically ground away and the specimens had an approximate density of 96 \pm 1%. For the sintered/HIP'ed specimen, the sintering was done under an argon atmosphere in a graphite furnace heated to approximately 2000°C. After which, the specimen was can-less HIP'ed near 2000°C at 200 MPa to achieve a density of approximately 98 \pm 1%. The nitrogen composition of the post-sprayed and sintered/HIP'ed was quantified by LECO combustion analysis. These specimens had approximately the same nitrogen content as the prior study [101] which had the improved oxidation performance for a variety of tantalum nitride conditions.

Specimen Characterization

The characterization of the nitrides consisted of electron and X-ray diffraction analysis. A FEI F20 Tecnai (scanning) transmission electron microscope ((S)TEM) operated at 200 keV using a High Angle Annular Dark Field (HAADF) detector was used for imaging. The HAADF provides micrographs which give semi-quantitative imaging based on the atomic number, or Z-contrast. The technique is relatively insensitive to crystallographic orientated contrast allowing the higher atomic number regions or phases to appear brighter within the image [79]. The TEM specimens were prepared using a focus ion beam (FIB) milling technique which allowed for site specific extraction and thinning [31-32] using a FEI Quanta 3D dual electron-FIB microscope. Additional microstructure analysis was imaged using scanning electron microscopy (SEM) performed in a JOEL 7000 SEM at 20 keV. This instrument was equipped for Electron Backscattered Diffraction (EBSD) for phase and grain size analysis using the Oxford Instruments platform. Chemical line analysis was done using Energy Dispersive X-ray Spectroscopy (EDS). These SEM specimens were mounted and mechanically polished using a 3 μm diamond paste with a further polish for 24 hours in aqueous 0.05 μm silica slurry using a Vibromet to reveal the microstructure [31-32].

The crystallography of the phases was also identified by X-ray diffraction (XRD) using a Bruker D8 Discovery General Area Diffraction Detector System (GADDS) with Cu- K_{α} radiation as the source at a setting of 45 keV and 40 mA. The collected peaks were compared with the phase data found in the International Centre for Diffraction Data (ICDD) given in references [81-87]. Prior to XRD analysis, the pre-oxidation specimens were crushed and ground into a powder using a mortar and pestle which ensured a random texture and sufficiently large sampling volume from the powder particulates.

Oxidation Heat Treatments

Two sets of oxidation experiments were conducted on the two types of nitride specimens. Each specimen was sectioned into 3 x 3 x 3 mm cubes and polished using 120 grit SiC on all six surfaces. After polishing, the cubes were cleaned in ethanol for 8 hours, followed by an 8 hour ultra-sonic water rinse, followed by 8 hours of air drying. The cubes were placed in silica boats slid into a 99.5% alumina tube and heated under atmospheric conditions in a Sentro Tech Corp

1700 2.5-6 tube furnace using MoSi₂ heating elements. Pre- and post-oxidation specimens' masses were measured for change.

The first series of oxidation experiments (oxidation treatment I) entailed bringing the furnace up to the set-point of 650, 750, 850, and 950°C. The individual cube was inserted into the furnace where it was held for 3, 10, or 30 minutes and then removed and air quenched. The second oxidation experiments (oxidation treatment II) involved a pre-heat followed by a high temperature oxidation exposure. As will be discussed below, this pre-heat exposure was done to study the formation of an intermediate oxy-nitride layer which could minimize oxidation at higher temperatures. The pre-heat condition was at 650°C for 10 minutes and air quenched. After this treatment, the cube was inserted at 1200°C for 10 minutes and air quenched. For comparison, a non-pre-treat specimen (control) was heated at 1200°C for 10 minutes and air quenched.

Results

Pre-Oxidation characteristics:

The as-sprayed and sintered/HIP'ed nitride specimens' porosity and nitrogen content are tabulated in Table 4-1. The porosity measurements were estimated using the Delesse Principle which compares the surface area fraction of the total pore count divided by the total surface area of the image [57]. The reported densities were measured using a displacement fluid technique (Archimedes principle) and the initial powder nitrogen content was also characterized with LECO analysis. After spraying, approximately one-half of the nitrogen species is lost. The loss of nitrogen biases the system toward the precipitation of metal-rich nitride phases [20,25-26]. These phases, which include ζ -Hf₄N₃, ϵ -Hf₃N₂, γ -Ta₂N, δ -HfN, δ -TaN, α -Hf, and β -Ta, were confirmed by the XRD scan seen in Figure 4-1. These hafnium and tantalum nitride phases were also indexed in the EBSD phase map, Figure 4-2(b-c), of the sintered/HIP'ed specimen. This microstructure consisted of various grain sizes, with laths (determined to be ζ -Hf₄N₃ and ϵ -Hf₃N₂) within the grains. The balance of these phases appears to be either single grains of that phase and/or more globular morphologies of the individual phases in the microstructure. The volume fraction of these phases is tabulated in Table 4-2. The as-sprayed morphology consisted of the common splat-like microstructure, Figure 4-2(a). The small length scale of several of the as-sprayed granular features prevented high confidence EBSD identification; hence its corresponding phase map is not shown.

Specimen Processing	Homogenization		Nitrogen Content	
	Density (g/cc)	Porosity %	Initial (at.%)	Post (at.%)
As Sprayed	12.1	5.52	44.23	26.18
Sintered/HIP'ed	13.5	0.20	44.23	26.80

Table 4-1: Pre-heat treatment (left) homogenization density and porosity % values as well as the (right) nitrogen content. The initial nitrogen value (at.%) is based on starting powders, the post (at.%) is nitrogen content post-processing.

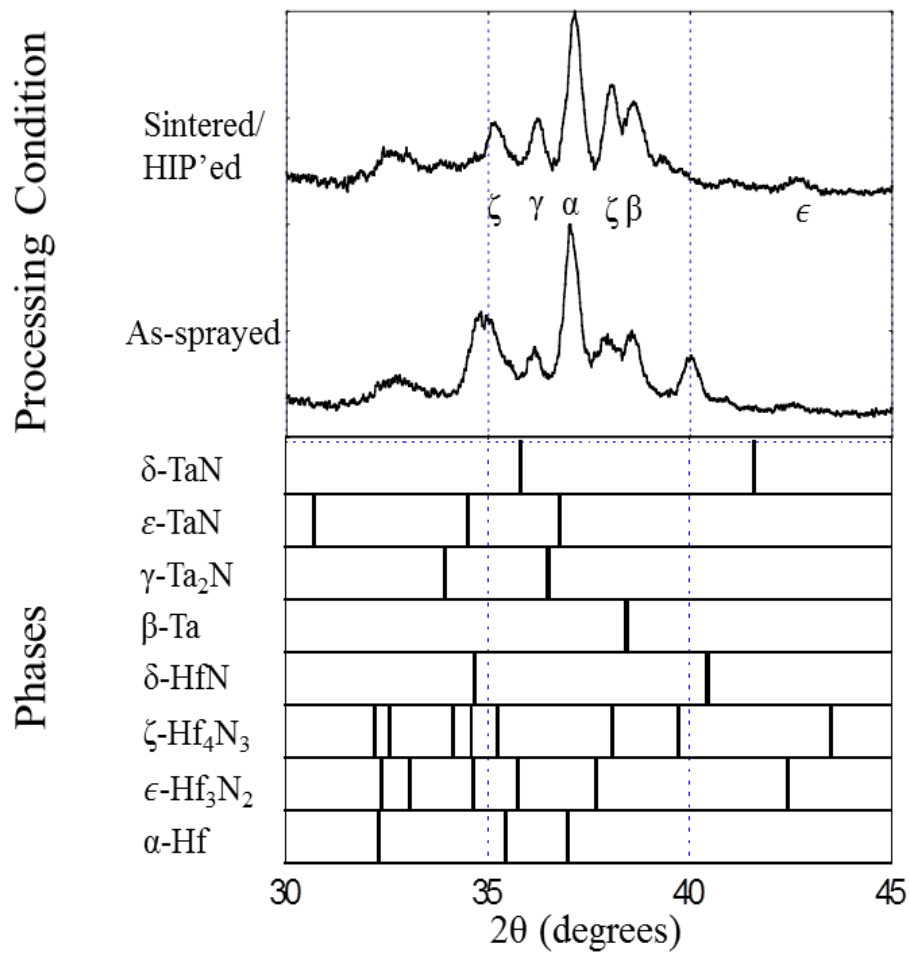


Figure 4-1: XRD of as-sprayed and sintered/HIP'ed pre-oxidation treatments.

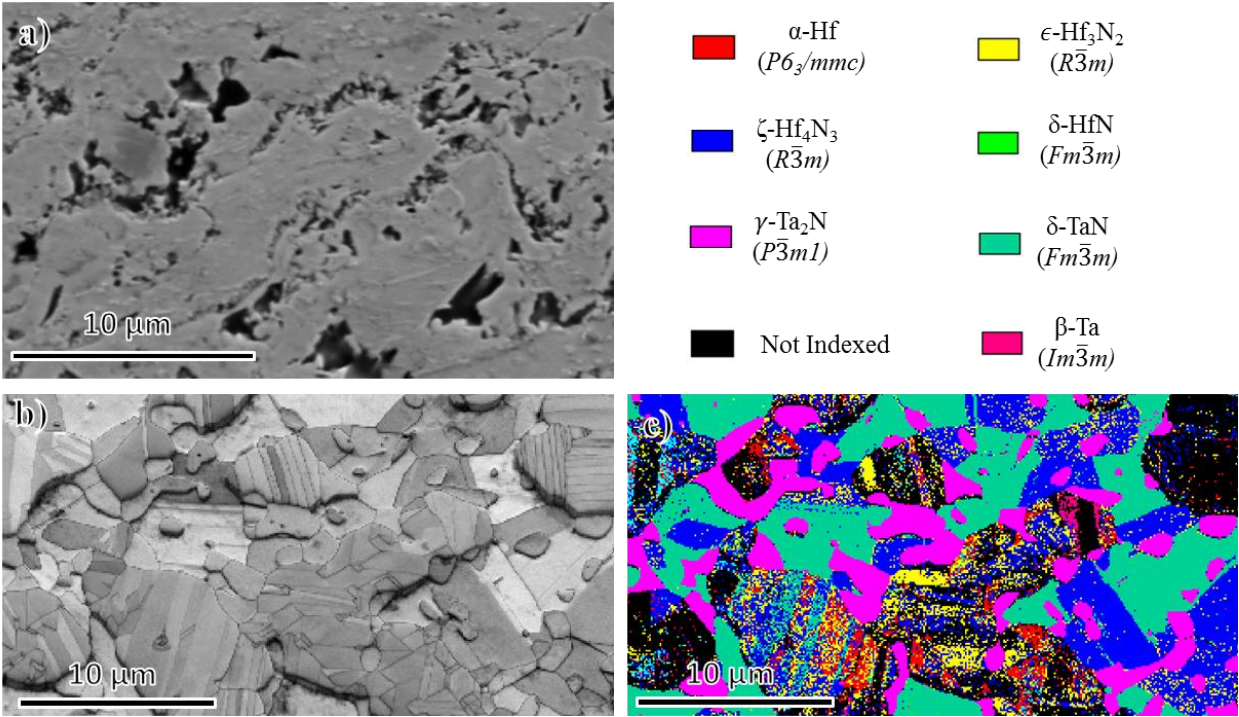


Figure 4-2: SEM image of as-sprayed microstructure (a). EBSD of sintered/HIP'ed specimen with quality reconstructed image (b) and phase content mapping (c). The phase content is matched based on colors found in the key.

Phase	Vol. %
α -Hf	3.5
ϵ -Hf ₃ N ₂	8.1
ζ -Hf ₄ N ₃	23.1
δ -HfN	0.2
β -Ta	0.4
γ -Ta ₂ N	14.4
δ -TaN	24.5
Unidentified	25.8

Table 4-2: EBSD phase content (volume %) of sintered/HIP'ed specimen pre-oxidation treatments.

Oxidation Treatment I

For all specimens, an increase mass change occurred with increasing temperature and time, as tabulated in Table 4-3. Comparing a single time as a function of temperature for the as-sprayed specimen, a larger mass change, which corresponded to visible spalling (not shown), was evident the intermediate temperatures of 750 and 850°C. This will be explained in the subsequent discussion. The cross-section imaged scale thicknesses were measured by overlaying an EDS line profile, which clearly identified the relative oxide content change with position, over an SEM micrograph, Figure 4-3(a). This figure reveals that an oxide scale as well as an intermediate or transitional layer was present. This intermediate layer can be seen from in the contrast change in the micrograph and composition change in the line scan, Figure 4-3(a). This layer is an oxy-nitride phase. The oxide scale thickness, Figure 4-3(b-c), grows with increasing temperature and time, with a noticeable increase at temperatures above 950°C. The sintered/HIP'ed specimen had an overall lower scale thickness of approximately 20 μm as compared to the as-sprayed specimen but shows a relative increase in growth at temperatures greater 950°C. The oxy-nitride intermediate layer thickness is also plotted and shows a relatively slow increase in thickness with increasing temperature and time.

Temperature (°C)	As-sprayed			Sintered/HIP'ed		
	3 min	10 min	30 min	3 min	10 min	30 min
650	0.10	0.22	1.83	0.01	0.06	0.05
750	0.06	0.97	3.00	0.04	0.04	0.06
850	0.09	0.92	2.01	0.02	0.14	0.15
950	0.19	0.45	0.96	0.01	0.02	0.63

Table 4-3: Oxidation treatment I mass % change for the (left) as-sprayed condition and (right) the additional sintered/HIP'ed. The oxidation heat treatment was for three times and four temperatures.

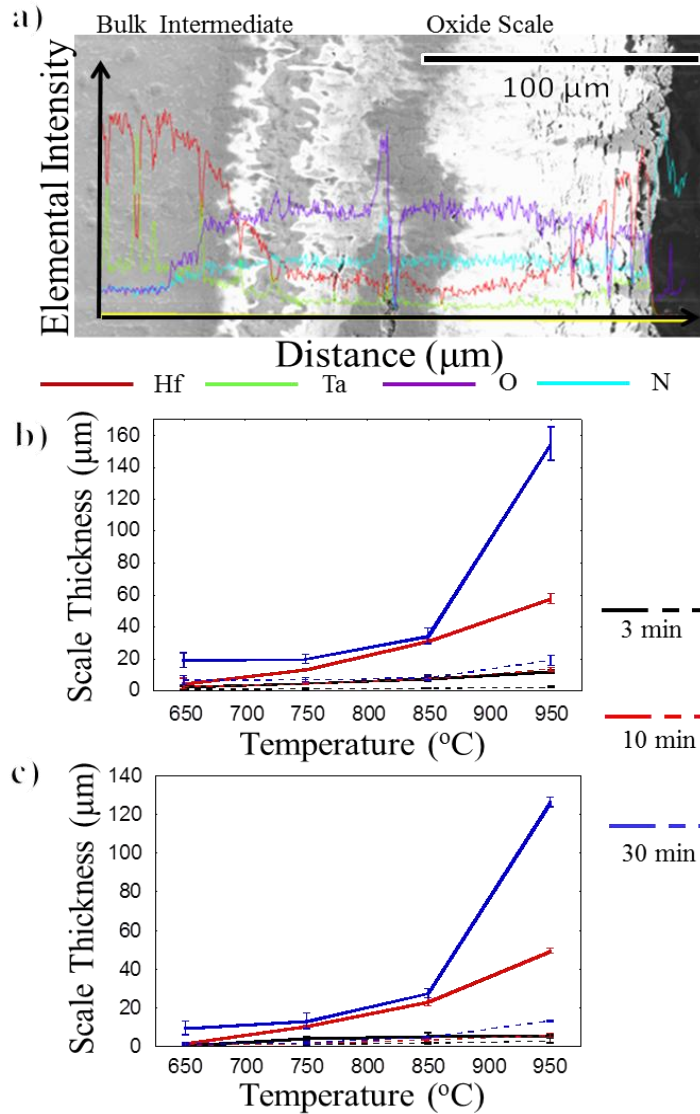


Figure 4-3: Scale thickness measurements of the post-oxidation treatment I measured with EDS line scans from SEM imaging (a). As-sprayed (b) with solid lines indicating oxide scale, dash is the intermediate scale, and color is based on the three times studied. Sintered/HIP'ed (c) with solid lines indicating oxide scale, dash is the intermediate scale, and color is based on the three times studied.

Oxidation Treatment II

Specimens were pre-treated at 650°C for 10 minutes to facilitate the growth of the prior noted oxy-nitride intermediate layer. This sub-set study aimed to determine if a preexisting oxy-nitride scale improved the oxidation behavior versus a specimen that forms the oxy-nitride layer while being oxidized simultaneously at higher temperatures. Once this layer was formed, these specimens were then re-oxidized at 1200°C for 10 minutes. The first group, denoted with a prefix of *C-*, is the *control* or non-pre-heat specimens for either the as-sprayed or sintered/HIP'ed. The second group, denoted with a prefix *T-*, is the *treated* results that had an oxy-nitride layer prior to exposure to the high temperature. For the sintered/HIP'ed specimens, a slight decrease in mass loss, Table 4-4, was measured between the control and pre-treated conditions. A corresponding decrease in oxide scale length and increase in the oxy-nitride scale length was noted between *C*-sintered/HIP'ed and *T*-sintered/HIP'ed, Figure 4-4. In contrast the treated as-sprayed specimen showed worse oxidation behavior than its control, Table 4-4. Similar to Figure 4-3, a corresponding increase in both oxy-nitride scale and oxide scale occurred for the control and treated specimens, Figure 4-4.

Temperature (°C)	As-sprayed		Sintered/HIP'ed	
	<i>C</i>	<i>T</i>	<i>C</i>	<i>T</i>
650	N/A	0.13	N/A	0.00
1200	0.87	3.19	0.49	0.44

Table 4-4: Oxidation treatment II mass % change for (left) as-sprayed conditions and (right) the additional sintered/HIP'ed. The first group *C*- had no low 650°C treatment but just 10 min oxidation at 1200°C follow by an air quench. The second group *T*- was oxidized for 10 min at 650°C followed by an air quench and then oxidized for 10 min at 1200°C with an air quench after.

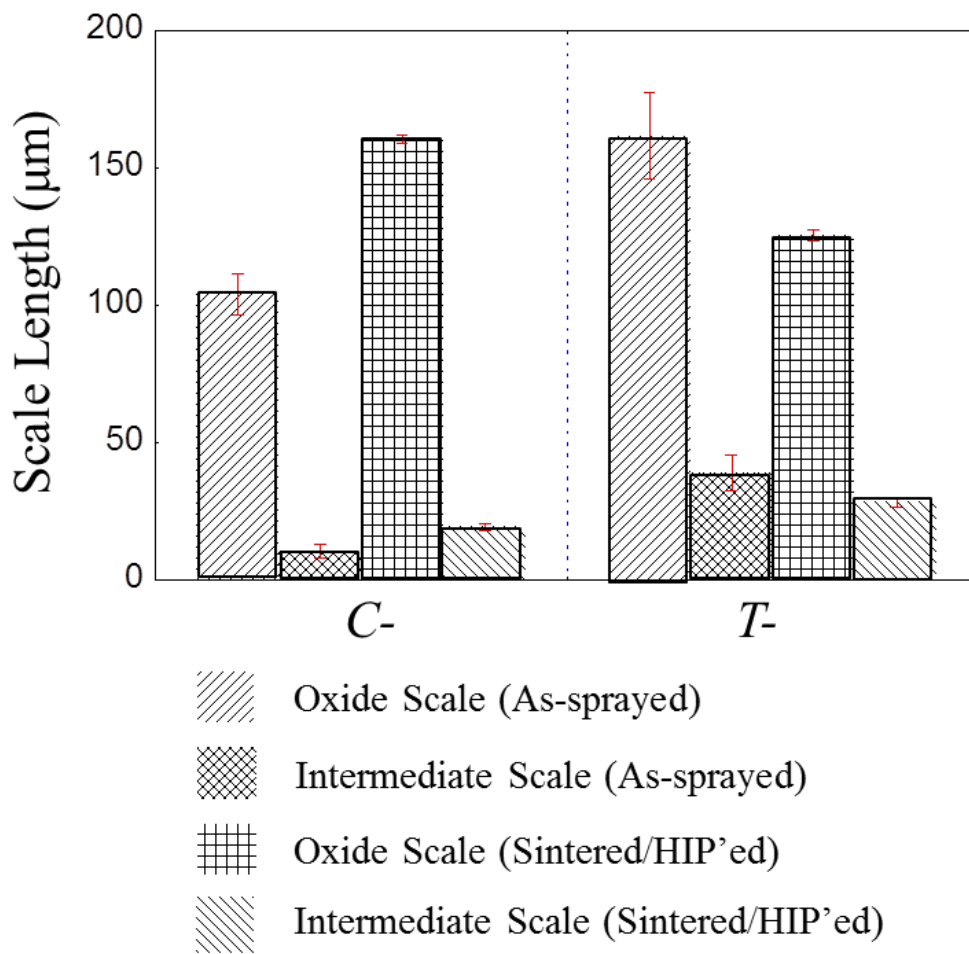


Figure 4-4: Measured EDS length of scales from the as-sprayed conditions (black and blue) and the additional sintered/HIP'ed (orange and green) post-oxidation treatment II. The *C*- without low 650°C oxidation is on the left while the *T*- with a low 10 min 650°C oxidation is on the right. Both groups were oxidized at 1200°C for 10 min with an air quench.

Discussion

The loss of nitrogen in the VPS process resulted in the precipitation of both elemental and metal-rich nitride phases, Figure 4-1. The VPS process is a dynamic fabrication method where powders are rapidly liquefied and solidified as they pass through a plasma plume [77]. In the liquid state, species can easily be lost from the starting solid state composition because of differences in vapor pressure which can be exasperated in a low pressure or vacuum environment and high temperatures. It is interesting to note that elemental hafnium and tantalum were both present in the VPS processed solid indicative that the nitride powders dissociated their species in the plasma plume. These phases and compositions were consistent with the previous processed specimen in reference [101].

As already reported [101], the oxide scale for this composition contained α -HfO₂, L-Ta₂O₅ and an oxy-nitride Hf₇O₈N₄ [94] scale. The formation of this oxy-nitride scale is facilitated by the presence of these rhombohedral phases [9]. These ϵ -Hf₃N₂ and ζ -Hf₄N₃ phases appear to be anion vacancy wells for absorbing the oxygen. This is observed by the increase in oxygen content noted in the line scan across a $[11\bar{2}0]$ orientated ϵ -Hf₃N₂ lath, Figure 4-5(a-c). The gettering oxygen by the rhombohedral ϵ -Hf₃N₂ and ζ -Hf₄N₃ phases and the stabilization of an oxy-nitride layer appears to help regulate the oxidation rate within these nitride microstructures.

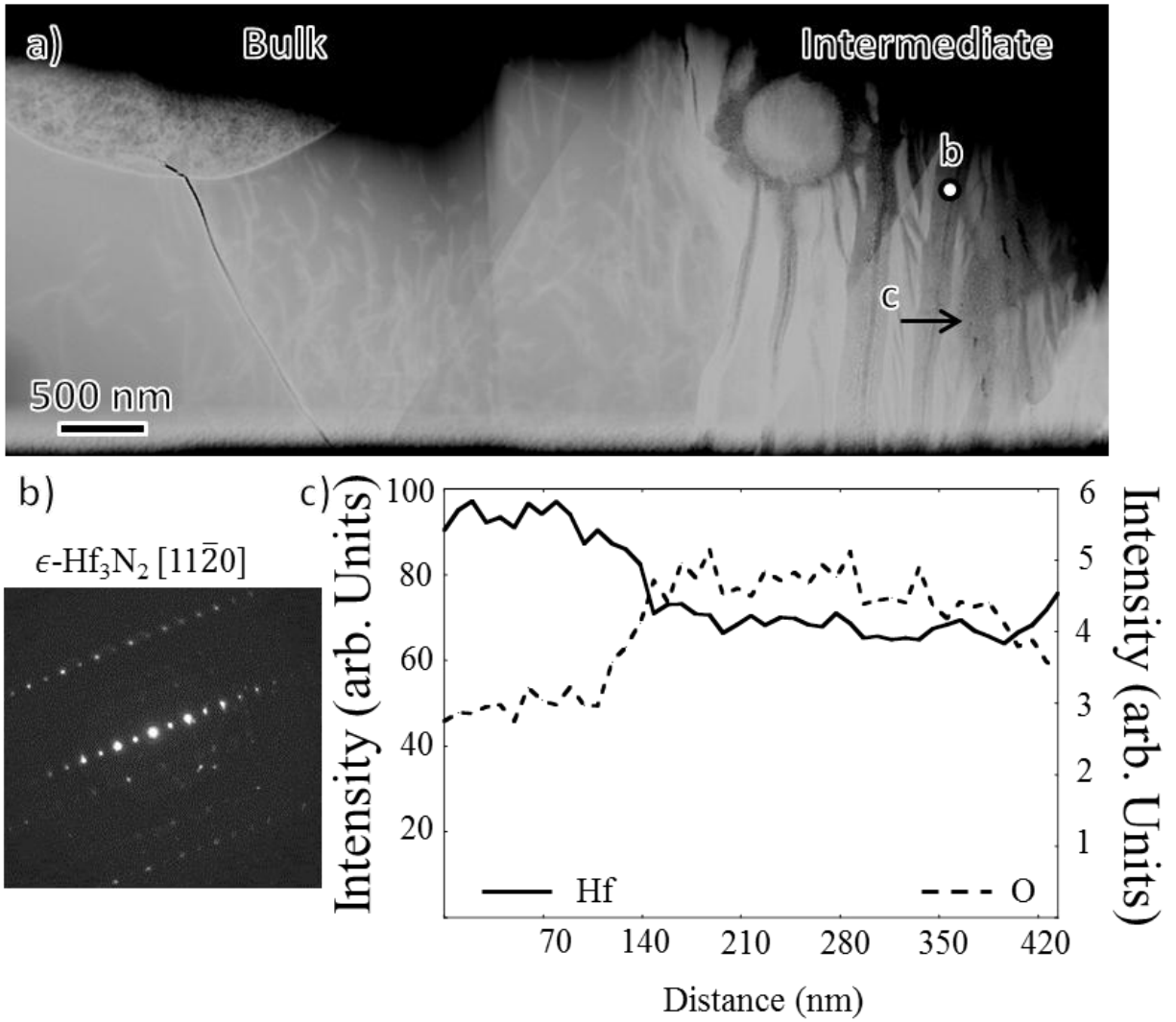


Figure 4-5: STEM-HAADF images and SAED of a FIB lift-out foil from the *T*-sintered/HIP'ed. STEM image (a) of FIB lift-out foil with the bulk region on left, intermediate on right, marked SAED diffraction pattern location, and STEM EDS line profile. The SAED diffraction pattern (b) identifies the lath-like microstructure as $\epsilon\text{-Hf}_3\text{N}_2$. The EDS line profile (c) across this lath indicates hafnium (intensity on left axis) and oxygen (intensity on right axis) content.

In the as-sprayed specimens, the inherent porosity provided initiation sites for the oxidation reaction layer. This is evident in the noticeable mass change and spalling that occurred for the as-sprayed specimens versus the consolidated specimens at 750-850°C, Table 4-3. The high pore content specimen allowed simultaneous intermediate scale formation at the surface as well as boundary mechanisms to be active. These mechanisms caused oxygen to penetrate further into the material and initiate more oxidation of the material through its increased surface area as compared to the consolidated post-processed specimens. Once the oxy-nitride scale became continuous and coarse (950°C in Figure 4-3(b)), the as-sprayed material showed a reduction in mass change (950°C in Table 4-3). The lack of spalling was used to infer that this oxy-nitride layer was continuous. Consequently, the oxidation rate was limited by the oxygen diffusion through the intermediate oxy-nitride layer and not by the progression of new oxidation reaction site initiation. This suggests that the presence of a preexisting oxy-nitride scale could be beneficial in reducing oxidation within these materials.

A preexisting oxy-nitride layer was processed into both as-sprayed and sintered/HIP'ed specimens by annealing them at 650°C. After this pre-treatment, they were directly exposed to 1200°C. The *T*-sintered/HIP'ed specimen showed a lower mass change and lower oxide scale growth than that of the *C*-sintered/HIP'ed specimen, Table 4-4 and Figure 4-5. In addition, the oxy-nitride scale coarsened under the high temperature treatment. This suggests that the oxy-nitride scale is stable (does not decompose) at this high temperatures tested condition since it increased in length from its pre-treated value. Also, the presence of the pre-treat oxy-nitride scale did help reduce the rate of oxidation compared to the control.

Surprisingly, the as-sprayed specimens did not show this beneficial mass loss reduction. The control specimen had better oxidation resistance than the pre-treat. This difference is believed to be a result of cracking. The pre-heat and subsequent air quench caused the as-sprayed porosity to crack, Figure 4-6(a). Associated with this cracking, the oxy-nitride layer was no longer continuous. When the as-sprayed specimen was then exposed to the higher temperature oxidation test, these crack surfaces provided virgin oxidation initiation sites. Consequently, boundary controlled mechanisms could dominate the oxidation rate and result in more mass loss. This severe micro-cracking was not evident in the sintered/HIP'ed specimens, Figure 4-6(b), which allowed the continuous oxy-nitride scale to be retained.

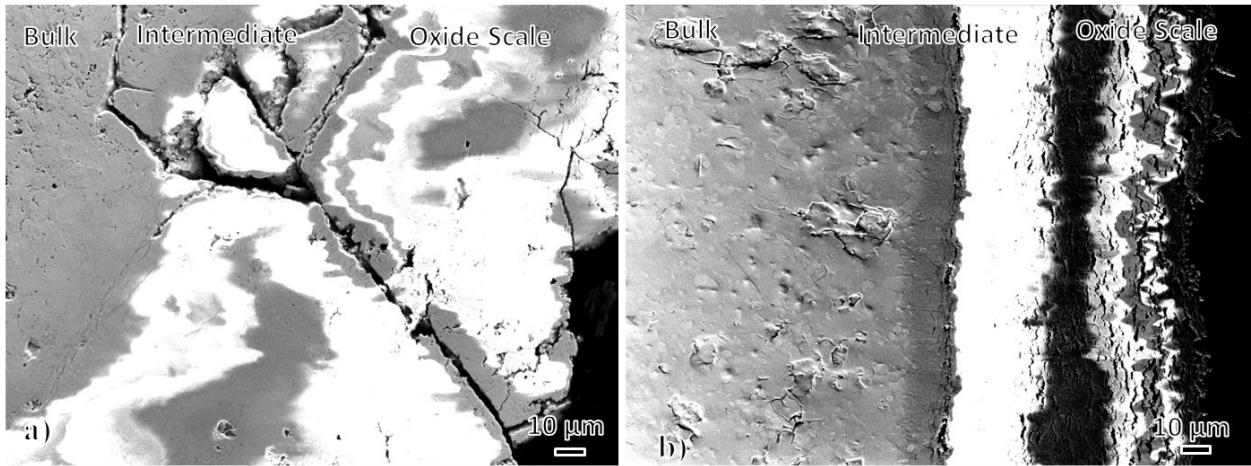


Figure 4-6: Example SEM imaging of (a) as-sprayed condition and (b) the additional sintered/HIP'ed post-oxidation treatment II for *T*-set. Approximate locations of oxide scale (note the observable charging), intermediate and bulk are marked.

Conclusion

The increase in density for the VPS with additional sintered/HIP'ed processing 80HfN-20TaN nitrides improved oxidation resistance. The reaction of hafnium nitride conversion into hafnia was found to be affected by both boundary and diffusion mechanisms. Boundary oxidation mechanisms were significant in specimens with increased porosity and that were subjected to cracking, possibly from thermal expansion stresses. Specimens with low porosity minimized boundary oxidation, and the inherent nitrogen loss from the high temperature processing led to the formation of close-packed phases. These close-packed phases aided in limiting the diffusion of oxygen through an adherent oxy-nitride intermediate layer. Growth of this oxy-nitride intermediate layer was found to begin as low as 650°C and negligible mass loss was noted under 950°C (for consolidated material). When this oxy-nitride intermediate layer was pre-grown at low temperatures the specimens with low cracks and porosity demonstrated improved oxidation resistance. Not only was there an observable difference in mass change but also in the oxy-nitride scale thickness. Above 950°C, where mass changes were noted due to higher temperature kinetics rather than a break of the oxy-nitride, the oxy-nitride layer thickened and was observed to coarsen suggesting that it was not unstable. By coarsening a preexisting continuous scale the oxidation was further reduced.

The TEM analysis of this improved pre-grown oxy-nitride intermediate layer revealed ϵ -Hf₃N₂ laths with increased oxygen content. It is believed that these close-packed like structures acted as anion vacancy wells, or getters, for oxygen. It was also found that consolidation of microstructure was also critical for it reduces porosity which determinately decreases the exposed surface area for oxidation. This lower porosity also minimized crack initiation sites upon thermal cycles which further protected the continuous oxy-nitride layer. Therefore, not only did the high density minimize boundary oxidation but the pre-grown oxy-nitride also lowered the rate of oxygen diffusion through the reaction layer.

CHAPTER 5

CONCLUSION AND FUTURE DIRECTIONS

A study of the phase content on multi-processed nitrides was completed and addressed in Chapters 2-4. In Chapter 2, two sets of hafnium nitride diffusion couples were processed by hot-isostatic pressing and their resulting microstructure and phase orientation were identified. Distinct regions were found in the diffusion couples. The first diffusion couple heat treated at 1900°C at 2 hrs revealed a combined phase region of ϵ -Hf₃N₂ grains with α -Hf laths, a dominant ζ -Hf₄N₃ grain region, and a mixed δ -HfN grains with ζ -Hf₄N₃ laths region between the initial α -Hf and δ -HfN diffused materials. The second diffusion couple heat treated at 1200°C for 12 hrs revealed similar regions except the mixed δ -HfN grains with ζ -Hf₄N₃ laths region was not present. Instead, the reaction zone transitioned directly from the initial δ -HfN to a mixed ϵ -Hf₃N₂ and ζ -Hf₄N₃ region. It was shown that the rhombohedral ζ -Hf₄N₃ phase, like other M₄X₃ UHTCs, formed through elemental migration along close-packed planes from FCC structures. Lattice parameter calculations from the high temperature diffusion couple verified homogeneity ranges of ϵ -Hf₃N₂ and ζ -Hf₄N₃.

In Chapter 3, a series of (HfN)_{1-x}(TaN)_x compositionally mixed powders where X= 0.0, 18.8, 28.1, and 46.7 at.% were processed with a vacuum plasma spray. The resulting nitrides had significant nitrogen content loss. This nitrogen loss is known to occur for the non-equilibrium parameters during VPS processing. This loss of nitrogen and the use of a ternary phase diagram were used to explain the presence of metal-rich phases. With sufficient nitrogen loss the formation of elemental α -Hf and β -Ta formed. When nitride compositions underwent two oxidation experiments between 400-1600°C it was found that this presence of β -Ta readily formed α -Ta₂O₅. The dominant oxide scale was found to be a white powder α -HfO₂. The specimen with the lowest mass change, 18.8 at.%, contained a lower β -Ta peak compared to α -Hf and a balance of the close-packed like structures of ϵ -Hf₃N₂, ζ -Hf₄N₃ and γ -Ta₂N phases. This composition developed a dark intermediate oxy-nitride phase between the oxide scale and bulk. XRD data identified three oxy-nitrides; the Hf₇O₈N₄ and the rhombohedral Hf-N based ζ -Hf₄O_xN₃ and ϵ -Hf₃O_xN₂ phases. STEM EDS line profiles suggested that the rhombohedral Hf-N

phases acted as oxygen getters and provide heterogeneous nucleation sites for forming the oxy-nitride. These phases were derived from the inherent interstitial vacancy of the ζ -Hf₄N₃ and ϵ -Hf₃N₂ phases that became filled with oxygen. The rhombohedral phases behaved as *n*-type anion vacancy oxygen getters. It is believed that these metal-rich nitride phases are advantageous to oxidation resistance by acting as a passivation layer at the ceramic bulk/oxide scale interface by minimizing oxygen diffusion through the close-packed like crystal lattices.

Processing conditions were studied in Chapter 4 where the 80HfN-20TaN composition from Chapter 3 was expanded upon. The increase in density for the VPS with additional sintered/HIP'ed processed nitrides improved oxidation resistance. The reaction of hafnium nitride conversion into hafnia was found to be affected by both boundary and diffusion mechanisms. Boundary oxidation mechanisms were significant in specimens with increased porosity and that were subjected to cracking, possibly from thermal expansion stresses. Specimens with low porosity minimized boundary oxidation, and the inherent nitrogen loss from the high temperature processing led to the formation of close-packed phases. These close-packed phases aided in limiting the diffusion of oxygen through an adherent oxy-nitride intermediate layer. Growth of this oxy-nitride intermediate layer was found to begin as low as 650°C and negligible mass loss was noted under 950°C (for consolidated material). When this oxy-nitride intermediate layer was pre-grown at low temperatures the specimens with low cracks and porosity demonstrated improved oxidation resistance. Not only was there an observable difference in mass change but also in the oxy-nitride scale thickness. Above 950°C, where mass changes were noted due to higher temperature kinetics rather than a break of the oxy-nitride, the oxy-nitride layer thickened and was observed to coarsen suggesting that it was not unstable. By coarsening a preexisting continuous scale the oxidation was further reduced.

The TEM analysis of this improved pre-grown oxy-nitride intermediate layer revealed ϵ -Hf₃N₂ laths with increased oxygen content. It is believed that these close-packed like structures acted as anion vacancy wells, or getters, for oxygen. It was also found that consolidation of microstructure was also critical for it reduces porosity which determinately decreases the exposed surface area for oxidation. This lower porosity also minimized crack initiation sites upon thermal cycles which further protected the continuous oxy-nitride layer. Therefore, not only did the high density minimize boundary oxidation but the pre-grown oxy-nitride also lowered the rate of oxygen diffusion through the reaction layer.

Although, it was found that a specific hafnium-tantalum-nitrogen composition improved oxidation resistance through the formation of oxy-nitride layers via the vacancy of hafnium-nitride rhombohedral phases, additional work would be beneficial. (1) This work began with a diffusion couple between hafnium-nitrogen to focus on the microstructure and orientation characterization of the rhombohedral phases in Chapter 2. This diffusion couple thermodynamic analysis could be expanded to the tantalum-nitrogen system and even ternary systems with oxygen. This could explore the rates of diffusion between the multiple hafnium-nitrogen and tantalum-nitrogen phases, along with oxygen. This would help provide computational values in building a kinetic model to further understand the phase transformation between these hafnium-tantalum-nitrides and their oxides. (2) Improvements to the processing correlation with the oxy-nitride interface are also suggested. One method for achieving this was discussed in Chapter 3, the use of density functional theory (DFT) for modeling the possible oxy-nitride reactions. DFT can contribute by computing the increase in phase energy for various possible oxidation reactions. For instance, it is hypothesized that the rhombohedral hafnium nitrides provide a favorable initial oxygen diffusion pathway versus the other nitrides; hence they behave as vacancy diffusion wells. By computing the phase transformation energy with DFT between hafnium nitrides and the ϵ -Hf₃O_xN₂ ζ -Hf₄O_xN₃ oxygen vacancy filled phases it is possible to show that this initial ‘getting’ of oxygen is favorable. What DFT could further show is whether the transformation from these oxy-nitrides to monoclinic hafnia is steeper energetically than base hafnium nitrides. By sacrificing some oxygen diffusion, it is possible that the oxy-nitrides are able to maintain their similar bulk crystallographic structure and provide a larger phase transformation energy barrier into hafnia. Analyzing (4) these oxy-nitrides at higher temperatures above 1700°C as well as determining the chemistry of the oxy-nitrides to couple with their lattice parameters would be beneficial. Another concept (5) from Chapters 3 and 4, the passivation behavior of the oxy-nitride intermediate layer could be further explored with a series of polarization E_{corr} studies to establish a possible critical current for passivity. Lastly, (6) the next direct step in this study is the analysis of different low-tantalum addition compositions with hafnium nitride and the mechanical behavior, specifically the thermal expansion stresses found in these phases.

REFERENCES

- [1] E. Wuchina, E. Opila, M. Opeka, W. Fahrenholtz, and I. Talmy, "UHTCS: Ultra-High Temperature Ceramic Materials for Extreme Environment Applications," *The Electrochemical Society Interface*, (2007) 30-36.
- [2] Perry, "The Refractories HfC and HfN - A survey," *Powd Metall Int*, 19(1), (1987) 29-35.
- [3] B.O. Johansson, U. Helmersson, M.K. Hibbs, and J.-E. Sundgren, "Reactively magnetron sputtered Hf-N film. I. Composition and structure," *J App Phys*, 58, (1985) 3104.
- [4] Carney, Parthasarathy, and Cinibulk, "Oxidation Resistance of Hafnium Diboride Ceramics with Additions of Silicon Carbide and Tungsten Boride or Tungsten Carbide," *J Am Ceram Soc*, 94(8), (2011) 2600-2607.
- [5] Allen L. Bowman, "The variation of lattice parameter with carbon content of tantalum carbide," *J. Phys. Chem*, 65(9), (1961) 1596-1598.
- [6] M. Desmaison, N. Alexandre, and J. Desmaison, "Comparison of the Oxidation Behavior of Two Dense Hot Isostatically Pressed Tantalum Carbide (TaC and Ta₂C) Materials," *J Eur Ceram Soc*, 17, (1997) 1325-1334.
- [7] Desmaison, Alexandre, and J. Desmaison, "Comparison of the Oxidation Behavior of Two Dense hot Isostatically Pressed Tantalum Carbide (TaC and Ta₂C) Materials," *J. Euro Ceram Soc*, 17, (1997) 1325-1344.
- [8] Kenneth Hackett, Shane Verhoef, Raymond A. Cutler, and Dinesh K. Shetty, "Phase Constitution and Mechanical Properties of Carbides in the Ta-C system," *J. Am. Ceram. Soc.*, 92(10), (2009) 2404-2407.
- [9] M. Desmaison-Brut, J. Montintin, "Mechanical Properties and Oxidation Behavior of HIPed Hafnium Nitride Ceramics," *J Euro Ceram Soc*, 13, (1994) 379-386.
- [10] Shimada, "A thermoanalytical study of the oxidation of ZrC and HfC powders with formation of carbon," *Solid State Ionics*, 149, (2002) 319-326.
- [11] Shimada, "Interfacial reaction on oxidation of carbides with formation of carbon," *Solid State Ionics*, 141, (2001) 99-104.
- [12] Shimada and Inagaki, "A kinetic study of oxidation of niobium carbide," *Solid State Ionics*, 63, (1993) 312-317.

- [13] Parthasarathy, Kerans, and Opeka, "A Model for the Oxidation of Refractory Diborides," Air Force Research Laboratory (2007).
- [14] Parthasarathy, Rapp, Opeka, and Kerans, "A model for the oxidation of ZrB₂, HfB₂, and TiB₂," *Acta Mat*, 55, (2007) 5999-6010.
- [15] Parthasarathy, Rapp, Opeka, and Kerans, "Effects of Phase Change and Oxygen Permeability in Oxide Scales on Oxidation Kinetics of ZrB₂ and HfB₂," *J Am Ceram Soc*, 92(5), (2009) 1079-1086.
- [16] R.B. Srinivasa, V. Musaramthota, D. Lahirir, V. Singh, S. Seal and A. Agarwal, "Spark plasma sintered tantalum carbide: Effect of pressure and nano-baron carbide addition on microstructure and mechanical properties," *Mat. Sci. Eng. A*, 528, (2011) 1287-1295.
- [17] Boncoeur Alexandre, Desmaison-Brut, and Valin, "Mechanical properties of hot isostatically pressed zirconium nitride materials," *J. Mater. Sci.*, 28, (1993) 2385-90.
- [18] Andreas Zerr, Gerhard Miehe, and Ralf Riedel, "Synthesis of cubic zirconium and hafnium nitride having Th₃P₄ structure," *Nature Materials*, 2, (2003).
- [19] Brady, Fuss, and Gerstenberg, "Thermal Oxidation and Resistivity of Tantalum Nitride Films," *Thin Solid Films*, 66, (1980) 287-302.
- [20] Booker and Brukl, "Part VI. The Phase Equilibria in the Metal-Rich Region of the Hafnium-Tantalum-Nitrogen System," in *Phase Equilibria Investigation of Binary, Ternary, and Higher Order Systems.*, (1967).
- [21] A. Zerr, R. Boehler, R. Riedel D. A. Dzivenko, "Equation of state of cubic hafnium (IV) nitride having Th₃P₄-type structure," *Solid State Communications*, 139, (2006) 255-258.
- [22] Desmaison-Brut, L. Themalin, Valin, and Boncoeur, "Mechanical properties of HIPed titanium nitride," *Euro-Ceramics*, 3, (1989).
- [23] P. Kroll, "Assessment of the Hf-N, Zr-N and Ti-N phase diagrams at high pressures and temperatures: balancing between MN and M₃N₄," *J Phys: condens Matter*, 16, (2004) 1235-1244.
- [24] P. Kroll, "Hafnium Nitride with Thorium Phosphide Structure: Physical Properties and an Assessment of the Hf-N, Zr-N, and Ti-N Phase Diagrams at High Pressures and Temperatures," *Phy Rev Lett*, 90(12), (2003).
- [25] Okamoto, "N-Ta (Nitrogen-Tantalum)," *J Phase Equilibria and Diffusion*, 29(3), (2008)

291.

- [26] Okamoto, "The Hf-N (Hafnium-Nitrogen) System," *Bulletin of Alloy Phase Diagrams*, 11(2), (1990).
- [27] E. Rudy, "The Crystal Structures of Hf₃N₂ and Hf₄N₃," *Met Trans*, 1, (1970) 1249-1252.
- [28] W. Lengauer, D. Rafaja, R. Taubler, C. Kral and P. Ettmayer, "Preparation of Binary Single-Phase Line Compounds Via Diffusion Couples; The subnitride phases Hf₃N₂ and Hf₄N₃," *Acta metall mater*, 41(12), (1993) 3505-3514.
- [29] W. Lengauer, S. Binder, K. Aigner, P. Ettmayer, A. Guillou, J. Debuigne, and G. Groboth, "Solid state properties of group IVb carbonitrides," *J Alloys and Compunds*, 217, (1995) 137-147.
- [30] A.L. Bowman, T.C. Wallace, J.L. Yarnell, R.G. Wenzel, and E.K. Storms, "The crystal structures of V₂C and Ta₂C," *Acta Cryst.*, 19, (1965) 6-9.
- [31] R.A. Morris, B. Wang, GB Thompson and D. Butts, "Variation in tantalum carbide microstructures with changing carbon content," *J App Cerm Tec*, 89, (2012).
- [32] R.A. Morris, B. Wang, L. Matson, and G.B. Thompson, "Microstructural formations and phase transformations pathways in hot isostatically pressed tantalum carbides," *Acta Mat*, 60, (2012) 139-148.
- [33] H. Nowotny, E. Rudy and F. Benesovsky, "Untersuchungen in den Systemen: Hafnium Bor Kohlenstoff und Zirkonium Bor Kohlenstoff," *Mh Chem*, 92, (1961).
- [34] M. Opeka, I. Talmy, E. Wuchina, J. Zaykoski, and S. Causey, "Mechanical, Thermal, and Oxidation Properties of Refractory Hafnium and Zirconium Compounds," *J. Euro Ceram Soc*, 19, (1999) 2405-2414.
- [35] Shimada, "Microstructural observation of ZrO₂ scales formed by oxidation of ZrC single crystals with formation of carbon," *Solid State Ionics*, 101, (1997) 749-753.
- [36] K Balani, G. Gonzalez and A. Agarwal, "Synthesis, microstructure characterization, and mechanical property evaluation of vacuum plasma sprayed tantalum carbide," *J Am Ceram Soc*, 89(4), (2006) 1419-1425.
- [37] Shimada, Nakajima, and Inagaki, "Oxidation of SIngle Crystals of hanfium Carbide in a Temperature Range of 600 to 900C," *J Am Ceram Soc*, 80(7), (1997) 1749-56.

- [38] E. Rudy and H. Nowotny, "Untersuchungen im System Hafnium-Tantal-Kohlenstoff," *Mh. Chem.*, 94, (1963).
- [39] E.K. Storms, *The Refractory Carbides*. New York: Academic Press, 1967.
- [40] E. Rudy and F. Benesovsky, "Untersuchungen in den Systemen: Hafnium Bor Stickstoff und Zirkonium Bor Stickstoff," *Mh. Chem.*, 92, (1961).
- [41] Rudy, Windisch, and Chang, Air Force Technical Report AFML-TR-65-2, 1, (1965).
- [42] Denny A. Jones, *Principles and Prevention of Corrosion*. Upper Saddle River, NJ: Prentice-Hall, Inc., 1996.
- [43] A.S. Khanna, "Introduction to High Temperature Oxidation and Corrosion", ASM International, Materials Park, OH. 2002.
- [44] N.B. Pilling and R.E. Bedworth, "The Oxidation of Metals at High Temperatures," *J. Inst. Met*, 29, (1923) 529-591.
- [45] "ASM Handbook vol. 13 Corrosion," in *ASM Handbook International.*, 1987.
- [46] M. Desmaison, M. Billy, and J. Desmaison, "Oxydation du nitrure de hafnium par l'oxygene," *Annal Chim*, 4, (1979) 85-92.
- [47] M. Desmaison, M. Billy, and J. Desmaison, "Oxydation du nitrure de hafnium par le dioxyde de carbone," *Anal Cehm*, 10, (1985) 93-103.
- [48] D Shin, R Arroyave, and Z. Liu, "Thermodynamic modeling of the Hf-Si-O System," *Computer Coupling of Phase Diagrams and Thermochemistry*, 0, (2008).
- [49] Desmaison-Brut, Boncoeur, Valin Montintin, "Microstructure, mechanical propertie and oxidation behavior of hot isostatic pressed tantalum nitride," in *Proceedings of hot isostatic pressing: Theory and Applications*, 1989.
- [50] K. Kelley, "The Specific Heats at Low Temperatures of Tantalum Oxide and Tantalum Carbide", *Metallurgical Fundamentals Section, United States Department of the Interior*, 1940.
- [51] V.I. Khikova, V.V. Klechkovskaya, and Z.G. Pinkser, *Kristallografiya*, 17, (1972) 506.
- [52] A. Reisman, F. Holtzberg, M. Berkenblit, and M. Berry, *J. Am. Chem. Soc.*, 78, (1956) 4514.

- [53] Shimada, Nakajima, and Inagaki, "Oxidation of Single Crystals of hafnium Carbide in a Temperature Range of 600 to 900C," *J Am Ceram Soc*, 80(7), (1997) 1749-56.
- [54] D.B. Carter and C.B. Williams, *Transmission Electron Microscopy: a Textbook for Materials Science*. New York, NY: Springer Science, 1996.
- [55] L.A. Giannuzzi, "Reducing FIB Damage Using Low Energy Ions," *J Microscopy Microanalysis*, 12(2), (2006) 1260-1261.
- [56] L.A. Giannuzzi, R. Geurts, and J. Ringnalda, "2 keV Ga⁺ FIB Milling for Reducing Amorphous Damage in Silicon," *J Microscopy and Microanalysis*, 11(2), (2005) 828-829.
- [57] E.R. Weibel, *Stereological methods*. New York, NY: Academic Press/Harcourt Brace Jovanovich, 1989.
- [58] "HfN 00-033-0592," International Centre for Diffraction Data, 1982.
- [59] "Hf₃N₂ 00-023-1097," International Centre for Diffraction Data, 1970.
- [60] "Hf₃N₄ 01-072-8063," International Centre for Diffraction Data, 2003.
- [61] "Hf₄N₃ 00-023-1096," International Centre for Diffraction Data, 2010.
- [62] B.O. Johansson, U. Helmersson, M.K. Hibbs, and J.-E. Sundgren, "Reactively magnetron sputtered Hf-N films I. Composition and Structure," *J Appl Phys*, 58, (1985).
- [63] Liu Limeng, Ye Feng, and Zhou Yu, "Microstructure and Mechanical Properties of Spark Plasma Sintered TaC_{0.7} Ceramics," *J. Am. Ceram. Soc.*, 93(10), (2010) 2945-2947.
- [64] Gregory M. Demyashev, "Review: Transition metal-based nanolamellar phases," *Prog. in Mat Sci*, 55, (2010) 629-674.
- [65] H. McMurdie, M. Morris, E. Evans, B. Paretzkin, W. Wong-Ng, and Y. Zhang, *Powder Diffraction*, 2, (1987) 46.
- [66] Fiala, Central Research Institute, SKODA, Czechoslovakia, 1973.
- [67] C. Suryanarayana and M.G. Norton, *X-Ray Diffraction: A Practical Approach*. New York: Plenum Press, 1998.
- [68] D.J. Rowcliffe and G. Thomas, "Structure of Non-Stoichiometric TaC," *Mat Sci and Eng*, 18, (1975) 231-238.

- [69] Paul G. Shewmon, Jenks, OK: J. Williams Book Company, 1983.
- [70] J.G. Mullen, "Effect of Bardeen-Herring Correlation on Vacancy Diffusion in Anisotropic Crystals," *Phys Rev*, 124(6), (1961) 1723-1730.
- [71] W. Lengauer, D. Rafaja, G. Zehetner, and P. Ettmayer, "The Hafnium-Nitrogen System: Phase Equilibria and Nitrogen Diffusivities Obtained from Diffusion Couples," *Acta mater.*, 44(8), (1996) 3331-3338.
- [72] A.I. Gusev, A.S. Kurlov, and V.N. Lipatnikov, "Atomic and vacancy ordering in carbide Z-Ta₄C₃ and Phase equilibria in the Ta-C System," *J. Solid State Chem.*, 180, (2007) 3234-3246.
- [73] E. Rudy, R. Ruetz, and H. Nowotny, "Carbon-Hafnium-Tantalum Ternary Alloy Phase Diagram," ASM Alloy Phase Diagrams Center (2006).
- [74] Wuchina, "Processing and mechanical properties of materials in the Hf-N system," *J. Euro. Ceram. Soc.*, 22, (2002) 2571-2576.
- [75] Wuchina, "Oxidation of Hf-based nitrides and borides," *Electrochemical Soc Proceedings*, 16, (2004) 240-252.
- [76] Okamoto, "Hf-O (Hafnium-Oxygen)," ASM International, 29(124), (2008).
- [77] B.C. Schulz, B. Wang, R.A. Morris, D. Butts, and G.B. Thompson, "Influence of hafnium carbide on vacuum plasma spray processed tantalum carbide microstructures," *J. Euro. Ceram. Society*, 33, (2013) 1219-1224.
- [78] L. Trignan-Piot, M. Berardo, J. Gastaldi, and S. Giorgio, "Influence of plasma spraying parameters on the carbon content and porosity of TaC coatings," *Surf. and Coatings Tech.*, 79, (1996) 113-118.
- [79] D.B. Carter and C.B. Williams, *Transmission Electron Microscopy: a Textbook for Materials Science*. New York: Springer Science, 1996.
- [80] ASM International, *Handbook of Thermal Spray Technology*. Materials Park, OH, United States of America: ASM International, 2004.
- [81] 2012 International Centre for Diffraction Data, "00-038-1478 (Alpha Hf),".
- [82] 2013 International Centre for Diffraction Data, "04-004-6450 (HfN_{0.67}),".

- [83] 2013 International Centre for Diffraction Data, "04-004-6451 (HfN_{0.75})",
- [84] 2013 International Centre for Diffraction Data, "00-025-1410 (HfN)",
- [85] 2012 International Centre for Diffraction Data, "00-004-0788 (Cubic Ta)",
- [86] 2012 International Centre for Diffraction Data, "01-089-4764 (Ta₂N)",
- [87] 2012 International Centre for Diffraction Data, "00-039-1485 (Hex TaN)",
- [88] 2012 International Centre for Diffraction Data, "00-049-1283 (Cubic TaN)",
- [89] 2013 International Centre for Diffraction Data, "00-006-0318 (Mono HfO₂)",
- [90] 2013 International Centre for Diffraction Data, "00-008-0342 (Tetra HfO₂)",
- [91] 2013 International Centre for Diffraction Data, "00-021-0904 (Ortho HfO₂)",
- [92] 2013 International Centre for Diffraction Data, "00-053-0550 (Cubic HfO₂)",
- [93] 2013 International Centre for Diffraction Data, "00-050-1171 (Cubic Hf₂ON₂)",
- [94] 2013 International Centre for Diffraction Data, "00-050-1173 (Rhom Hf₇O₈N₄)",
- [95] 2012 International Centre for Diffraction Data, "33-1391 (Mono Ta₂O₅)",
- [96] 2012 International Centre for Diffraction Data, "33-1390 (Tri Ta₂O₅)",
- [97] 2012 International Centre for Diffraction Data, "21-1199 (Tetra Ta₂O₅)",
- [98] 2012 International Centre for Diffraction Data, "25-0922 (Ortho Ta₂O₅)",
- [99] 2012 International Centre for Diffraction Data, "18-1304 (Hex Ta₂O₅)",
- [100] E. Rudy, "Part V. Compendium of Phase Diagram Data," USAF; Wright-Patterson Air Force Base, Ohio, 1969.
- [101] B.C. Schulz, D. Butts, and G.B. Thompson, "Oxidation Behavior of Vacuum Plasma Sprayed Hafnium-Tantalum Nitrides," J. Am. Soc.(PENDING)

APPENDIX A

XRD LINE SCAN PROCEDURE

This procedure will walk the user through the procedure for creating an XRD line scan on the Bruker D8 Discovery General Area Diffraction Detector System (GADDS) using Cu-K α radiation at 45 keV and 40 mA as the source. The scans used in this dissertation were with 0.01 mm steps and 180 second dwell time.

Step 1: Attach sample to post seen in Figure A-1, with region of interest parallel to axis movement. Both x- and y- axis can be changed.

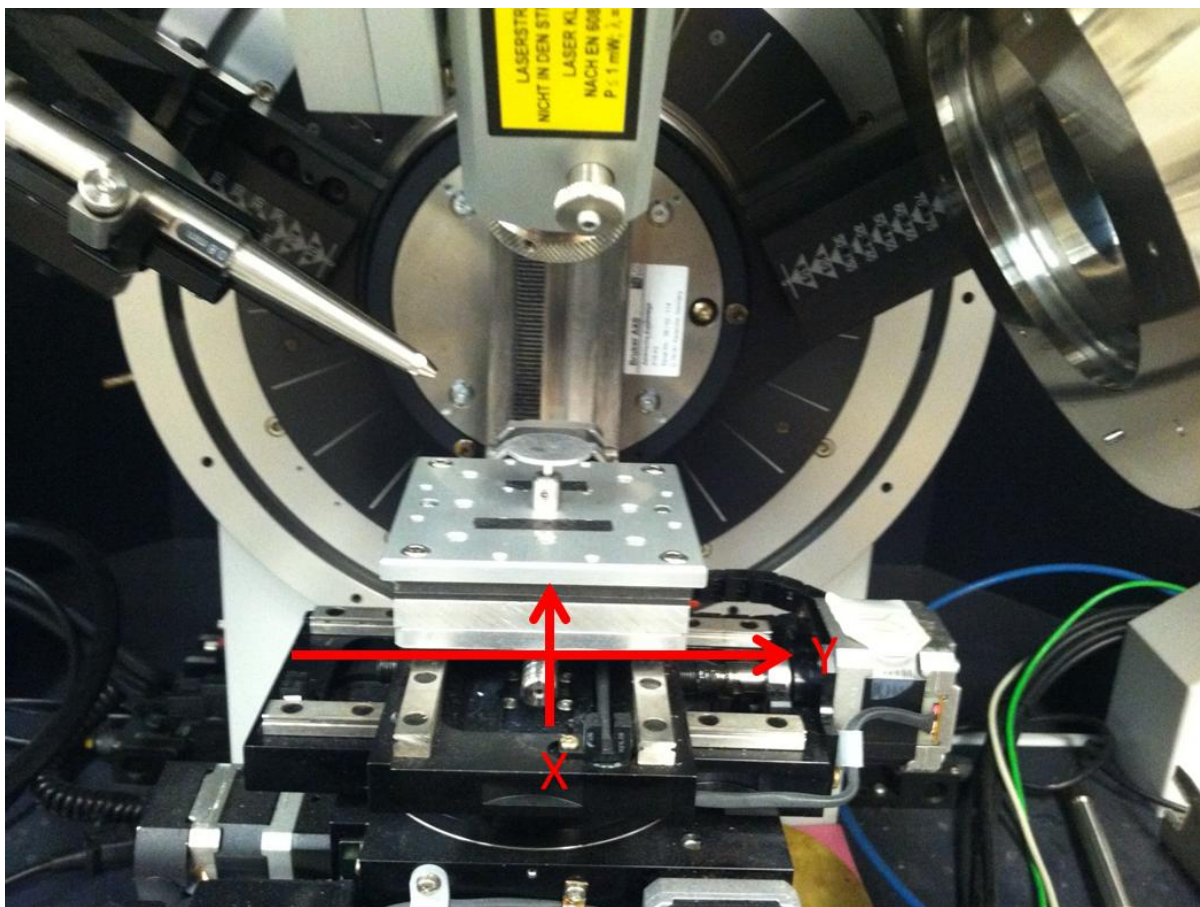


Figure A-1: Interior image of Bruker XRD system at the University of Alabama. XRD probe on left, optical camera in the middle, and XRD detector on right. The x- and y-axis' are labeled.

Step 2: Align the Z-axis with default procedure. With the GADDS software opened and project selected, open “Collect” and select “single run”, Figure A-2. Determine the dwell time, suggested 180 seconds/frame, and the frame width (step thickness of 0.01 mm). Based on these

parameters the # Frames will decide the overall length of the scan (50 frame 0.01 mm steps = 0.5 mm). Based on region of interest and desired line profile, select the Scan Axis with no Sample Oscillation.

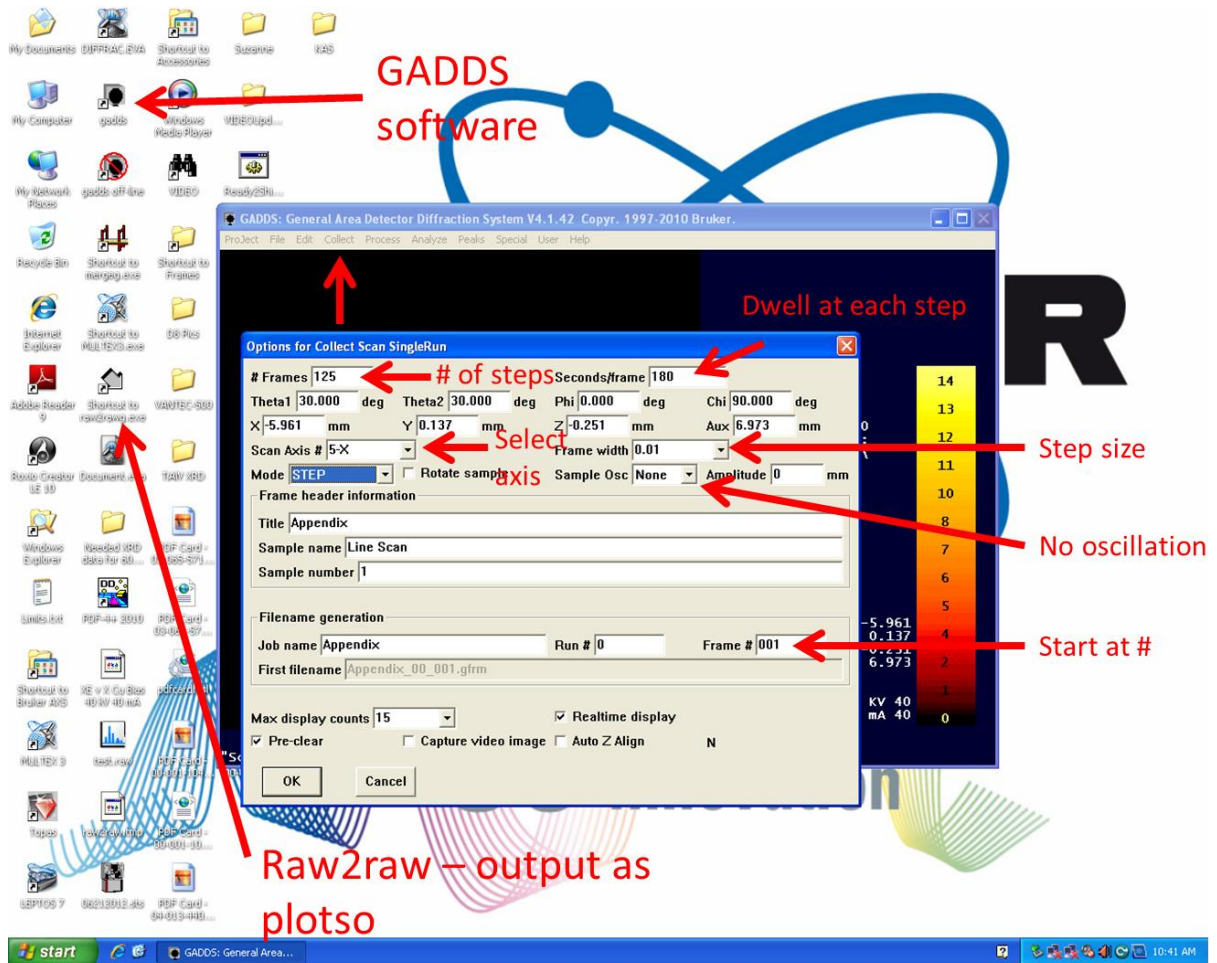


Figure A-2: GADDS line scan software parameters.

Step 3: Run the XRD scans and save them all with the exact same 2-theta values. This is extremely important for the 3D graphical section- SAVE ALL SCANS WITH SAME 2-THETA VALUES.

Step 4: Convert XRD data to “.out” files with Raw2Raw found in Figure A-2.

Step 5: Load XRD .out data in Excel and transfer over to Origin software.

Step 6: Plot the XRD data so that each frame is a different y-axis, demonstrated in Figure A-3. Once again, make sure that all the frames have the same x-axis 2-theta values. Select “plot” → “3D Wire/Bar/Symbol” → “Wire Surface”. Then make sure that the x-axis correlates to the 2-theta column and the remaining columns should be the y-axis data.

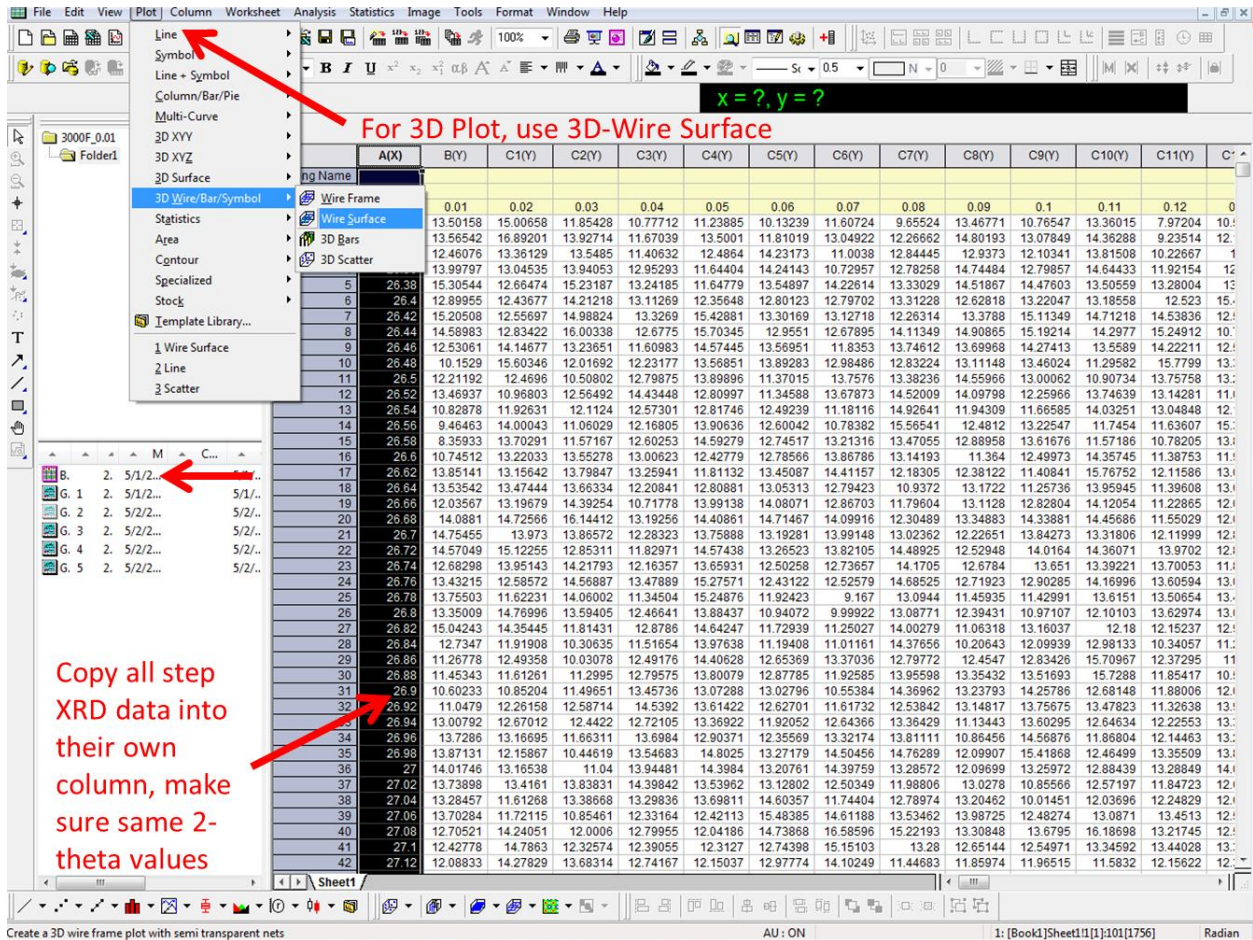


Figure A-3: Imported XRD files from Excel into Origins.

Step 7: Plot the 3D wire surface. Use the on-screen commands to adjust the view and its display rate, Figure A-5. Determine the frame-distance position based on the maxima, Figure A-4.

Step 8: Plot a 2D line scan of desired frame by selecting the 2-theta values and the specific column for the respective frame. Select “Plot” → “Line” → “Line”, Figure A-7. Find the peak 2-theta value with “Peak Analyzer”, Figure A-6 (“Analysis” → “Peaks and Baseline” → “Peak Analyzer” → “Open Dialog”). Gather these 2-theta values and record them in Excel.

Step 9: Calculate lattice parameters based on the D-spacing and *hkl* values. The Bragg’s equation and respective *a*- and *c/a* equations for hexagonal or cubic crystal structures are required too, Figure A-8.

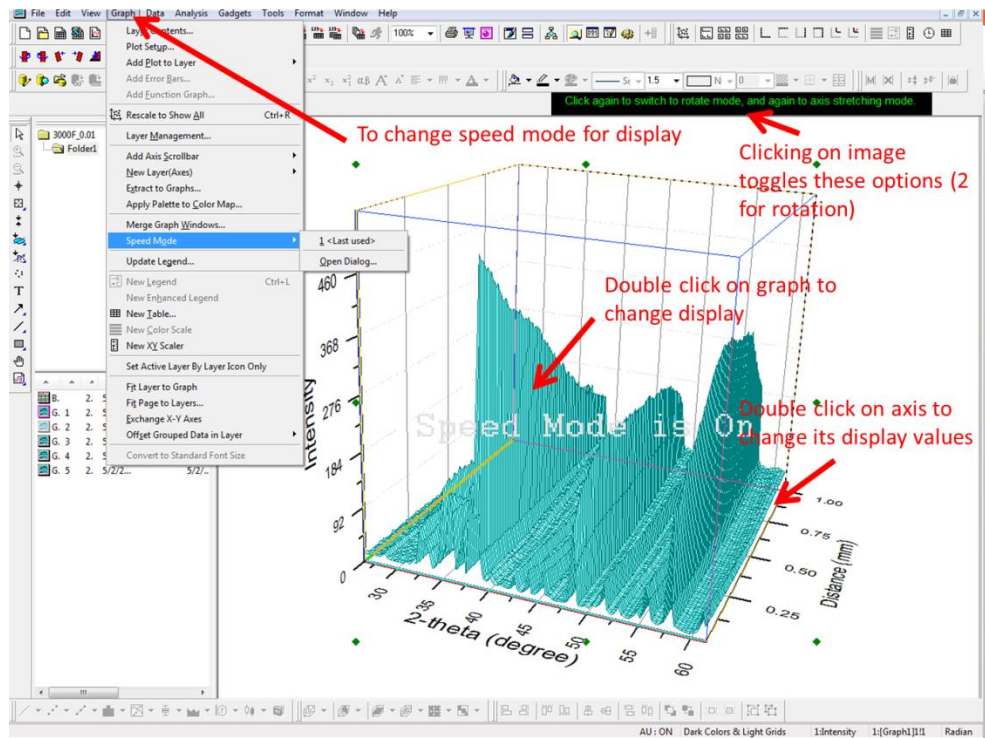


Figure A-5: Shows Origins on-screen commands. How to change the display speed, rotation and image adjustment, as well as axis parameter changes are described above.

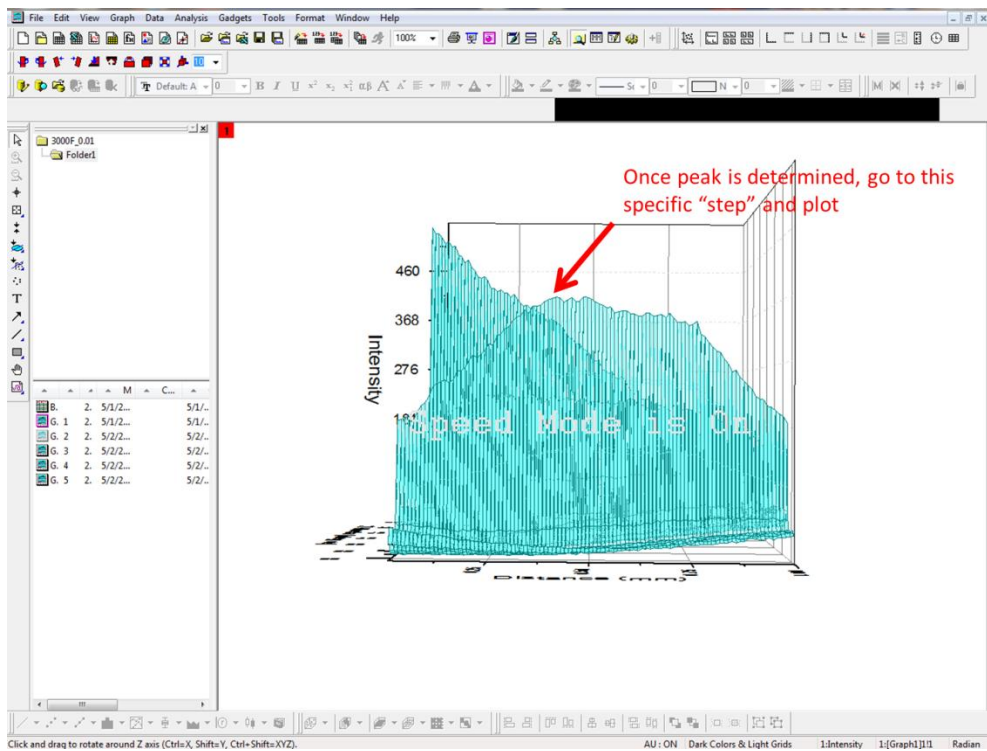


Figure A-4: Orientate display to determine peak maxima and their frame-distance positioning.

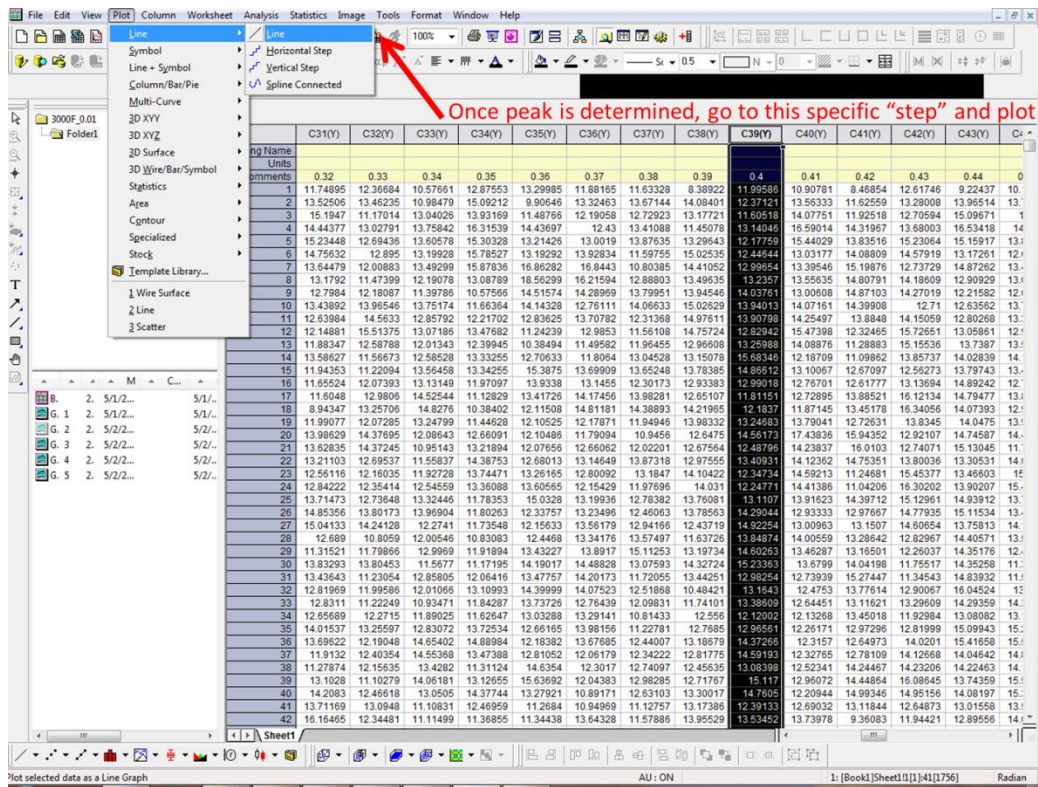


Figure A-7: Screen shot demonstrating the creation of a 2D line scan plot.

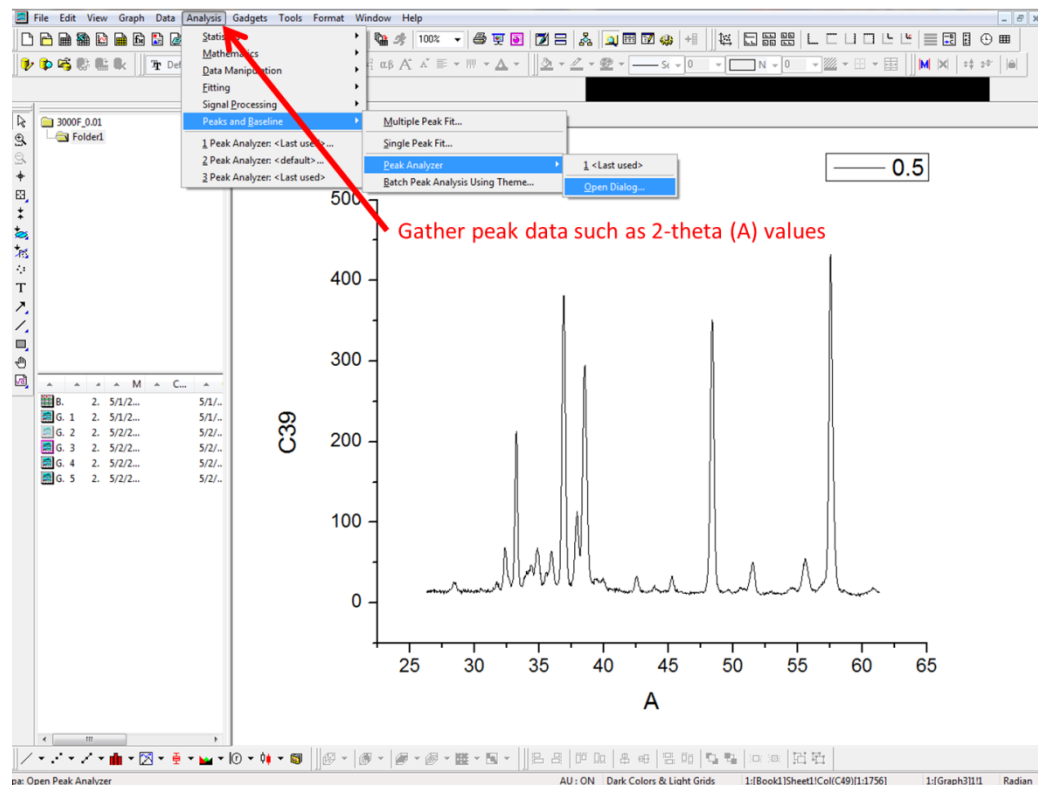


Figure A-6: Demonstration of peak analysis to determine the 2-theta values of frame-distance position.

Hf3N2	Normal							
2Theta	Radians	Dspacing	h	k	l	a	c/a	c
35.57334	0.620872	2.521591	1	0	4		24.59168	7.702768
35.9688	0.627774	2.494769	1	0	4		22.90422	7.156582
35.61987	0.621684	2.518404	1	0	4		24.12195	7.537071
35.61987	0.621684	2.518404	1	0	4		24.12195	7.537071
57.70343	1.007115	1.596288	1	1	0	3.192576		0
57.54835	1.004408	1.600221	1	1	0	3.200441		0
57.54835	1.004408	1.600221	1	1	0	3.200441		0
57.54835	1.004408	1.600221	1	1	0	3.200441		0

↑
2-theta
value from
single step
(C39) XRD
peak data.

↑
Bragg's
Law

$$a = \frac{\lambda \sqrt{h^2 + hk + k^2}}{\sqrt{3} \sin 2\theta}$$

$$\frac{c}{a} = \frac{(a * l)}{\sqrt{\frac{4a^2 \sin^2 2\theta}{\lambda^2 - \frac{4}{3}(h^2 + hk + k^2)}}}$$

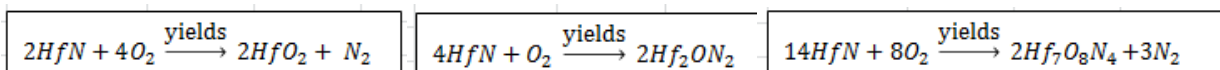
Figure A-8: Example Excel sheet with appropriate equations in determining *a*- and *c/a* lattice values in a hexagonal crystal system.

APPENDIX B

DENSITY FUNCTIONAL THEORY EXAMPLE REACTIONS FOR THE HAFNIUM AND TANTALUM NITRIDE SYSTEMS

Proposed reactions for a future DFT modeling study of the Hf-N and Ta-N phases along with their possible oxides. I envisioned that the starting reactions would be based on the given crystallographic information; however, the lattice parameters were subject to change. In the case of the rhombohedral phases, the exact positioning of the nitrogen atoms was unknown, so 2 cases are presented: (1) random throughout the 6c-3a-3b Wyckoff placements or (2) filled 6c-3a placements with 3b empty. In addition, the rhombohedral phases go an additional step beyond the proposed oxygen occupancy of the vacant sites; they continue on with oxygen-nitrogen substitution. I hypothesized that the rhombohedral phases would be energetically favorable for the first 3 oxygen placements in Hf_3N_2 (completely filled to form Hf_3ON_2 for instance) compared to the transformation of Hf_3N_2 to hafnia. However, I believe that the further transformation from Hf_3ON_2 to hafnia would provide a steeper energy curve than the base Hf_3N_2 to hafnia. Thus the system would sacrifice some oxidation for a higher resistance to the hafnia transformation.

HfN



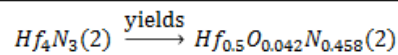
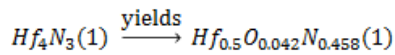
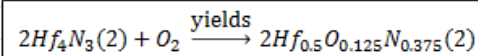
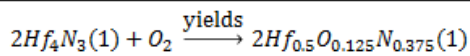
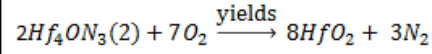
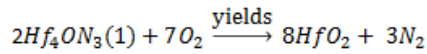
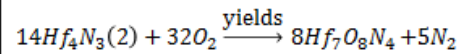
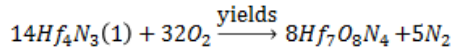
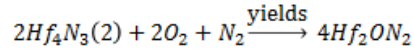
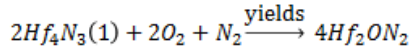
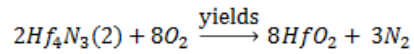
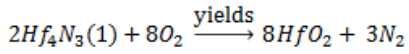
HfN						
Crystallography	Fm-3m (225)					
Lattice a (nm)	0.4454					
Lattice b (nm)						
Lattice c (nm)						
alpha (degree)	90					
beta (degree)	90					
gamma (degree)	90					
Element	Occupancy	Wyckoff	x	y	z	
Hf	1		0	0	0	
N	1		0.5	0.5	0.5	

HfO2						
Crystallography	P21/c (14)					
Lattice a (nm)	0.52851					
Lattice b (nm)	0.51819					
Lattice c (nm)	0.51157					
alpha (degree)	90					
beta (degree)	99.259					
gamma (degree)	90					
Element	Occupancy	Wyckoff	x	y	z	
Hf	1		0.2759	0.0412	0.2078	
O(1)	1		0.073	0.346	0.332	
O(2)	1		0.446	0.748	0.488	

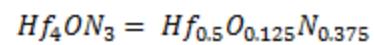
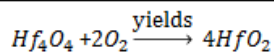
Hf2ON2						
Crystallography	Ia-3 (206)					
Lattice a (nm)	1.0063					
Lattice b (nm)						
Lattice c (nm)						
alpha (degree)	90					
beta (degree)	90					
gamma (degree)	90					
Element	Occupancy	Wyckoff	x	y	z	
Hf(1)	1	24d	0.96739	0	0.25	
Hf(2)	1	8b	0.25	0.25	0.25	
O	0.333	48e	0.39075	0.15189	0.38012	
N	0.67	48e	0.39075	0.15189	0.38012	

Hf7O8N4						
Crystallography	R-3 (148)					
Lattice a (nm)	0.94851					
Lattice b (nm)						
Lattice c (nm)	0.8787					
alpha (degree)	90					
beta (degree)	90					
gamma (degree)	120					
Element	Occupancy	Wyckoff	x	y	z	
Hf(1)	1	3a	0	0	0	
Hf(2)	1	18f	0.2903	0.4096	0.0161	
O(1)	0.67	18f	0.2997	0.4536	-0.2308	
N(1)	0.33	18f	0.2997	0.4536	-0.2308	
O(2)	0.67	18f	0.3016	0.4549	0.2787	
N(2)	0.33	18f	0.3016	0.4549	0.2787	

Hf4N3



Keep substituting in oxygen for nitrogen until reach Hf4O4



Hf4N3 (1)						
Crystallography	R-3m (166)					
Lattice a (nm)	0.3214					
Lattice b (nm)						
Lattice c (nm)	3.112					
alpha (degree)	90					
beta (degree)	90					
gamma (degree)	120					
Element	Occupancy	Wyckoff	x	y	z	
Hf(1)	1 (6/6)	6c	0	0	0.125	
Hf(2)	1 (6/6)	6c	0	0	0.292	
N(1)	0.75 (5/6)	6c	0	0	0.417	
N(2)	0.75 (2/3)	3a	0	0	0	
N(3)	0.75 (2/3)	3b	0	0	0.5	

Hf4N3 (2)						
Crystallography	R-3m (166)					
Lattice a (nm)	0.3214					
Lattice b (nm)						
Lattice c (nm)	3.112					
alpha (degree)	90					
beta (degree)	90					
gamma (degree)	120					
Element	Occupancy	Wyckoff	x	y	z	
Hf(1)	1 (6/6)	6c	0	0	0.125	
Hf(2)	1 (6/6)	6c	0	0	0.292	
N(1)	1 (6/6)	6c	0	0	0.417	
N(2)	1 (3/3)	3a	0	0	0	
N(3)	0 (0/3)	3b	0	0	0.5	

HfO2					
Crystallography	P21/c (14)				
Lattice a (nm)	0.52851				
Lattice b (nm)	0.51819				
Lattice c (nm)	0.51157				
alpha (degree)	90				
beta (degree)	99.259				
gamma (degree)	90				
Element	Occupancy	Wyckoff	x	y	z
Hf	1		0.2759	0.0412	0.2078
O(1)	1		0.073	0.346	0.332
O(2)	1		0.446	0.748	0.488

Hf2ON2					
Crystallography	Ia-3 (206)				
Lattice a (nm)	1.0063				
Lattice b (nm)					
Lattice c (nm)					
alpha (degree)	90				
beta (degree)	90				
gamma (degree)	90				
Element	Occupancy	Wyckoff	x	y	z
Hf(1)	1	24d	0.96739	0	0.25
Hf(2)	1	8b	0.25	0.25	0.25
O	0.333	48e	0.39075	0.15189	0.38012
N	0.67	48e	0.39075	0.15189	0.38012

Hf7O8N4					
Crystallography	R-3 (148)				
Lattice a (nm)	0.94851				
Lattice b (nm)					
Lattice c (nm)	0.8787				
alpha (degree)	90				
beta (degree)	90				
gamma (degree)	120				
Element	Occupancy	Wyckoff	x	y	z
Hf(1)	1	3a	0	0	0
Hf(2)	1	18f	0.2903	0.4096	0.0161
O(1)	0.67	18f	0.2997	0.4536	-0.2308
N(1)	0.33	18f	0.2997	0.4536	-0.2308
O(2)	0.67	18f	0.3016	0.4549	0.2787
N(2)	0.33	18f	0.3016	0.4549	0.2787

Hf0.5O0.042N0.458 (1)					
Crystallography	R-3m (166)				
Lattice a (nm)	0.3214				
Lattice b (nm)					
Lattice c (nm)	3.112				
alpha (degree)	90				
beta (degree)	90				
gamma (degree)	120				
Element	Occupancy	Wyckoff	x	y	z
Hf(1)	(6/6)	6c	0	0	0.125
Hf(2)	(6/6)	6c	0	0	0.292
N(1)	(5/6)	6c	0	0	0.417
O(1)	(1/6)	6c	0	0	0.417
N(2)	(2/3)	3a	0	0	0
O(2)	(0/3)	3a	0	0	0
N(3)	(2/3)	3b	0	0	0.5
O(3)	(0/3)	3b	0	0	0.5

Hf0.5O0.042N0.458 (2)					
Crystallography	R-3m (166)				
Lattice a (nm)	0.3214				
Lattice b (nm)					
Lattice c (nm)	3.112				
alpha (degree)	90				
beta (degree)	90				
gamma (degree)	120				
Element	Occupancy	Wyckoff	x	y	z
Hf(1)	(6/6)	6c	0	0	0.125
Hf(2)	(6/6)	6c	0	0	0.292
N(1)	(6/6)	6c	0	0	0.417
O(1)	(0/6)	6c	0	0	0.417
N(2)	(3/3)	3a	0	0	0
O(2)	(0/3)	3a	0	0	0
N(3)	(0/3)	3b	0	0	0.5
O(3)	(1/3)	3b	0	0	0.5

Hf0.500.083N0.417 (1)					
Crystallography	R-3m (166)				
Lattice a (nm)	0.3214				
Lattice b (nm)					
Lattice c (nm)	3.112				
alpha (degree)	90				
beta (degree)	90				
gamma (degree)	120				
Element	Occupancy	Wyckoff	x	y	z
Hf(1)	(6/6)	6c	0	0	0.125
Hf(2)	(6/6)	6c	0	0	0.292
N(1)	(5/6)	6c	0	0	0.417
O(1)	(1/6)	6c	0	0	0.417
N(2)	(2/3)	3a	0	0	0
O(2)	(1/3)	3a	0	0	0
N(3)	(2/3)	3b	0	0	0.5
O(3)	(0/3)	3b	0	0	0.5

Hf0.500.083N0.417 (2)					
Crystallography	R-3m (166)				
Lattice a (nm)	0.3214				
Lattice b (nm)					
Lattice c (nm)	3.112				
alpha (degree)	90				
beta (degree)	90				
gamma (degree)	120				
Element	Occupancy	Wyckoff	x	y	z
Hf(1)	(6/6)	6c	0	0	0.125
Hf(2)	(6/6)	6c	0	0	0.292
N(1)	(6/6)	6c	0	0	0.417
O(1)	(0/6)	6c	0	0	0.417
N(2)	(3/3)	3a	0	0	0
O(2)	(0/3)	3a	0	0	0
N(3)	(0/3)	3b	0	0	0.5
O(3)	(2/3)	3b	0	0	0.5

Hf0.500.125N0.375 (1)					
Crystallography	R-3m (166)				
Lattice a (nm)	0.3214				
Lattice b (nm)					
Lattice c (nm)	3.112				
alpha (degree)	90				
beta (degree)	90				
gamma (degree)	120				
$Hf_4ON_3 = Hf_{0.5}O_{0.125}N_{0.375}$					
Element	Occupancy	Wyckoff	x	y	z
Hf(1)	(6/6)	6c	0	0	0.125
Hf(2)	(6/6)	6c	0	0	0.292
N(1)	(5/6)	6c	0	0	0.417
O(1)	(1/6)	6c	0	0	0.417
N(2)	(2/3)	3a	0	0	0
O(2)	(1/3)	3a	0	0	0
N(3)	(2/3)	3b	0	0	0.5
O(3)	(1/3)	3b	0	0	0.5

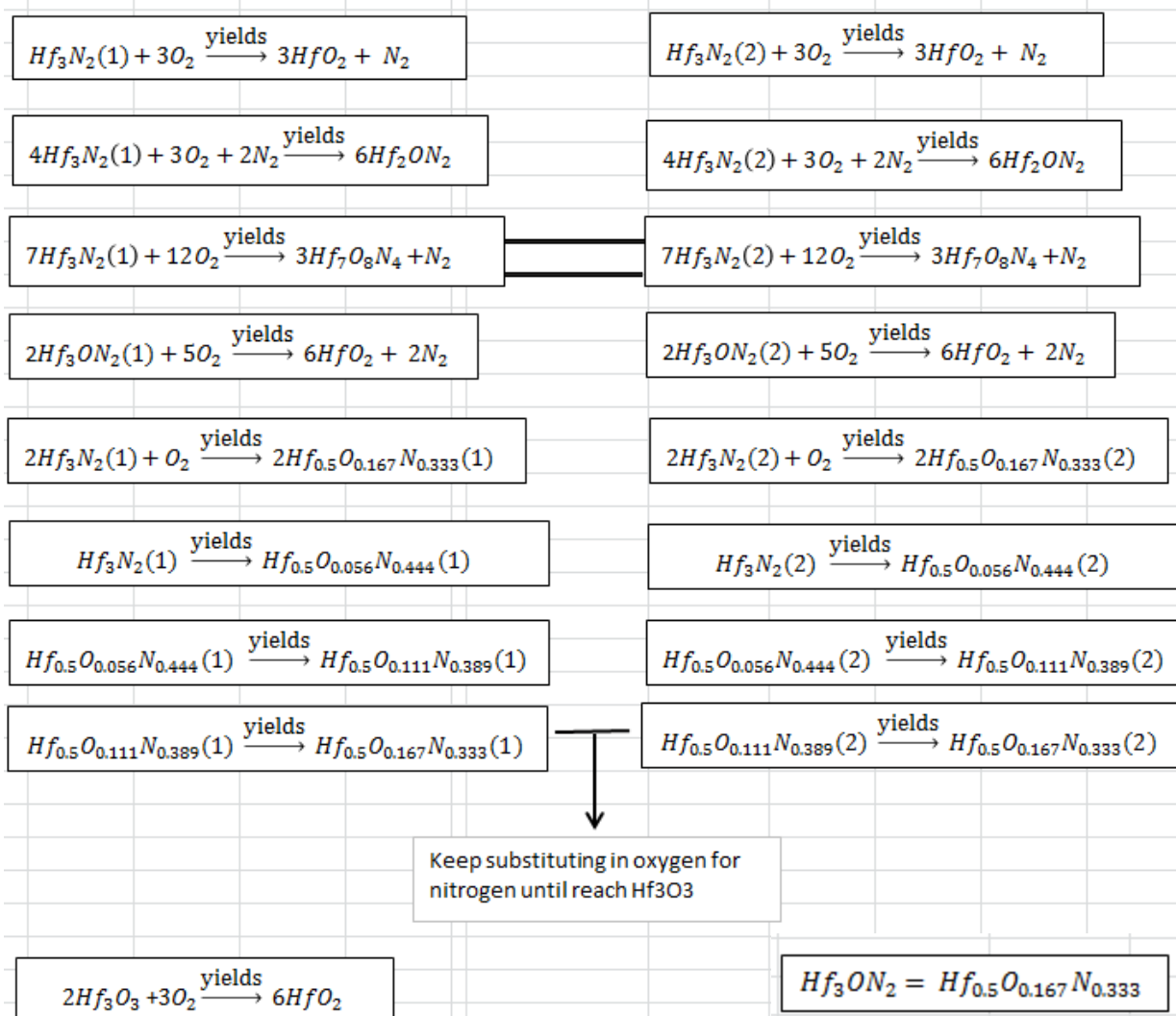
Hf0.500.125N0.375 (2)					
Crystallography	R-3m (166)				
Lattice a (nm)	0.3214				
Lattice b (nm)					
Lattice c (nm)	3.112				
alpha (degree)	90				
beta (degree)	90				
gamma (degree)	120				
Element	Occupancy	Wyckoff	x	y	z
Hf(1)	(6/6)	6c	0	0	0.125
Hf(2)	(6/6)	6c	0	0	0.292
N(1)	(6/6)	6c	0	0	0.417
O(1)	(0/6)	6c	0	0	0.417
N(2)	(3/3)	3a	0	0	0
O(2)	(0/3)	3a	0	0	0
N(3)	(0/3)	3b	0	0	0.5
O(3)	(3/3)	3b	0	0	0.5

Hf0.500.167N0.333 (1)					
Crystallography	R-3m (166)				
Lattice a (nm)	0.3214				
Lattice b (nm)					
Lattice c (nm)	3.112				
alpha (degree)	90				
beta (degree)	90				
gamma (degree)	120				
Element	Occupancy	Wyckoff	x	y	z
Hf(1)	(6/6)	6c	0	0	0.125
Hf(2)	(6/6)	6c	0	0	0.292
N(1)	(4/6)	6c	0	0	0.417
O(1)	(2/6)	6c	0	0	0.417
N(2)	(2/3)	3a	0	0	0
O(2)	(1/3)	3a	0	0	0
N(3)	(2/3)	3b	0	0	0.5
O(3)	(1/3)	3b	0	0	0.5

Hf0.500.167N0.333 (2)					
Crystallography	R-3m (166)				
Lattice a (nm)	0.3214				
Lattice b (nm)					
Lattice c (nm)	3.112				
alpha (degree)	90				
beta (degree)	90				
gamma (degree)	120				
Element	Occupancy	Wyckoff	x	y	z
Hf(1)	(6/6)	6c	0	0	0.125
Hf(2)	(6/6)	6c	0	0	0.292
N(1)	(5/6)	6c	0	0	0.417
O(1)	(1/6)	6c	0	0	0.417
N(2)	(3/3)	3a	0	0	0
O(2)	(0/3)	3a	0	0	0
N(3)	(0/3)	3b	0	0	0.5
O(3)	(3/3)	3b	0	0	0.5

Hf4O4					
Crystallography	R-3m (166)				
Lattice a (nm)	0.3214				
Lattice b (nm)					
Lattice c (nm)	3.112				
alpha (degree)	90				
beta (degree)	90				
gamma (degree)	120				
Element	Occupancy	Wyckoff	x	y	z
Hf(1)	(6/6)	6c	0	0	0.125
Hf(2)	(6/6)	6c	0	0	0.292
N(1)	(0/6)	6c	0	0	0.417
O(1)	(6/6)	6c	0	0	0.417
N(2)	(0/3)	3a	0	0	0
O(2)	(3/3)	3a	0	0	0
N(3)	(0/3)	3b	0	0	0.5
O(3)	(3/3)	3b	0	0	0.5

Hf3N2



Hf3N2 (1)					
Crystallography	R-3m (166)				
Lattice a (nm)	0.3206				
Lattice b (nm)					
Lattice c (nm)	2.326				
alpha (degree)	90				
beta (degree)	90				
gamma (degree)	120				
Element	Occupancy	Wyckoff	x	y	z
Hf(1)	1 (6/6)	6c	0	0	0.222
Hf(2)	1 (3/3)	3a	0	0	0
N(1)	0.67 (4/6)	6c	0	0	0.389
N(2)	0.67 (2/3)	3b	0	0	0.5

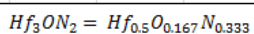
Hf3N2 (2)					
Crystallography	R-3m (166)				
Lattice a (nm)	0.3206				
Lattice b (nm)					
Lattice c (nm)	2.326				
alpha (degree)	90				
beta (degree)	90				
gamma (degree)	120				
Element	Occupancy	Wyckoff	x	y	z
Hf(1)	1 (6/6)	6c	0	0	0.222
Hf(2)	1 (3/3)	3a	0	0	0
N(1)	1 (6/6)	6c	0	0	0.389
N(2)	0 (0/3)	3b	0	0	0.5

HfO2					
Crystallography	P21/c (14)				
Lattice a (nm)	0.52851				
Lattice b (nm)	0.51819				
Lattice c (nm)	0.51157				
alpha (degree)	90				
beta (degree)	99.259				
gamma (degree)	90				
Element	Occupancy	Wyckoff	x	y	z
Hf	1		0.2759	0.0412	0.2078
O(1)	1		0.073	0.346	0.332
O(2)	1		0.446	0.748	0.488

Hf2ON2					
Crystallography	Ia-3 (206)				
Lattice a (nm)	1.0063				
Lattice b (nm)					
Lattice c (nm)					
alpha (degree)	90				
beta (degree)	90				
gamma (degree)	90				
Element	Occupancy	Wyckoff	x	y	z
Hf(1)	1	24d	0.96739	0	0.25
Hf(2)	1	8b	0.25	0.25	0.25
O	0.333	48e	0.39075	0.15189	0.38012
N	0.67	48e	0.39075	0.15189	0.38012

Hf7O8N4					
Crystallography	R-3 (148)				
Lattice a (nm)	0.94851				
Lattice b (nm)					
Lattice c (nm)	0.8787				
alpha (degree)	90				
beta (degree)	90				
gamma (degree)	120				
Element	Occupancy	Wyckoff	x	y	z
Hf(1)	1	3a	0	0	0
Hf(2)	1	18f	0.2903	0.4096	0.0161
O(1)	0.67	18f	0.2997	0.4536	-0.2308
N(1)	0.33	18f	0.2997	0.4536	-0.2308
O(2)	0.67	18f	0.3016	0.4549	0.2787
N(2)	0.33	18f	0.3016	0.4549	0.2787

Hf0.5O0.056N0.444 (1)						Hf0.5O0.056N0.444 (2)					
Crystallography	R-3m (166)					Crystallography	R-3m (166)				
Lattice a (nm)	0.3206					Lattice a (nm)	0.3206				
Lattice b (nm)						Lattice b (nm)					
Lattice c (nm)	2.326					Lattice c (nm)	2.326				
alpha (degree)	90					alpha (degree)	90				
beta (degree)	90					beta (degree)	90				
gamma (degree)	120					gamma (degree)	120				
Element	Occupancy	Wyckoff	x	y	z	Element	Occupancy	Wyckoff	x	y	z
Hf(1)	(6/6)	6c	0	0	0.222	Hf(1)	(6/6)	6c	0	0	0.222
Hf(2)	(3/3)	3a	0	0	0	Hf(2)	(3/3)	3a	0	0	0
N(1)	(4/6)	6c	0	0	0.389	N(1)	(6/6)	6c	0	0	0.389
O(1)	(1/6)	6c	0	0	0.389	O(1)	(0/6)	6c	0	0	0.389
N(2)	(2/3)	3b	0	0	0.5	N(2)	(0/3)	3b	0	0	0.5
O(2)	(0/3)	3b	0	0	0.5	O(2)	(1/3)	3b	0	0	0.5
Hf0.5O0.111N0.389 (1)						Hf0.5O0.111N0.389 (2)					
Crystallography	R-3m (166)					Crystallography	R-3m (166)				
Lattice a (nm)	0.3206					Lattice a (nm)	0.3206				
Lattice b (nm)						Lattice b (nm)					
Lattice c (nm)	2.326					Lattice c (nm)	2.326				
alpha (degree)	90					alpha (degree)	90				
beta (degree)	90					beta (degree)	90				
gamma (degree)	120					gamma (degree)	120				
Element	Occupancy	Wyckoff	x	y	z	Element	Occupancy	Wyckoff	x	y	z
Hf(1)	(6/6)	6c	0	0	0.222	Hf(1)	(6/6)	6c	0	0	0.222
Hf(2)	(3/3)	3a	0	0	0	Hf(2)	(3/3)	3a	0	0	0
N(1)	(4/6)	6c	0	0	0.389	N(1)	(6/6)	6c	0	0	0.389
O(1)	(2/6)	6c	0	0	0.389	O(1)	(0/6)	6c	0	0	0.389
N(2)	(2/3)	3b	0	0	0.5	N(2)	(0/3)	3b	0	0	0.5
O(2)	(0/3)	3b	0	0	0.5	O(2)	(2/3)	3b	0	0	0.5
Hf0.5O0.167N0.333 (1)						Hf0.5O0.167N0.333 (2)					
Crystallography	R-3m (166)					Crystallography	R-3m (166)				
Lattice a (nm)	0.3206					Lattice a (nm)	0.3206				
Lattice b (nm)						Lattice b (nm)					
Lattice c (nm)	2.326					Lattice c (nm)	2.326				
alpha (degree)	90					alpha (degree)	90				
beta (degree)	90					beta (degree)	90				
gamma (degree)	120					gamma (degree)	120				
Element	Occupancy	Wyckoff	x	y	z	Element	Occupancy	Wyckoff	x	y	z
Hf(1)	(6/6)	6c	0	0	0.222	Hf(1)	(6/6)	6c	0	0	0.222
Hf(2)	(3/3)	3a	0	0	0	Hf(2)	(3/3)	3a	0	0	0
N(1)	(4/6)	6c	0	0	0.389	N(1)	(6/6)	6c	0	0	0.389
O(1)	(2/6)	6c	0	0	0.389	O(1)	(0/6)	6c	0	0	0.389
N(2)	(2/3)	3b	0	0	0.5	N(2)	(0/3)	3b	0	0	0.5
O(2)	(1/3)	3b	0	0	0.5	O(2)	(3/3)	3b	0	0	0.5

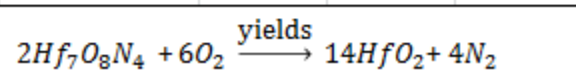
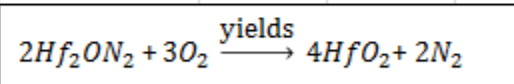
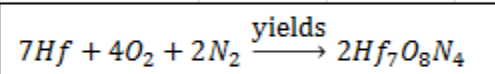
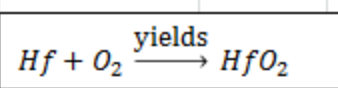


Hf0.5O0.222N0.278 (1)					
Crystallography	R-3m (166)				
Lattice a (nm)	0.3206				
Lattice b (nm)					
Lattice c (nm)	2.326				
alpha (degree)	90				
beta (degree)	90				
gamma (degree)	120				
Element	Occupancy	Wyckoff	x	y	z
Hf(1)	(6/6)	6c	0	0	0.222
Hf(2)	(3/3)	3a	0	0	0
N(1)	(3/6)	6c	0	0	0.389
O(1)	(3/6)	6c	0	0	0.389
N(2)	(2/3)	3b	0	0	0.5
O(2)	(1/3)	3b	0	0	0.5

Hf0.5O0.222N0.278 (2)					
Crystallography	R-3m (166)				
Lattice a (nm)	0.3206				
Lattice b (nm)					
Lattice c (nm)	2.326				
alpha (degree)	90				
beta (degree)	90				
gamma (degree)	120				
Element	Occupancy	Wyckoff	x	y	z
Hf(1)	(6/6)	6c	0	0	0.222
Hf(2)	(3/3)	3a	0	0	0
N(1)	(5/6)	6c	0	0	0.389
O(1)	(1/6)	6c	0	0	0.389
N(2)	(0/3)	3b	0	0	0.5
O(2)	(3/3)	3b	0	0	0.5

Hf3O3					
Crystallography	R-3m (166)				
Lattice a (nm)	0.3206				
Lattice b (nm)					
Lattice c (nm)	2.326				
alpha (degree)	90				
beta (degree)	90				
gamma (degree)	120				
Element	Occupancy	Wyckoff	x	y	z
Hf(1)	(6/6)	6c	0	0	0.222
Hf(2)	(3/3)	3a	0	0	0
N(1)	(0/6)	6c	0	0	0.389
O(1)	(6/6)	6c	0	0	0.389
N(2)	(0/3)	3b	0	0	0.5
O(2)	(3/3)	3b	0	0	0.5

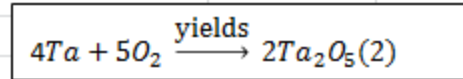
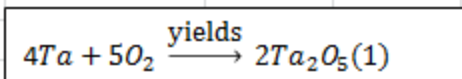
Hf



Hf					
Crystallography	P63/mmc (194)				
Lattice a (nm)	0.31967				
Lattice b (nm)					
Lattice c (nm)	0.50578				
alpha (degree)	90				
beta (degree)	90				
gamma (degree)	120				
Element	Occupancy	Wyckoff	x	y	z
Hf	1		0.333	0.667	0.25

HfO2					
Crystallography	P21/c (14)				
Lattice a (nm)	0.52851				
Lattice b (nm)	0.51819				
Lattice c (nm)	0.51157				
alpha (degree)	90				
beta (degree)	99.259				
gamma (degree)	90				
Element	Occupancy	Wyckoff	x	y	z
Hf	1		0.2759	0.0412	0.2078
O(1)	1		0.073	0.346	0.332
O(2)	1		0.446	0.748	0.488

Ta

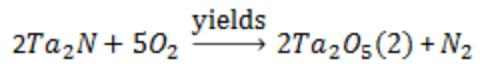


Ta					
Crystallography	Im-3m (229)				
Lattice a (nm)	0.3306				
Lattice b (nm)					
Lattice c (nm)					
alpha (degree)	90				
beta (degree)	90				
gamma (degree)	90				
Element	Occupancy	Wyckoff	x	y	z
Ta	1				

Ta2O5 (1)					
Crystallography	P (2)				
Lattice a (nm)	0.3801				
Lattice b (nm)	0.3785				
Lattice c (nm)	3.574				
alpha (degree)	90.91				
beta (degree)	90.19				
gamma (degree)	89.99				
Element	Occupancy	Wyckoff	x	y	z
Ta	1		0.607	0.1395	0.9628
O(1)	1		0.44239	0.22834	0.66245
O(2)	1		0.18239	0.3085	1.19424

Ta2O5 (2)					
Crystallography	Pmm2 (25)				
Lattice a (nm)	0.6198				
Lattice b (nm)	4.029				
Lattice c (nm)	0.3888				
alpha (degree)	90				
beta (degree)					
gamma (degree)					
Element	Occupancy	Wyckoff	x	y	z
Ta	1		0.1289	0.0972	0.8628
O(1)	1		0.0095	0.1491	0.1835
O(2)	1		0.2314	0.111	0.5366

Ta₂N

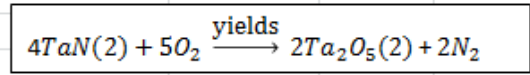
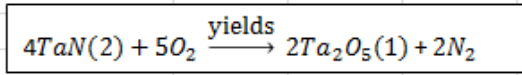
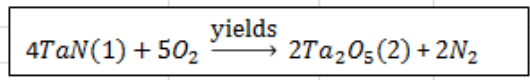
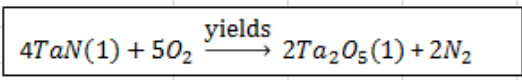


Ta ₂ N					
Crystallography	P-3m1 (164)				
Lattice a (nm)	0.30476				
Lattice b (nm)					
Lattice c (nm)	0.49187				
alpha (degree)	90				
beta (degree)	90				
gamma (degree)	120				
Element	Occupancy	Wyckoff	x	y	z
Ta	1				

Ta ₂ O ₅ (1)					
Crystallography	P (2)				
Lattice a (nm)	0.3801				
Lattice b (nm)	0.3785				
Lattice c (nm)	3.574				
alpha (degree)	90.91				
beta (degree)	90.19				
gamma (degree)	89.99				
Element	Occupancy	Wyckoff	x	y	z
Ta	1		0.607	0.1395	0.9628
O(1)	1		0.44239	0.22834	0.66245
O(2)	1		0.18239	0.3085	1.19424

Ta ₂ O ₅ (2)					
Crystallography	Pmm2 (25)				
Lattice a (nm)	0.6198				
Lattice b (nm)	4.029				
Lattice c (nm)	0.3888				
alpha (degree)	90				
beta (degree)					
gamma (degree)					
Element	Occupancy	Wyckoff	x	y	z
Ta	1		0.1289	0.0972	0.8628
O(1)	1		0.0095	0.1491	0.1835
O(2)	1		0.2314	0.111	0.5366

TaN



TaN (1)					
Crystallography	P6/mmm (191)				
Lattice a (nm)	0.51918				
Lattice b (nm)					
Lattice c (nm)	0.29081				
alpha (degree)	90				
beta (degree)	90				
gamma (degree)	120				
Element	Occupancy	Wyckoff	x	y	z
Ta	1				

TaN (2)					
Crystallography	Fm-3m (225)				
Lattice a (nm)	0.434				
Lattice b (nm)					
Lattice c (nm)					
alpha (degree)	90				
beta (degree)	90				
gamma (degree)	90				
Element	Occupancy	Wyckoff	x	y	z
Ta	1				

Ta2O5 (1)					
Crystallography	P (2)				
Lattice a (nm)	0.3801				
Lattice b (nm)	0.3785				
Lattice c (nm)	3.574				
alpha (degree)	90.91				
beta (degree)	90.19				
gamma (degree)	89.99				
Element	Occupancy	Wyckoff	x	y	z
Ta	1		0.607	0.1395	0.9628
O(1)	1		0.44239	0.22834	0.66245
O(2)	1		0.18239	0.3085	1.19424

Ta2O5 (2)					
Crystallography	Pmm2 (25)				
Lattice a (nm)	0.6198				
Lattice b (nm)	4.029				
Lattice c (nm)	0.3888				
alpha (degree)	90				
beta (degree)					
gamma (degree)					
Element	Occupancy	Wyckoff	x	y	z
Ta	1		0.1289	0.0972	0.8628
O(1)	1		0.0095	0.1491	0.1835
O(2)	1		0.2314	0.111	0.5366

APPENDIX C

INITIAL WORK ON HAFNIUM-TANTALUM-NITRIDE CHARACTERIZATION OF MECHANICAL BEHAVIOR

An additional 80HfN-20TaN, initial blend, specimen was processed with VPS and followed with sinter/HIP. This specimen had mechanical behavior specimens made that were tested at 3000°F (approximately 1650°C). These mechanical specimens were tested in a high-temperature flexural furnace at Southern Research Institute (Birmingham, Al). A bar of approximately 2 mm x 4 mm was slowly heat ramped up to 1650°C over approximately 30 min in a helium purged atmosphere. The specimen was held at temperature for 5 min where it was mechanically tested and cooled then down. At approximately 540°C the furnace was opened to air as it cooled down to room temperature. The specimen was primarily tested for mechanical behavior thus the actual oxidation and heat ramps were not well recorded. However, it was noted that this specimen also developed a black scale post-testing; the typical specimen develops a white scale after this procedure.

Characterization included XRD, SEM, TEM, as well as atom-probe tomography. The EBSD demonstrates, Figure C-9, that the oxy-nitride phases were clearly identified as separate phases from the nitrides. In addition it was shown that these oxy-nitrides had significant volume content compared to the nitrides and hafnia, Table C-1. HAADF STEM imaging of this oxy-nitride scale region showed that heavy contrast along grain boundaries and lath-like microstructures, Figure C-10. In addition, atom probe tomography was attempted on this specimen. Multiple tips were made from the bulk region as well as from the oxide and oxy-nitride/oxide interface. The oxide atom probe tips were unsuccessful and fractured; however, the oxy-nitride/oxide interface as well as the bulk nitride atom probe tips had successful runs, Figure C-11. Another XRD line scan was conducted on this specimen between the bulk and oxide scale. It was found that not only did the rhombohedral nitride phases, Hf_3N_2 and Hf_4N_3 , phases have peak shifts, but they had significant peak splits, Figure C-12. These peaks were only able to be identified as their base rhombohedral phases. It is believed that the new rhombohedral peaks are the distinct different oxy-nitride Hf_3ON_2 and Hf_4ON_3 phases, Table C-2.

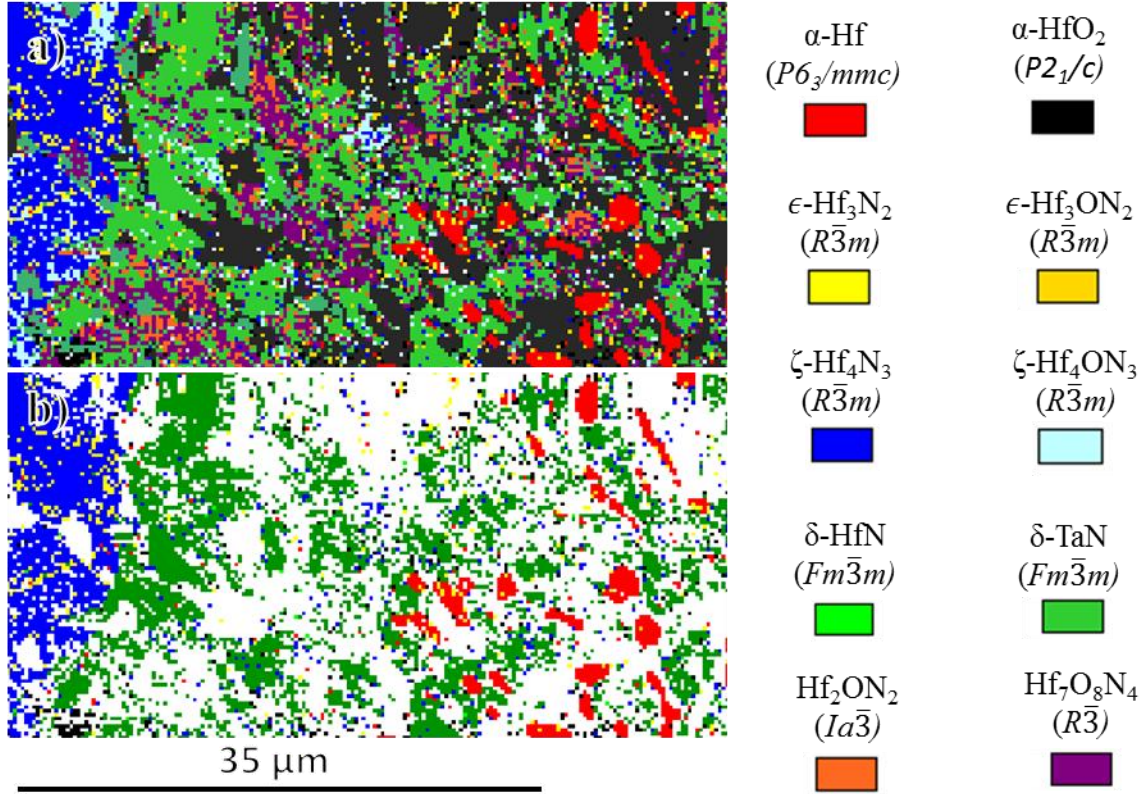


Figure C-9: EBSD of high-temperature flexural tested 80HfN-20TaN at 1650°C. The bulk is on left and scale on right. All phases are shown in (a) including the prior-literature Hf_2ON_2 and $\text{Hf}_7\text{O}_8\text{N}_4$ oxy-nitrides as well as the predicted Hf_3ON_2 and Hf_4ON_3 . Only the nitrides and elemental Hf are shown in (b) for comparison.

Phase	Vol. %
α -Hf	3.8
ϵ - Hf_3N_2	2.0
ζ - Hf_4N_3	8.5
δ -HfN	0.5
β -Ta	3.0
δ -TaN	25.2
α - HfO_2	19.3
$\text{Hf}_7\text{O}_8\text{N}_4$	11.5
Hf_2ON_2	3.7
ϵ - Hf_3ON_2	3.3
ζ - Hf_4ON_3	5.5

Table C-1: EBSD of high-temperature flexural tested 80HfN-20TaN at 1650°C.

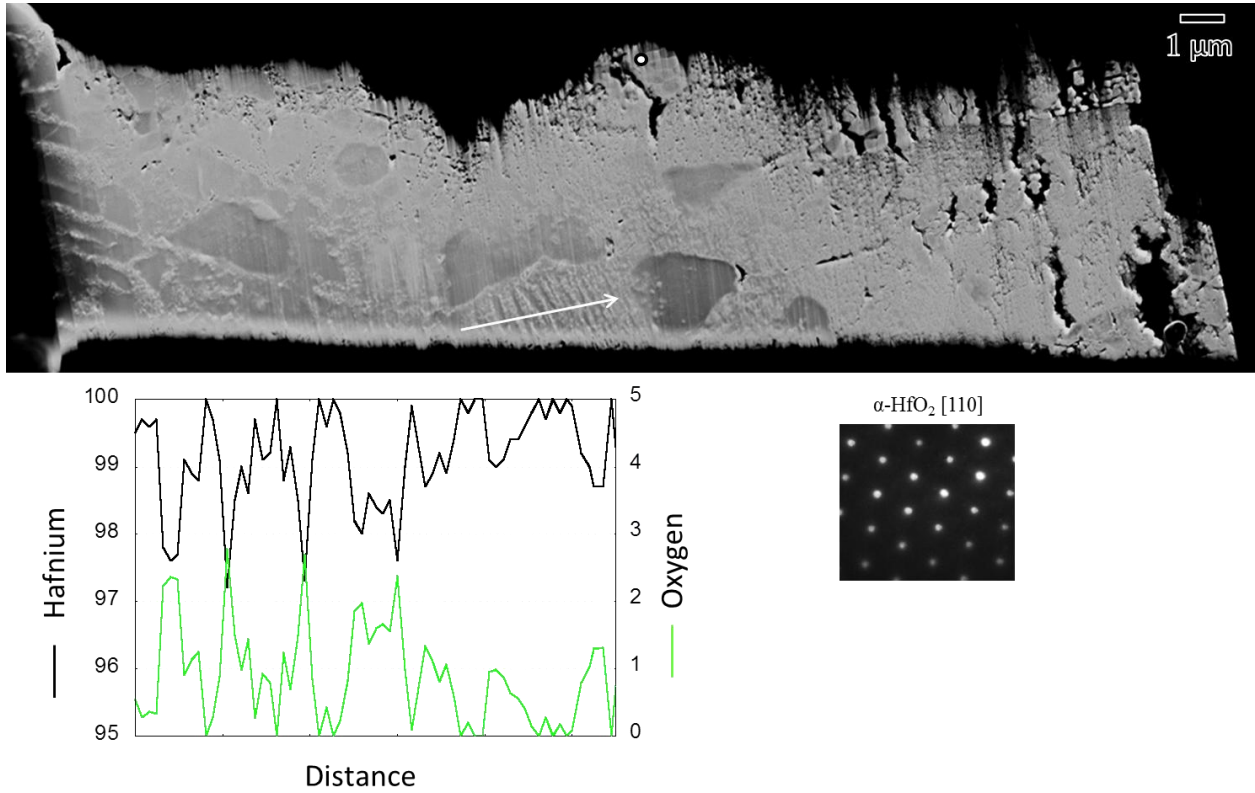


Figure C-10: HAADF STEM image (a) of the 1650°C post-tested specimen with bulk on left and oxide scale on left. The line profile (b) from (a) and the diffraction pattern (c) is the spot found in (a).

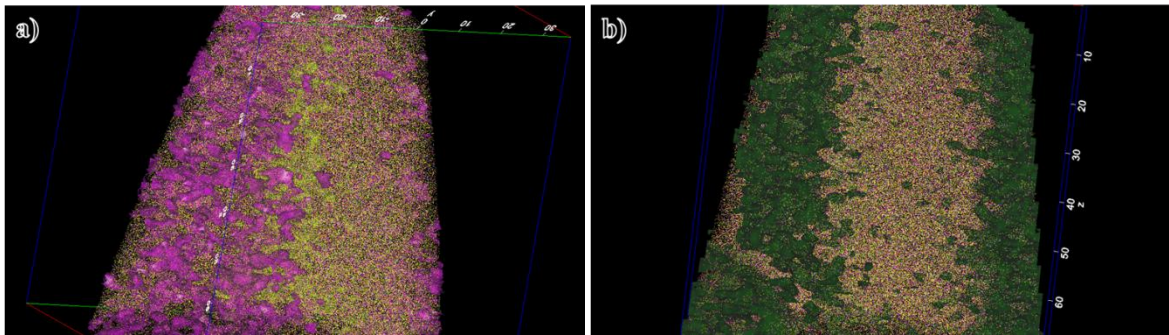


Figure C-11: Atom probe tip (a) from bulk of 1650°C tested nitride and tip (b) near oxide/intermediate interface.

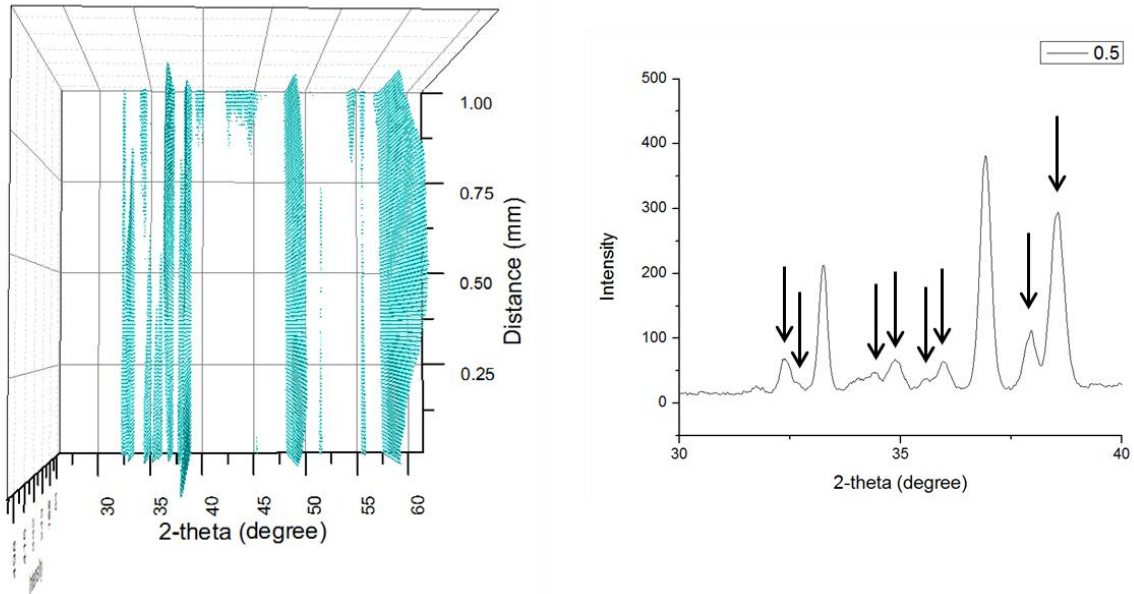


Figure C-12: XRD line scan of 1650°C specimen from bulk (bottom, distance = 0) to oxide scale (distance = 1.00). At distance = 0.5 an example 2D plot shows the peak shifting.

	Measured (Schulz)	0.00 mm	0.5 mm	0.88 mm	1 mm	Prior (McMurdie)
Chemical Formula	Hf					Hf
Crystal System	Hexagonal					Hexagonal
Space Group	<i>P63/mmc</i> (194)					<i>P63/mmc</i> (194)
<i>a</i> (nm)	0.31926	0.31926	0.32004	0.32004	0.32004	0.3196
<i>b</i> (nm)	0.31926	0.31926	0.32004	0.32004	0.32004	0.3196
<i>c</i> (nm)	0.52538	0.50943	0.50791	0.50791	0.50791	0.5058
	Measured (Schulz)	0.00 mm	0.5 mm	0.88 mm	1 mm	Prior (Rudy)
Chemical Formula	HfN _{0.67}					HfN _{0.67}
Crystal System	Rhombohedral					Rhombohedral
Space Group	<i>R-3m</i> (166)					<i>R-3m</i> (166)
<i>a</i> (nm)	0.32179	0.31926	0.32004	0.32004	0.32004	0.3206
<i>b</i> (nm)	0.32179	0.31926	0.32004	0.32004	0.32004	0.3206
<i>c</i> (nm)	2.34306	2.45917	2.29042	2.41220	2.41220	2.326
	Measured Schulz	0.00 mm	0.5 mm	0.88 mm	1 mm	Prior (Rudy)
Chemical Formula	HfN _{0.67}					HfN _{0.67}
Crystal System	Rhombohedral					Rhombohedral
Space Group	<i>R-3m</i> (166)					<i>R-3m</i> (166)
<i>a</i> (nm)	0.00000	0.31926	0.32004	0.32004	0.32004	0.3206
<i>b</i> (nm)	0.00000	0.31926	0.32004	0.32004	0.32004	0.3206
<i>c</i> (nm)	0.00000	2.33065	2.44789	2.67139	2.67139	2.326
	Measured (Schulz)	0.00 mm	0.5 mm	0.88 mm	1 mm	Prior (Rudy)
Chemical Formula	HfN _{0.75}					HfN _{0.75}
Crystal System	Rhombohedral					Rhombohedral
Space Group	<i>R-3m</i> (166)					<i>R-3m</i> (166)
<i>a</i> (nm)	0.32152	0.31926	0.32004	0.32004	0.32004	0.3214
<i>b</i> (nm)	0.32152	0.31926	0.32004	0.32004	0.32004	0.3214
<i>c</i> (nm)	3.10719	3.06983	3.02464	3.03878	3.03878	3.112
	Measured (Schulz)	0.00 mm	0.5 mm	0.88 mm	1 mm	Prior (Rudy)
Chemical Formula	HfN _{0.75}					HfN _{0.75}
Crystal System	Rhombohedral					Rhombohedral
Space Group	<i>R-3m</i> (166)					<i>R-3m</i> (166)
<i>a</i> (nm)	0.32152	0.31926	0.32004	0.32004	0.32004	0.3214
<i>b</i> (nm)	0.32152	0.31926	0.32004	0.32004	0.32004	0.3214
<i>c</i> (nm)	3.10719	3.22919	3.20735	3.20735	3.23601	3.112
	Measured (Schulz)	0.00 mm	0.5 mm	0.88 mm	1 mm	Prior (Fiala)
Chemical Formula	HfN					HfN
Crystal System	Cubic					Cubic
Space Group	<i>Fm-3m</i> (225)					<i>Fm-3m</i> (225)
<i>a</i> (nm)	0.45108	0.44992	0.44992	0.44992	0.44992	0.452
<i>b</i> (nm)	0.45108	0.44992	0.44992	0.44992	0.44992	0.452
<i>c</i> (nm)	0.45108	0.44992	0.44992	0.44992	0.44992	0.452

Table C-2: Lattice parameters based on XRD line scan. Starting at top: (1) Hf, (2) Hf₃N₂ main peak, (3) Hf₃N₂ new split peak, (4) Hf₄N₃ main peak, (5) Hf₄N₃ new split peak, (6) HfN.